Study of intermetallic nanoparticles and MOF-derived nanostructures in electrocatalysis

by

Zhiyuan Qi

A dissertation submitted to the graduate faculty

in partial fulfillment of the requirements for the degree of

DOCTOR OF PHILOSOPHY

Major: Chemistry

Program of Study Committee:
Wenyu Huang, Major Professor
Robbyn K. Anand
Gordon J. Miller
Patricia A. Thiel
Yan Zhao

The student author, whose presentation of the scholarship herein was approved by the program of study committee, is solely responsible for the content of this dissertation. The Graduate College will ensure this dissertation is globally accessible and will not permit alterations after a degree is conferred.

Iowa State University

Ames, Iowa

2018

DEDICATION

The dissertation is dedicated to my family, some of whom did not live to see it published.

TABLE OF CONTENTS

ACKNOWLEDGMENTS

First of all, I would like to sincerely thank my supervisor, Prof. Wenyu Huang for all your encouragement, support, patience during my doctoral studies since 2012. Thank for guiding me in both professional and personal life. I would really appreciate everything I learned from you and in Huang's group, which will definitely be with me through my research career. I would also like to thank my other committee members: Prof. Gordon J. Miller, Prof. Patricia A. Thiel, Prof. Robbyn K. Anand, Prof. Yan Zhao, and Prof. Ning Fang for all your insightful advice and comments during my Ph.D. study.

In addition, I deeply appreciate all the help from past and current Huang group members: Dr. Chaoxian Xiao, Dr. Zhiyong Guo, Dr. Xinle Li, Dr. Raghu V. Maligal-Ganesh, Kyle, Daniel, Yuchen, Jason, Sanaz, Minda, Sangki, Biying, Xuechen, Patrick, Alex, and Ranjai. I am especially thankful to Yuchen for all the beneficial discussions, your great contributions in Chapter 3 and 5 and friendship over the years. Many thanks to Xinle and Raghu for all your kindness and selfless help. I am thankful to our collaborator: Prof. Yue Wu and Zhe for initiating the collaboration and involving me in your excellent research. I also owe my gratitude to my friends acquainted in Ames: Peng, Ping, Jie, Weiwei, Tuo, Tai, Chen, Long, Qiaochu and so on. Thank you all for the great memories.

I would like to thank my family members: especially my parents and parents in law. No words can express my appreciation for all your sacrifice during my Ph.D. study. Thank you so much for your support and love through my life. Finally, my deepest thanks go to my loving and caring wife, Qinyan. You are truly my sunshine and greatest inspiration. Thanks for your support, encouragement, and love over the years.

ABSTRACT

Electrocatalysis plays a critical role in the clean energy conversions nowadays, such as fuel cells and batteries. With the increasing population and energy demands, people are aiming to build a global-scale sustainable energy system in the future, which could convert the abundant N2, O2, water into more useful chemicals and fuels via electrocatalysis and electricity from renewable energies (e.g., wind, solar energy). Therefore, there is an urgent need to design electrocatalysts with higher activity, better stability, and higher selectivity. Two strategies are commonly applied to enhance the activity: 1) increase the number of active sites and 2) increase the intrinsic activity of each active site. By using support and alloying in our research, we could achieve both strategies simultaneously.

In this dissertation, I present several examples of confined intermetallic nanoparticles and MOF-derived nanomaterials for enhanced electrocatalysis. In chapter 2, I synthesized sub-4 nm monodispersed PtZn intermetallic nanoparticles supported on carbon nanotubes with the protection of mesoporous silica shell via high temperature annealing. Both specific activity and mass activity towards methanol oxidation reaction of smaller PtZn nanoparticles are greatly enhanced, revealing that the smaller particles not only increase the number of active sites but also increase the intrinsic activity of each site. Moreover, both DFT calculation and experimental results indicating PtZn systems go through a “non-CO pathway”, due to the stabilization of the *OH species by Zn atoms. Chapter 3 shows a facial synthesis of intermetallic nanoparticles as electrocatalysts via one-pot pyrolysis of ZIF-8 encapsulated metal nanoparticles. ZIF-8 works as both carbon source, zinc precursors, encapsulation shell in the formation of zinc-containing intermetallic nanoparticles supported by nitrogen doped carbon. This method allows the fine tuning of particle size and composition, and more importantly, provides high thermal stabilities up

to 1000 ˚C. In chapter 4, I showed the enhanced hydrogen evolution activity of ordered Pt3Ti intermetallic nanoparticles supported by Ti3C2 Mxene sheet. We further demonstrated the enhanced activity is due to the strong synergistic effect between Pt3Ti and Mxene support. Chapter 5 shows the morphology inherence from hollow ZIFs to hollow carbons with superior activities of oxygen reduction reaction. The designed hollow carbons are not only having better mass transfer but also able to introduce the heteroatoms such as Fe onto the inner wall, which could promote the activity of ORR.

CHAPTER 1. INTRODUCTION

1.1 History of electrochemistry

Isaac Newton once said: "If I have seen further it is by standing on the shoulders of Giants." Without the effort dedicated by generation upon generation of scientists, we would not have the flourishing development of electrochemistry and electrochemical applications nowadays. Much earlier than the discovery and identification of electrons by Sir J.J. Thomson in 1897, the electrochemical phenomena and electrical matters have been explored and understood via detailed experiments. By the mid-18th century, Charles Fran ̧s de Cisternay du Fay discovered the existence of two types of electricity and right after that the law of electrostatic attraction was developed by Charles-Augustin de Coulomb. The birth of electrochemistry is considered as that Luigi Galvani proposed a "Nerveo-electrical substance" in animal tissue, which bridges the electricity and chemical reactions.[1] In 1800, the first electrolysis of water was achieved by William Nicholson and Johann Wilhelm Ritter, and right afterward Johann accomplished the first electroplating.[2] In 1834, Michael Faraday published the laws of electrolysis which provides a tool to control the electrochemical reaction quantitatively.[3] Faraday also made a significant contribution to the terminology in electrochemistry, most of which are still used today. The first fuel cell was produced by William Grove in 1839.[4] In 1888, Walther Hermann Nernst invented the concept of electromotive force (emf) of the voltaic cell and constructed the well-known Nernst equation in 1889.[5-6] Julius Tafel formulated the famous Tafel equation by summarizing tremendous experimental results in 1905, initiating the kinetic study of electrochemical reactions. He is also known for the discovery of Tafel mechanism in hydrogen evolution. Electrochemistry has a rapid growth in the 20th century as well. Butler-Volmer equation well described the heterogeneous kinetics on the electrode. A complete fundamental theory of electrode reactions was

established by Alexander Frumkin to reveal the interfacial structure between electrode and electrolyte, which help the study of electrode kinetics. Paul Delahay systematically clarified various electrochemical measurement methods. In the last two decades, electrochemistry has moved a considerable step further in mechanism and kinetic study when coupled with *in-situ* characterization methods, such as FTIR spectroscopy and mass spectroscopy.

1.2 Electrochemical techniques

Electrochemical reactions involve multiple steps on the electrode-electrolyte interface including adsorption/desorption, mass transfer and charge transfer.[7] Similar to heterogeneous catalytic reactions, the rate of electrochemical reactions could be altered by temperature, pressure, mass transfer, surface structure and composition of catalysts. Meanwhile, electrochemical reactions have their advantages, one of which is the precise control of the applied activation energy. By simply alternating the applied potential between the electrode-electrolyte interface, the corresponding reaction rate and mechanism can be controlled.[8] For most electrochemical reactions, the change of 1 V in potential leads to a dramatic increase in reaction speed of 10^{10} magnitude, which cannot be achieved by general chemical reactions. Besides the applied potential, the reaction rate is also determined by the interfacial structure (i.e., double layer capacitor) between electrolyte and electrode. Therefore, it is critical to carefully characterize the surface structures and study the electrochemical behaviors of different catalysts using advanced techniques. Before discussing the structure and electrochemical properties of those electrocatalysts I studied in my Ph.D. research, I will first summarize the common electrochemical techniques used in studying electrocatalysis. These techniques include linear sweep voltammetry, cyclic voltammetry, rotating disk electrode, rotating ring-disk electrode, electrochemical impedance spectroscopy.

Linear sweep voltammetry Potential (*E*) plays a significant role in controlling the reaction rate, whose change can be followed by recording the electric current (*i*) v.s. time (*t*) in electrochemistry. However, analyzing thousands of current-time (*i*-*t*) curves recorded at a series of different potentials is laborious. It is also difficult to recognize reactants depleting and new species forming (i.e., to observe current peaks) from *i*-*t* curves. In fact, the three-dimensional *i*-*t*-*E* realm could be easily obtained in one single experiment by sweeping the potential with a constant scan rate ν while recording the *i*-*E* curve. Since the typical potential ramp is varied linearly within time, this experiment is thus mostly referred as liner sweep voltammetry (LSV). A customary LSV plot records current as a function of potential, which is equivalent to recording current versus time when scan rate is known.[8] A peaked current-potential curve will be observed when an electrochemical reaction is occurring in an unstirred solution. For example, if the starting potential of LSV is more positive than the $E^{0'}$ of a reduction, only non-faradaic current is recorded, which is more like a background. As the negatively sweeping potential is close to the formal potential $E^{0'}$, the cathodic current starts to be observed and the total current will increase. The reaction will speed up with sweeping to the more negative potential because the increased consumption rate of reactant result in an increase in the flux (and also current) to the electrode surface. The current reaches to a maximum value when the surface concentration of reactant drops close to zero, leading to the highest mass transfer rate. Then the current will decrease due to the depleting effect, and thus a current peak is obtained. LSV is widely applied in rotating disk electrode (RDE) experiment to study the reaction mechanism and kinetic, which will be discussed together with RDE later.

Cyclic voltammetry In the above example, when the surface concentration of the reactant is zero and the current starts to drop due to the depleting, there are a large number of products

around the electrode surface which are oxidizable. If we reverse the potential scan directly after this point, the oxidation will become more favored as the potential moves positively. As a result, an anodic current peak with a similar shape will be observed. The experiment with a cyclic potential sweep is named as cyclic voltammetry (CV), which is a powerful reversal technique to initiate the electrochemical study of new systems and complicated reactions. Useful information could be obtained from the equations listed below. [8]

Peak current: $i_p = (2.65 \times 10^5) n^{\frac{3}{2}} A D^{\frac{1}{2}} C^* \nu^{\frac{1}{2}}$,

where n is the number of transferred electrons, A is the surface area of electrode, D is the diffusion coefficient, $C^*$is the bulk concentration and ν is the scan rate of the potential. Therefore, n could be derived by plotting i_p versus $\nu^{\frac{1}{2}}$ when D and C^* are known.

Peak potential: $E_p = E_{1/2} - 1.109 \frac{RT}{nF} = E_{1/2} - 28.5/n$

Half-peak potential: $E_{p/2} = E_{1/2} + 1.09 \frac{RT}{nF} = E_{1/2} + \frac{28.0}{n}$

Nernstian wave follows $\left|E_p - E_{p/2}\right| = 2.20 \frac{RT}{nF} = 56.5/n$

The above three equations (2-4) reflect that $E_{1/2}$ (potential at $i_p/2$) is located in between E_p and $E_{p/2}$, and they are all independent from the scan rate. The last equation is also very useful to determine whether a given reaction is Nernstian or not. The detailed application of CV will be discussed for each electrochemical reaction.

Rotating Disk Electrode Rotating disk electrode (RDE) is a convective system used to measure the steady-state polarization curves at different rotating rates.[8] A typical RDE consists of a disk electrode (e.g., glassy carbon or noble metal) imbedded in an insulating (e.g., PTFE) rod. The exact alignment of the disk and insulating mantle is critical to avoid the turbulence at high

rotating rates. Besides, a good seal between the electrode and the insulator is vital to prevent the leakage of the electrolyte that will etch the inner metal pieces. The rotating electrode is immersed in the electrolyte, typically functioning as a working electrode, while the other end is fixed to a motor by a shaft. The electrical connection is achieved by two metal brush contacts on the side of the shaft. During the electrochemical measurement (e.g., linear sweep voltammetry), the electrode rotates at a targeted angular velocity ω, which drags the electrolyte flow up towards the electrode and flinging the solution away from the electrode center via centrifugal force. Unlike the unstirred measurements (e.g., CV) where the steady-state current is mostly limited by the diffusion of redox species to the electrode surface, the steady current of RDE system is dependent on the electrolyte flow rate. The rate of electrolyte flow is controlled by the electrode's rotating speed, which has been rigorously modeled.[8] Therefore, RDE is widely used to investigate the electrochemical reaction kinetics and mechanisms.[9]

The mass transfer of charged species in a fluid is governed by Nernst-Planck Equation:[8]

$$\boldsymbol{J_j} = -D_j \boldsymbol{\nabla} C_j - \frac{z_j F}{RT} D_j C_j \boldsymbol{\nabla} \phi + C_j \boldsymbol{\upsilon}$$

where $\boldsymbol{J_j}$ is the flux of species *j*, $D_j$is the diffusion coefficient, $\boldsymbol{\nabla} C_j$ is the concentration gradient, z_j and C_j are the charge and concetraion of species *j*, $\boldsymbol{\upsilon}$ is the solution velocity.

The first term on the right side ($-D_j \boldsymbol{\nabla} C_j$**)** represents the contribution of diffusion to the total mass transfer, and the second term ($-\frac{z_j F}{RT} D_j C_j \boldsymbol{\nabla} \phi$) and the last term ($C_j \boldsymbol{\upsilon}$) represents the contribution of migration and convection respectively. In most of the studied systems containing excess supporting electrolytes, the influence of migration become negligible. We thus could obtain a general convective-diffusion equation in the rectilinear coordinates (x, y, z) as below, while assuming $\boldsymbol{D_j}$ is not a function of x, y, and z.

$$\frac{\partial \boldsymbol{C}_{\mathrm{j}}}{\partial t} = -\boldsymbol{\nabla} \boldsymbol{J}_{\mathbf{j}} = D_{\mathrm{j}} \boldsymbol{\nabla}^{\mathbf{2}} C_{\mathrm{j}} - \boldsymbol{v} \boldsymbol{\nabla} C_{\mathrm{j}}$$

Therefore, the concentration profiles can be solved by determining the concentration gradient $C_{\mathrm{j}}\ (x, y, z)$ at the electrode surface and the volecity profile $\boldsymbol{v}\ (x, y, z)$. After von Karman and Cochran successfully determined the velocity profile by solving the hydrodynamic equations, it is feasible to solve the convective-diffusion equation with appropriate boundary conditions. For the limiting current region, we have:

1) C_O(y=0)=0, where C_O is the concetration of oxidized species, y is the distance perpendicular to the electrode;
2) $\lim_{\mathrm{y}\to\infty} C_O = C_O^*$, where C_O^* is the bulk concentration of oxidized species.[8]

We thus could determine the mass-transfer limiting current $i_{l,c}$ by *Levich Equation*:

$$i_{l,c} = 0.620\, n\, F\, A\, D^{\frac{2}{3}} \omega^{\frac{1}{2}} v^{-\frac{1}{6}} C_O^*$$

where n is the number of moles of electron transferred (unitless), F is the Faraday constant (C/mol), A is the geometric electrode surface area (cm^2), D is the diffusion coefficient of species O (cm^2/s), ω is the angular rotation rate (rad/s), v is the kinematic viscosity (cm^2/s), C_O^* is the bulk concentration of species O ($mole/cm^3$). A real example to investigate reaction kinetics of oxygen reduction reaction (ORR) will be given in the Section 1.3.

Rotating Ring-Disk Electrode A rotating ring-disk electrode (RRDE) is very similar to RDE, except the addition of the second working electrode (e.g., Pt metal) with a ring shape around the center disk electrode. The two electrodes are separated by insulators and connected to potentiostat by different metal brushes. The measurement on the disk electrode will not be affected by the presence of ring electrode. The ring electrode is used to collect the intermediates produced on the disk electrode, which facilitates the understanding of reaction mechanism. RRDE involves

more parameters compared to a single electrode: the potential of disk and ring electrodes, the current of disk and ring electrodes (E_D, E_R, I_D, and I_R respectively). In order to separately adjust on E_D and E_R, a bipotentiostat is needed to carry out RRDE measurements.[8]

A plot of I_D and I_R as a function of E_D (E_R is usually kept as a constant) could be obtained via a RRDE collection experiment.[8] For a one-electron transferred reaction $O + e^- \rightarrow R$ measured by RRDE, species O is first reduced to R on disk electrode and a portion of R will get oxidized on ring electrode via collection experiments (E_R is set to have strong oxidizing power). The ring current is related to disk current by collection efficiency N:

$$N = -\frac{I_R}{I_D}$$

where N is only determined by the morphology of two electrodes (i.e., two diameters and the gap distance between the two electrodes). The application of RRDE will also be discussed with ORR in Section 1.3.

Electrochemical Impedance Spectroscopy The techniques discussed previously always involve potential steps and sweeps, which drive the reaction far from the equilibrium condition. Generally, an electrochemical cell or electrode can be simplified as the impedance to a small sinusoidal excitation. Electrochemical impedance spectroscopy (EIS) is a technique that studies the system response to the applied perturbation (i.e., an alternating signal: potential or current) at steady state. The biggest advantage of EIS is its great simplification in studying kinetic and diffusion. In EIS, the information could be obtained close to equilibrium, which leaves out detailed studying the transient response of *i*-*E* curves over a large range of overpotentials.[8]

An alternating signal, e.g., an alternating current, can be expressed as

$$i(t) = I\sin(\omega t + \phi)$$

where I is the magnitude of current, $\omega = 2\pi f$ is the angular frequency, ϕ is the phase angle which is usually measured with respet to the other reference signal. We can use rotating vectors (or phasors) to represent the relationship between two alternating signals in the phasor diagram. Particularly, impedance is the ratio of a sinusoidal voltage to the corresponding current flow, and could be formulated as:

$$\boldsymbol{Z} = \frac{\dot{E}}{\dot{I}}$$

where $\dot{E}$ and $\dot{I}$ are both in phasor notation.

It is also convenient to use complex notation to denote phasors by defining components along the abscissa in phasor diagram as "real" and those along ordinate as "imaginary". Impedance is thus generally represented as:

$$\boldsymbol{Z}(\boldsymbol{\omega}) = Z_{Re} - jZ_{Im}$$

where Z_{Re} and Z_{Im} are the real and imaginary part of impedance and $j = \sqrt{-1}$.

Mathematically, we could solve the impedance of simple electrical elements, such as resistors ($\boldsymbol{Z_R}$), capacitors ($\boldsymbol{Z_C}$), and inductors($\boldsymbol{Z_I}$).

$$\boldsymbol{Z_R} = R$$

$$\boldsymbol{Z_C} = \frac{1}{j\,C\omega}$$

$$\boldsymbol{Z_I} = j\,L\,\omega$$

where R, C, and L are resistance, capacitance and inductance respectively.

A Nyquist plot is commonly obtained by plotting Z_{Im} vs. Z_{Re} with the varying frequencies, where we could further discover the equivalent circuit consisting of resistors and capacitors. The equivalent circuit could help us understand surface structures, reaction mechanisms (mass transfer limited or charge transfer limited) and kinetics; determine diffusion coefficient D, exchange

current i_0, and number of electron transferred n, by solving the solution resistance R_Ω, double layer capacitance R_{dl}, charge transfer resistance R_{ct}, and Warburg impedance Z_w.[8]

Besides the above-mentioned classic electrochemical techniques, the characterization of electrode surface and the study of electrochemical reactions could be further explored and confirmed via other techniques: *in situ* FTIR or Raman spectroscopy to analyze the sorption and binding strength of involved reaction species on/around electrode surface and reveal the reaction mechanisms;[10] differential electrochemical mass spectroscopy (DEMS) to monitor the chemical concentration changes[11-12] and study chemical conversion by isotope labeling,[13] density functional theory (DFT) in calculating sorption energy, activation energy, and the possible reaction pathways.[14-15] When combined these different methods in the electrochemistry study, electrochemists are able to gain a comprehensive understanding of the reaction at the atomic and molecular level, ultimately to design superior catalytic systems for the chemical and energy conversions.

1.3 Featured electrochemical reactions

Electrocatalysis plays an essential role in clean energy and conversion such as fuel cells, rechargeable batteries. In this chapter, I will mainly discuss the mechanism and typical research methodologies of three representative electrochemical reactions, which are oxygen reduction reaction, hydrogen evolution reaction, and methanol oxidation reaction. Very recently, electrochemical reduction of CO_2 and N_2 has gained an increasing amount of research interests, and I hope to continue my research on those topics at my next stop.

Oxygen reduction reaction (ORR) is the cathodic reaction in proton exchange membrane (PEM) fuel cells. The sluggish reaction mechanism of ORR hinders the practical application of

fuel cell, and thus an ORR catalyst is required to speed up the reaction.[16] Pt catalyst is generally accepted as the most practical catalyst and has already been used in the commercial fuel cell vehicle. However, it's not generally affordable due to the high cost. Tremendous research efforts have been made to design cheap ORR catalysts to replace the expensive Pt, including noble metal alloys and interemtallics[17], carbon materials,[18] and transition metal carbides.[19]

In aqueous solution, ORR mainly occurs in two different pathways: (1) reduce O_2 to hydrogen peroxide (H_2O_2) via a 2-electron pathway; and (2) reduce O_2 to H_2O via a 4-electron pathway.[20] A 1-electron pathway from O_2 to superoxide (O_2^-) is also possible in a non-aqueous solution.[21] For fuel cell application, a 4-electron pathway is greatly preferred to achieve higher current in the same period of reaction time. The 2-electron pathway could also be used to produce H_2O_2 in industry.[17] Based on the different electrolyte media, ORR reaction could be written as below:

Acidic solution		**Basic solution**	
$O_2 + 4e^- + 4H^+ \rightarrow 2H_2O$	E = 1.23 V	$O_2 + 4e^- + 2H_2O \rightarrow 4OH^-$	E= 0.40 V
$O_2 + 2e^- + 2H^+ \rightarrow H_2O_2$	E = 0.70 V	$O_2 + 2e^- + H_2O \rightarrow H^- + OH^-$	E =-0.065 V
$H_2O_2 + 2e^- + 2H^+ \rightarrow 2H_2$	E = 1.76 V	$H_2O_2 + 2e^- + 2H^+ \rightarrow 2H_2O$	E = 1.76 V

Similar to most of the electrochemical reactions, ORR involves multiple elementary reactions, including electron transfer steps and chemical steps. Since it is very complicated to determine the rate of the whole reaction, the rate-determining step (RDS) is considered as a pseudo-elementary step and used to evaluate the reaction rate. RDS of ORR could be a chemical step or electron transfer step, depending on the applied catalyst and potential.[16-17,22] When the solution is well stirred, and/or current is kept low so that the surface concentration and bulk

concentration of oxygen are close, the reaction rate of an electron transfer step can be formulated by Butler-Volmer equation[8]:

$$j = j_0 \left(e^{-\frac{\alpha F\eta}{RT}} - e^{\frac{(1-\alpha)nF\eta}{RT}}\right)$$

where j is the ORR current density, j_0 is the exchange current density, n is the number of electrons transferred in RDS, α is the transfer coefficient representing the fraction of cathodic reaction, $\eta = E - E_{eq}$ is the overpotential, F is the Faraday constant, R is the ideal gas constant, and T is the temperature in Kelvin. (Note that positive current is used to represent cathodic current and negative current for anodic current in this equation.)

A large j_0 and/or small η is perferred to obtain the high current density at low overpotential. At larger η, $e^{-\frac{\alpha nF\eta}{RT}} \gg e^{\frac{(1-\alpha)nF\eta}{RT}}$, the Butler-Volmer equation can be simplified to:

$$j = j_0 \left(e^{\frac{-\alpha nF\eta}{RT}}\right)$$

$$\text{or} \qquad \eta = \frac{RT}{\alpha nF}\ln j_0 - \frac{RT}{\alpha nF}\ln j$$

The bottom equation has a similar format to the empirical Tafel equation $\eta = a \pm b\log j$, (+b for anodic reaction and – b for cathodic reaction) and we thus have:

$$b = -\frac{2.303RT}{\alpha nF}, \; a = \frac{2.303RT}{\alpha nF}\log j_0$$

Herein, the b value is the Tafel slope, which could be derived from the plot of η vs. $\log j$, namely Tafel plot. Besides Tafel slope , exchange current density j_0 is the other key parameter we could derive from Tafel plot. They both are widely used to evaluate the catalyst performances, investigate the reaction kinetics, and understand the reaction mechanisms.

When an electrochemical reaction is at equilibrium, anodic reaction and cathodic reaction have the same reaction rate, leading to the net current density as zero. The absolute value of the current density of forward and backward reaction is called exchange current density j_0, which

reflects the reaction rate at equilibrium.[8] The exchange current is related to the standard rate constant k_0 via the equation

$$j_0 = F\, k_0\, C_O^{*(1-\alpha)} C_R^{*\alpha}$$

or $$j_0 = F\, k_0\, C, \quad \text{where } C_R^* = C_O^* = C$$

Since oxygen is always saturated in solution for ORR measurement, the ORR exchange current density can be directly used to compare the reaction rate, which is greatly influenced by the electrode surface and catalyst type, and can vary from 10^{-5} to 10^{-10} A/cm^2.

The Tafel slope was solely dependent on the number of transferred electron and the transfer coefficient at given temperature. A small Tafel slope is highly desired as the overpotential increases slowly with the current density. 60 mV/dec and 120 mV/dec are the two typical Tafel slope for ORR, observed in different catalyst surface and potential range.[23] For example, 60 mV/dec was observed at high potential range (larger than 0.8 V) on Pt electrode when the actual surface is a mixture of PtO and Pt. However, a slope of 120 mV/dec was observed at the low potential range where the electrode is purely Pt.[24] We thus could conclude the ORR mechanism are different on Pt surface and Pt/PtO surface.

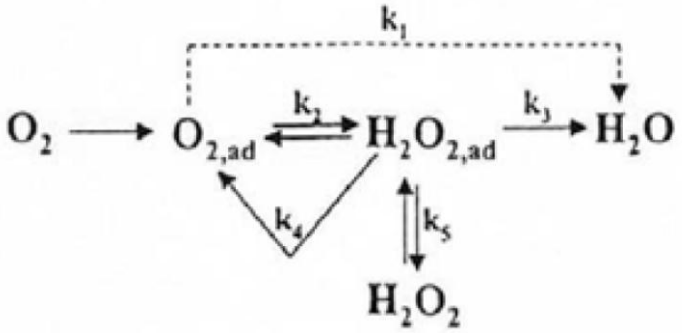

Figure 1.1 Scheme of simplified ORR reaction pathways. Reprint with permission from *J. Phys. Chem. B*, **2004**, 108 (46), 17886-17892. Copyright © 2004 American Chemical Society.

Besides experimental observations, the ORR mechanism on Pt has also been well investigated by density functional theory (DFT) calculations.[25] The dissociative mechanism and associative mechanism have been proposed for low j_0 and high j_0 range respectively.[26]

Dissociative Mechanism	**Associative Mechanism**
$\frac{1}{2}O_2 + * \rightarrow O^*$	$O_2 + * \rightarrow O_2^*$
$O^* + e^- + H^+ \rightarrow OH^*$	$O_2^* + e^- + H^+ \rightarrow HO_2^*$
$OH^* + e^- + H^+ \rightarrow H_2O + *$	$HO_2^* + e^- + H^+ \rightarrow H_2O + O^*$
	$O^* + e^- + H^+ \rightarrow OH^*$
	$OH^* + e^- + H^+ \rightarrow H_2O + *$

Here, * represents the active site on Pt surface. The dissociative mechanism involves the breaking of O-O bond. The adsorbed O atom is further reduced to water by two consecutive reduction steps. No H_2O_2 is formed by this mechanism. In the associative mechanism, the adsorbed O_2 and HO_2^* could also form H_2O_2 without further breaking the O-O bond.[27] The simplified ORR reaction pathway on Pt is summarized in Figure 1.1, while the full mechanism is still not fully understood.

Additionally, ORR can also be catalyzed by carbon materials in alkaline solution. The corresponding mechanisms are summarized below.[28-29] For the left mechanism, the RDS is $[O_{2(ads)}]^- \rightarrow O_{2(\text{ads})}^-$ when pH is larger than 10. The reactant $[O_{2(ads)}]^-$ that is relatively inert migrates to the active sites to form $O_{2(\text{ads})}^-$.

On Glass Carbon Electrode	On Graphite Electrode
$O_2 \rightarrow O_{2(ads)}$	$O_2 \rightarrow O_{2(ads)}$
$O_{2(ads)} + e^- \rightarrow [O_{2(ads)}]^-$ (RDS when pH <10)	$O_{2(ads)} + e^- \rightarrow O^-_{2(ads)}$ RDS
$[O_{2(ads)}]^- \rightarrow O^-_{2(ads)}$ (*RDS when pH >10*)	$2O^-_{2(ads)} + H_2O \rightarrow O_2 + HO_2^- + OH^-$
$O^-_{2(ads)} + H_2O \rightarrow HO_{2(ads)} + OH^-$	
$HO_{2(ads)} + e^- \rightarrow HO^-_{2(ads)}$	
$HO^-_{2(ads)} \rightarrow HO_2^-$	

where (ads) represents the certain species are adsorbed on the electrode surface.

CV, LSV, RDE, RRDE are the four techniques commonly used in the ORR studies. For noble-metal catalysts, CV is used to determine the electrochemical surface area (ECSA) via either H_2 sorption or CO stripping peaks.[30] With ECSA that reflects the number of active sites, catalyst ORR activities at different overpotential can be fairly compared to specific activity (ECSA-normalized current).[17] However, the method cannot be applied to carbon materials as they barely adsorb H_2 or CO molecules. The surface area of carbon can still be estimated by the double layer capacitance. A series of CV with the same potential window but different scan rates should be measured, and a plot of *i* vs. scan rate could be obtained at a fixed potential where the current is only related to the charging/discharging of the electric double layer, and the Faradic current is negligible.[31] With a linear relationship between the resultant current and the scan rates, we could obtain the double layer capacitance of the carbon materials from the slope. The surface area could be calculated as the ratio between the measured capacitance and the literature value of the specific

capacitance of the specific materials. Besides the surface area, CV could also evaluate the ORR activity via the onset potential and the current density of oxygen reduction peak.

RDE is extensively used in studying ORR activities and mechanisms.[16] In a RDE application, LSV is applied to sweep the potential away from the equilibrium potential to the more negative values and to record the corresponding current response. The current follows the Kouteckýy-Levich equation:

$$\frac{1}{i_m} = \frac{1}{i_k} + \frac{1}{i_{Lev}}$$

where i_m is the measured current, i_k is the kinetcic current of ORR , and i_{Lev} is the mass transport current following Levich equation. Both i_k and i_{Lev} are well formulated:

$$i_k = n\ F\ A\ k\ C_{O_2}(y = 0),$$

$$i_{lev} = 0.620\ n\ F\ A\ D^{\frac{2}{3}}\omega^{\frac{1}{2}}v^{-\frac{1}{6}}C_O^*$$

Kouteckýy-Levich plot is obtained by plotting ${i_m}^{-1}$ vs. $\omega^{-\frac{1}{2}}$, and the number of transferred electron involving in ORR could be derived from the slope as diffusion coefficient, kinetic viscosity, surface concentration have all been measured in different electrolytes at certain temperatures. The kinetic current at different potential could also be obtained from the intercept.

RRDE is also used to investigate ORR reaction mechanisms, especially powerful in monitoring the possible intermediate and determining the overall number of electron transferred. The initial ORR occurs on the glassy carbon disk electrode and possible intermediates H_2O_2 will be detected by the Pt ring electrode through an oxidation reaction back to O_2. The number of overall electron transfer is calculated by

$$n_e = \frac{4I_D}{I_D + \frac{I_R}{N}}$$

where I_D is the disk current, I_R is the ring current and N is the collection coefficient which could be determined for each electrode.

Hydrogen evolution reaction (HER) is the cathodic reaction of water splitting reaction.[32] The formed hydrogen gas could be stored for H_2 fuel cell application. Depending on the different electrolytes, this reaction could be expressed by

$2\,H^+ + 2e^- \rightarrow H_2$ in acidic media, and

$2H_2O + 2e^- \rightarrow H_2 + \ 2OH^-$ in basic or neural media.[23]

Although the HER mechanism remains ambiguous in a basic solution, it is widely accepted that HER in an acidic solution typically involves three steps:[33]

Volmer reaction: primary discharge step

$$H_3O^+ + e^- \rightarrow H_{ads} + H_2O$$

$$b = \frac{2.3\,RT}{\alpha F} \approx 120\,mV$$

Heyrovsky reaction: electrochemical desorption step

$$H_{ads} + H_3O^+ + e^- \rightarrow H_2 + H_2O$$

$$b = \frac{2.3\,RT}{(1+\alpha)F} \approx 40\,mV$$

Tafel reaction: recombination step

$$H_{ads} + H_{ads} \rightarrow H_2$$

$$b = \frac{2.3\,RT}{2F} \approx 30\,mV$$

In the first step, proton was reduced to form the adsorbed hydrogen atom (H_{ads}) on the surface. Based on the amount of H_{ads}, HER can proceed by either Heyrovsky reaction or Tafel

reaction or both. [23]The activity of HER is usually compared by 1) onset overpotential (η_{onset}) at the current density varying from 0.5 -2.0 mA cm^{-2} and 2) the overpotential (η) required to yiled 10 mA cm^{-2}.[34] Besides these two overpotentials measured from LSV, we could also derive Tafel slope (b) and exchange current (j_0) via Tafel equation $\eta = a + b\,logj$ to evaluate the reaction meacchanism and intrinsic activity respectively. In some reports, Turnover frequency (TOF) and Faradic efficiency will be measured and compared as well.[35]

Different from experimental measurement, the free energy of hydrogen atom adsorption (ΔG_{H}) is widely used as a descriptor in computational work to evaluate the HER activity, as H_{ads} is invovled in all three reactions as an intermediate.[36-40] A (ΔG_{H}) value close to zero is preferred in principle, which indicates the optimal H_2 binding strength for HER. The binding of H_2 becomes too strong when ΔG_{H} is large and positive, which favors the initial Volmer reaction but makes the sequent Heyrovsky and Tafel reaction hard to occur. In the contrast, the Volmer reaction becomes very slow within a large and negative ΔG_{H}, which limits the activity of the overall reaction.[41]

Methanol oxidation reaction (MOR) is the anodic reaction in direct methanol fuel cells (DMFCs). Compared to hydrogen fuel, methanol is an ideal candidate due to its high theoretical energy density and the ease of storage and transportation. A complete MOR involves 6-electron transferred and multiple steps of sorption to form CO_2 and H_2O, which are more complicated than HER and ORR. Platinum shows the highest activity among the pure metals for MOR, but its surfaces are usually poisoned by the intermediate carbon monoxide.[42] After methanol was adsorbed onto the Pt surface, the C-H activation was achieved by 4 steps, one electron transferred and one proton generated in each step (Figure 1.2).[43] The adsorbed CO was then further oxidized to CO_2, with the assistance of OH species on the adjacent site.[44] Consider that Pt requires a large

potential to form the required OH species, researchers have coupled Pt with other metals such as Pb, Ir, Ru, Fe, Sn via alloying to facilitate the generation of OH species at relatively low potentials.[44-45]

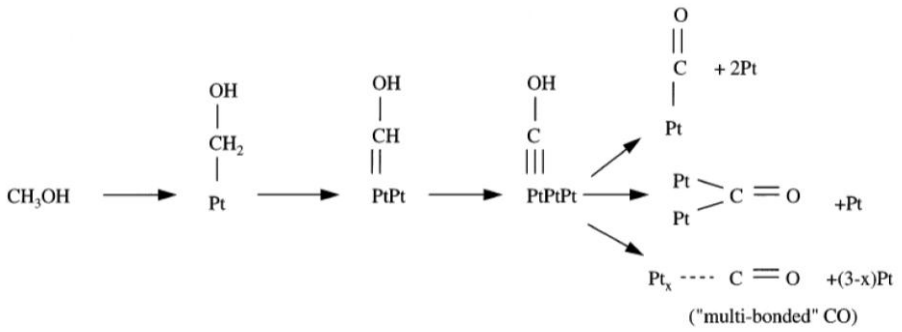

Figure 1.2 Scheme of the consecutive dissociative electroporation of methanol at a Pt electrode.[43] Reprint with permission from *Journal of Electroanalytical Chemistry* **1999,** *461* (1), 14-31. Copyright © 1999 Elsevier B.V.

In a typical CV curve of MOR, two oxidation peaks will be observed, one in the forward scan (sweep positively) and the other in the backward scan (sweep negatively). It is widely accepted that the first oxidation peak in forward scan is due to the oxidation of methanol to CO_2, CO, and other carbonaceous spices. In the backward scan, the oxidation peak was attributed to the further oxidation of adsorbed CO and carbonaceous spices adsorbed to CO_2.[46] Therefore, the peak current density ratio of forward peak and backward peak J_f/J_b is used to evaluate the tolerance towards intermediate poisoning of the catalyst surface.[47]

1.4 Electronic and structural effect of electrocatalysts surface

In chapter 1.3, featured electrochemical reactions and their possible mechanisms are discussed, some of which already involves the presence of active sites from catalysts. We've also shown that distinct reaction mechanism and reaction rate of ORR were observed on different

material surfaces. Therefore, electrocatalysts with high performance are highly desired to control the electrochemical reaction better.

Similar to other catalytic reactions, electrocatalysts are used to lower the reaction activation energy and to increase the electrochemical reaction rate and conversion efficiency.[48-50] In the real electrocatalytic system, electrocatalysts are either directly used as working electrode or deposited onto the surface of the working electrode to test the catalytic performance, in terms of activity, selectivity and stability.[47] The activity of the electrochemical reaction can be evaluated by the faradic current density, overpotential, Tafel slope, exchange current.[32] However, the overall performance could also be influenced by other non-electrochemical steps whose contribution sometimes even dominated over electrocatalytic steps. Therefore, it is widely accepted that the performance of catalysts can be directly compared by the overpotential at a given current density (e.g., DOE target for ORR is to achieve 0.44 A/mg Pt at 0.9 V). [51]

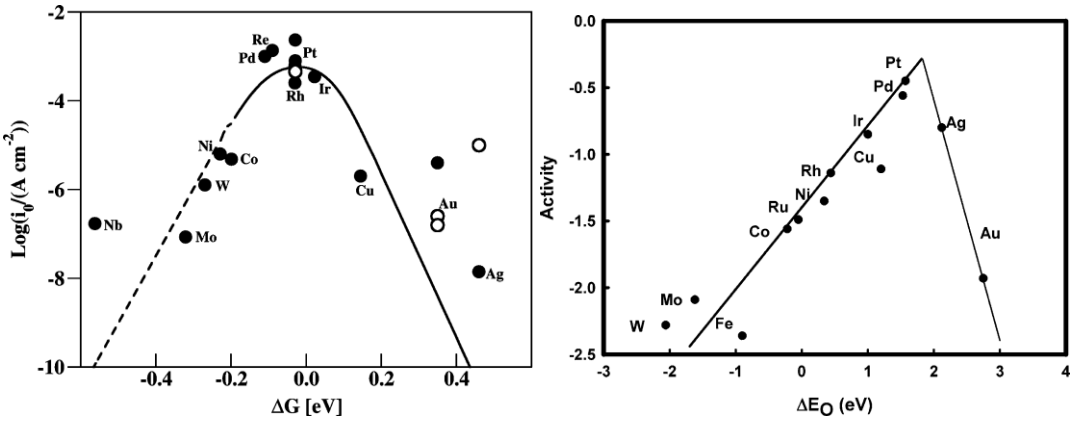

Figure 1.3 HER and ORR volcano plots of metals. The left image is reprinted with permission from *The Journal of Physical Chemistry B* **2004,** *108* (46), 17886-17892. Copyright © 2004 American Chemical Society. The right image is reprinted with permission from *The Journal of Physical Chemistry C* **2010,** *114* (42), 18182-18197. Copyright © 2010 American Chemical Society.

This chapter will mainly discuss the influence of catalyst surface to the overall performance, specifically the electronic and structural effects. Although the two effects cannot be completely distinguished, the electronic effect should be the first principles of designing the catalysts due to its great contribution to enhancing reaction rate via lowering the activation energy[52-54]. As shown in Figure 1.3, there is a volcano-shape relationship between different metal surfaces and their actives toward either ORR or HER.[26,55] It is clearly shown that the electronic structures of different metals strongly influence the sorption of reactants, intermediates, and products, which could further determine the reaction pathway, reaction rate, and activity. In HER and ORR reaction, a moderate ΔG_{H} and O binding energy ΔE_{O} are required to achieve the best activity.

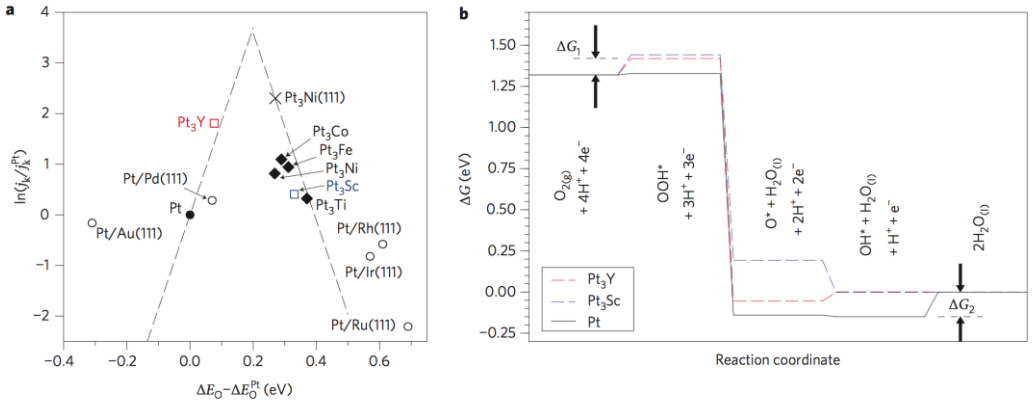

Figure 1.4 Volcano plot of various Pt-based intermetallics and metal overlayers. Reprinted with permission from *Nature Chemistry* **2009,** *1*, 552. Copyright © 2009 Springer Nature.

The electronic structure of noble metal catalysts could be tuned by alloying the second or third metals, which usually lower the d-band center of noble metal and weakened the binding of adsorbate. For examples, O binds strongly with Pt surface, but the oxygen binding was weakened in Pt_3Ni alloy which has been proved the best ORR catalyst so far (Figure 4).[15] By applying the same strategy, Pt and Pd based alloys and intermetallics have been synthesized and shown superior

activities, higher tolerance towards CO poisoning, and better stability in methanol oxidation, ethanol oxidation, formic acid oxidation, oxygen reduction reactions.[46-47,49,51,56-60]

The structural effect usually refers to the surface composition, surface structure, and morphology of the catalyst. As most of the electrochemical reactions are extremely sensitive to the catalyst surface structure, it is very important to investigate the surface atomic arrangement, oxidation states of active sites, and the interaction of the molecule with different surfaces. The pioneering work was carried out on metal single crystal electrodes with defined crystal facets which are ideal catalyst platforms to investigate the reaction mechanism. For example, it has been shown that the activity of electrooxidation of formic acid follows: Pt(110) > Pt(111)> Pt(100) where Pt(110) has the lowest apparent activation energy. The shape-controlled nanoparticle is another ideal platform for electrocatalytic study due to their high surface area to volume ratio and well-defined surface structures. Methods to synthesize shape-controlled nanoparticles are well established and their electrocatalytic activities were investigated in the past decades, including perfect cubic with {100} facets, perfect octahedron with {111} facets, perfect tetrahedron with {111} facets, truncated octahedron with both {111} and {100}, decahedron and icosahedron with {111} facets, hexagonal plate with {111} panel and {100} edge. Besides the common stable surface such as {110}, {100}, {111}, the high index surface is also well studied. Shigang Sun and co-workers have using square-wave potential treatment to synthesize a series of Pt nanoparticles with different high index surface (e.g., {522}, {730}), which exhibit higher activity in electrooxidation of formic acid and ethanol than catalysts with low index surface.

1.5 Design of nanoparticles for electrocatalysis

In this section, I will mainly discuss the fundamental and designing principle of the 3 types of nanomaterials (i.e., Pt-based intermetallic nanoparticles, Metal-organic framework (MOF)-

derived carbon, and Mxenes) used in my Ph.D. research, and thus provide a general idea about the achievement in this field.

Pt-based intermetallic nanoparticles

Intermetallic, also known as intermetallic compounds, long-range ordered alloys, contains defined stoichiometry and ordered crystal structures. Enhanced electrocatalytic activity and selectivity is observed after random alloys are converted to intermetallics, due to the modification of electronic structure and the isolation of active sites. Besides, intermetallic nanoparticles exhibit better stability under harsh reaction conditions and show better tolerance towards oxidative etching. Intermetallics are more thermodynamically favored than random alloys with same compositions due to their ordered crystal structures. However, bimetallic alloys are usually obtained in the wet-chemistry synthesis, while only a few examples of intermetallic compounds are directly synthesized from solvothermal methods. This is mainly because the high activation energy barrier required for forming of intermetallics cannot be met by relatively low temperatures applied in wet-chemistry synthesis. From a thermodynamic point of view, the formation of ordered intermetallic from disordered phases is determined by the changes in Gibbs' free energy $\Delta G_{d\rightarrow o}$. The change in enthalpy $\Delta H_{d\rightarrow o}$ is negative due to the higher bonding order of intermetallics while the change in entropy $\Delta S_{d\rightarrow o}$ is also negative because of the more ordered structures. Therefore, ΔH is dominated in ΔG at low temperature, but $-T\Delta S$ is dominated at high temperatures. Besides, the transition temperature could be calculated when $\Delta G_{d\rightarrow o} = 0$.

When it comes to the nanomaterials that have a high surface area to volume ratio, the surface free energy should also be included into the total free energy. In a recent review, the change in Gibbs' free energy of a nanocrystal between disordered and ordered phases ($\Delta G_{d\rightarrow o}^{nano}$) is presented as:[61]

$$\Delta G_{d\to o}^{nano} = \Delta H_{d\to o} - T\Delta S_{d\to o} + \Delta\gamma_{d\to o}A$$

where $\Delta\gamma_{d\to o}$ is the specific surface free energy and A is the surface area of the nanocrystal. The author then compared the transition temperatures of nanomaterials ($T_{d\to o}^{nano}$) and bulks($T_{d\to o}^{bulk}$):

$$\frac{T_{d\to o}^{nano}}{T_{d\to o}^{bulk}} = 1 + (\frac{A}{V})\frac{\Delta\gamma_{d\to o}}{\Delta H_{d\to o,V}}$$

where $\Delta H_{d\to o,V}$ is the volume-specific bulk enthalpy, which is a negative value. At the same time, $\Delta\gamma_{d\to o}$ is positive as it requires more energy to form an ordered new surface. Therefore, the smaller nanoparticles with larger surface area to volume ratio will have lower transition temperatures, which is also thermodynamically favored. The effect of small particle size on kinetics generally has two opposite impacts: 1) unfavorable higher surface energy induced by more surface areas; 2) lower diffusion barrier to overcome. Therefore, an optimal size range might exist for the formation of interemtallics from the kinetic point of view.[61]

As has been mentioned before, the intermetallics synthesis via solvothermal method only works for limited cases, which are highly dependent on the components. Schaak reported a seed-mediated growth method to synthesize M-Zn (M = Au, Cu, Pd) nanocrystals in an organoamine solvent at 230- 260 ˚C.[62] The synthesis of Au-Cu intermetallic nanoparticles (i.e., Au_3Cu, AuCu, and $AuCu_3$) have been reported below 300 ˚C by different research groups.[63-65] For Pt-based intermetallic compounds, Pt_3Sn, PtSn, and $PtSn_2$ were successfully synthesized in TEG at 225-280 ˚C.[66] Pt_3Zn, Pt_3Co and $PtCu_3$ with the same space group of Pm-3m were obtained via wet-chemistry synthesis.[67-69] Although the possible intermetallic composition is limited via wet-chemistry synthesis, it leaves the possibility to finely tune the shape and morphology of intermetallic nanoparticles (e.g., cage, cube, rod, plate, wire).[60,67,70]

Annealing method is used to synthesize intermetallics with a wider range of compositions. Disordered alloys and core-shell nanocrystals are first synthesized via seed-mediated growth and/or co-reduction, and then converted to intermetallics by annealing in reducing or inert atmosphere around their transition temperatures, which typically are above 500 ℃.[61] Intermetallic nanoparticles such as PtFe, PtZn, PtMn, PtCo have been successfully synthesized via this methodology.[71-73] However, annealing at high temperature will lead to the inevitable aggregation of nanoparticles, which hampers their application in catalysis. Therefore, intermetallic nanoparticles are usually deposited onto inert supports or encapsulated in inorganic shells to gain extra thermal stability under annealing.[61]

The electrocatalytic performance of Pt/Pd-based alloys and intermetallics have been well investigated in oxygen reduction reaction, methanol oxidation reaction, ethanol oxidation reaction, formic acid oxidation reaction.[42] So far, Pt_3Ni shows the best performance towards ORR in an acidic electrolyte, and its ORR activity could be further improved by doping transition metals or shape control (e.g., nanoframes).[57-59] PtRu has superior activity and high tolerance towards CO poisoning in methanol oxidation reaction and formic acid reaction.[74] Ru is able to generate oxygen-containing spices at relatively low potential, which are on the sites adjacent to Pt sites, assisting to further oxidize CO intermediates. With similar mechanism, PtSn shows the higher activity towards ethanol oxidation than other intermetallic compounds.[75] Electrochemists now are more focused on the size control and morphology control to further lower the usage of noble metals, increase the active sites and enhance the intrinsic activity.[46,76]

MOF-derived carbon nanostructures

Metal-organic frameworks (MOFs) are crystalline porous materials consisting of metal ions or clusters and rigid organic linkers.[77-80] Due to their intriguing chemical/structural flexibility,

more than 20000 MOF structures have been reported via varying metal ions, linkers, and their interactions.[81-82] MOFs have been gaining extensive research interests due to their great potential in various applications, such as gas storage,[83] sensing,[84] separation,[85] imaging,[86] photoluminescence,[87] proton conductivity,[88] and catalysis.[89] However, many MOFs are relatively less stable in harsh conditions, such as acidic/basic solution, high temperatures.[90] Starting from the last decade, MOFs have been used as precursors to prepare porous carbon nanomaterials and metal (oxide)/carbon nanocomposites via pyrolysis under high temperatures.[91] Interestingly, the porosity, long-range structural ordering and sometimes the morphology of the parent MOFs are usually well preserved. [92] Moreover, the stability of those MOF-derived nanocomposites are greatly enhanced, making them more suitable catalysts for reactions under harsh conditions such as the Fischer-Tropsch synthesis,[93] hydrogenation,[94] oxidation,[95] and electrocatalytic reactions.[96-97]

The heteroatom-doped carbon materials, transition metal/metal oxides, metal carbides/nitrides derived from MOFs have been reported as active catalysts for ORR,[98-100] water splitting,[101-102] and CO_2 reduction.[103] These MOF-derived nanomaterials mostly inherit the high surface area, tunable porosity and facial functionalization with heteroatoms from the organic ligands.[77] Very recently, various single-atom catalysts were synthesized from MOF materials and reported with enhanced electrocatalytic performance.[104] The metal atoms are well dispersed and stabilized, due to the large surface area and high density of functional groups of the derived carbon.[105-106]

Two-dimensional MXenes nanosheets

MXenes are a class of 2D layered transition metal carbides, nitrides or carbonitrides derived from MAX phases via selective etching away "A" elements.[107] The parent MAX phases with the chemical formula $M_{n+1}AX_n$ and symmetry group $P6_3/mmc$ consists of an early transition

metal M (Sc, Ti, V, Cr, Zr, Nb, Mo, Hf, and Ta), an elemental A from groups 13-16 (Al, Si, P, S, F, Ga, In, and Sn), and X representing carbon and/or nitrogen.[108] As the bonding between elements A and M is weaker than those between elements M and X, Mxenes could be chemically exfoliated by acid washing (such as HF), and thus the F, O, and OH-terminated MXenes are obtained.[109] Because of their high chemical stability, tunable electronic functionality, controllable layer thickness, and functionalized surface, MXenes are appealing 2D systems with extensive applications in Li-ion batteries,[110-111] supercapacitors,[112-113] substrates for dyes, [114] hybrid nanocomposites, [36-38] and catalysis.[36,115-116] DFT calculation results indicate the O-terminated Mxenes are a good candidate for HER while few examples have been reported that Mxenes could be directly used as active electrocatalysts. Therefore, the study of MXenes and their composites in catalysis and energy conversion has an auspicious future. In chapter 4, I will present the preliminary data of the synthesis and electrochemical activity of MXenes supported noble metal alloy particles.

1.6 References

1. Electrochemistry, Past and Present, Copyright, ACS Symposium Series, Foreword. In *Electrochemistry, Past and Present*, American Chemical Society: 1989; Vol. 390, pp i-iv.

2. Stock, J. T., Electrochemistry in Retrospect. In *Electrochemistry, Past and Present*, American Chemical Society: 1989; Vol. 390, pp 1-17.

3. James, F. A. J. L., Michael Faraday's First Law of Electrochemistry. In *Electrochemistry, Past and Present*, American Chemical Society: 1989; Vol. 390, pp 32-49.

4. Appleby, A. J. *Journal of Power Sources* **1990,** *29* (1), 3-11.

5. von Smolinski, A. W.; Moore, C. E.; Jaselskis, B., The Choice of the Hydrogen Electrode as the Base for the Electromotive Series. In *Electrochemistry, Past and Present*, American Chemical Society: 1989; Vol. 390, pp 127-141.

6. Archer, M. D., Genesis of the Nernst Equation. In *Electrochemistry, Past and Present*, American Chemical Society: 1989; Vol. 390, pp 115-126.

7. Hudson, J. L.; Tsotsis, T. T. *Chemical Engineering Science* **1994,** *49* (10), 1493-1572.

8. Bard, A. J.; Faulkner, L. R., *Electrochemcial methods: fundamentals and applications 2nd Edition*. John Wiley&Sons, Inc.: New York, 2001.

9. Shinozaki, K.; Zack, J. W.; Richards, R. M.; Pivovar, B. S.; Kocha, S. S. *Journal of The Electrochemical Society* **2015,** *162* (10), F1144-F1158.

10. Yajima, T.; Uchida, H.; Watanabe, M. *The Journal of Physical Chemistry B* **2004,** *108* (8), 2654-2659.

11. Cuesta, A.; Escudero, M.; Lanova, B.; Baltruschat, H. *Langmuir* **2009,** *25* (11), 6500-6507.

12. Castel, E.; Berg, E. J.; El Kazzi, M.; Novák, P.; Villevieille, C. *Chemistry of Materials* **2014,** *26* (17), 5051-5057.

13. Wolter, O.; Willsau, J.; Heitbaum, J. *Journal of The Electrochemical Society* **1985,** *132* (7), 1635-1638.

14. Stamenkovic, V.; Mun, B. S.; Mayrhofer, K. J. J.; Ross, P. N.; Markovic, N. M.; Rossmeisl, J.; Greeley, J.; Nørskov, J. K. *Angewandte Chemie* **2006,** *118* (18), 2963-2967.

15. Greeley, J.; Stephens, I. E. L.; Bondarenko, A. S.; Johansson, T. P.; Hansen, H. A.; Jaramillo, T. F.; Rossmeisl, J.; Chorkendorff, I.; Nørskov, J. K. *Nature Chemistry* **2009,** *1*, 552.

16. Shao, M.; Chang, Q.; Dodelet, J.-P.; Chenitz, R. *Chemical Reviews* **2016,** *116* (6), 3594-3657.

17. Marković, N. M.; Schmidt, T. J.; Stamenković, V.; Ross, P. N. *Fuel Cells* **2001,** *1* (2), 105-116.

18. Dai, L.; Xue, Y.; Qu, L.; Choi, H.-J.; Baek, J.-B. *Chemical Reviews* **2015,** *115* (11), 4823-4892.

19. Liu, Y.; Kelly, T. G.; Chen, J. G.; Mustain, W. E. *ACS Catalysis* **2013,** *3* (6), 1184-1194.

20. Siahrostami, S.; Verdaguer-Casadevall, A.; Karamad, M.; Deiana, D.; Malacrida, P.; Wickman, B.; Escudero-Escribano, M.; Paoli, E. A.; Frydendal, R.; Hansen, T. W.; Chorkendorff, I.; Stephens, I. E. L.; Rossmeisl, J. *Nature Materials* **2013,** *12*, 1137.

21. Turrens, J. F. *The Journal of Physiology* **2003,** *552* (Pt 2), 335-344.

22. Zhao, Q.; Yan, Z.; Chen, C.; Chen, J. *Chemical Reviews* **2017,** *117* (15), 10121-10211.

23. Shinagawa, T.; Garcia-Esparza, A. T.; Takanabe, K. *Scientific Reports* **2015,** *5*, 13801.

24. Holewinski, A.; Linic, S. *Journal of The Electrochemical Society* **2012,** *159* (11), H864-H870.

25. Tripković, V.; Skúlason, E.; Siahrostami, S.; Nørskov, J. K.; Rossmeisl, J. *Electrochimica Acta* **2010,** *55* (27), 7975-7981.

26. Nørskov, J. K.; Rossmeisl, J.; Logadottir, A.; Lindqvist, L.; Kitchin, J. R.; Bligaard, T.; Jónsson, H. *The Journal of Physical Chemistry B* **2004,** *108* (46), 17886-17892.

27. Marković, N. M.; Ross, P. N. *Surface Science Reports* **2002,** *45* (4), 117-229.

28. Taylor, R. J.; Humffray, A. A. *Journal of Electroanalytical Chemistry and Interfacial Electrochemistry* **1975,** *64* (1), 85-94.

29. Taylor, R. J.; Humffray, A. A. *Journal of Electroanalytical Chemistry and Interfacial Electrochemistry* **1975,** *64* (1), 63-84.

30. Binninger, T.; Fabbri, E.; Kötz, R.; Schmidt, T. J. *Journal of The Electrochemical Society* **2014,** *161* (3), H121-H128.

31. Gao, S.; Sun, Z.; Liu, W.; Jiao, X.; Zu, X.; Hu, Q.; Sun, Y.; Yao, T.; Zhang, W.; Wei, S.; Xie, Y. *Nature Communications* **2017,** *8*, 14503.

32. Seh, Z. W.; Kibsgaard, J.; Dickens, C. F.; Chorkendorff, I.; Nørskov, J. K.; Jaramillo, T. F. *Science* **2017,** *355* (6321).

33. Zheng, Y.; Jiao, Y.; Jaroniec, M.; Qiao, S. Z. *Angewandte Chemie International Edition* **2015,** *54* (1), 52-65.

34. Vesborg, P. C. K.; Seger, B.; Chorkendorff, I. *The Journal of Physical Chemistry Letters* **2015,** *6* (6), 951-957.

35. Vij, V.; Sultan, S.; Harzandi, A. M.; Meena, A.; Tiwari, J. N.; Lee, W.-G.; Yoon, T.; Kim, K. S. *ACS Catalysis* **2017,** *7* (10), 7196-7225.

36. Pandey, M.; Thygesen, K. S. *The Journal of Physical Chemistry C* **2017,** *121* (25), 13593-13598.

37. Zheng, Y.; Jiao, Y.; Zhu, Y.; Li, L. H.; Han, Y.; Chen, Y.; Jaroniec, M.; Qiao, S.-Z. *Journal of the American Chemical Society* **2016,** *138* (49), 16174-16181.

38. Li, G.; Zhang, D.; Qiao, Q.; Yu, Y.; Peterson, D.; Zafar, A.; Kumar, R.; Curtarolo, S.; Hunte, F.; Shannon, S.; Zhu, Y.; Yang, W.; Cao, L. *Journal of the American Chemical Society* **2016,** *138* (51), 16632-16638.

39. Pandey, M.; Vojvodic, A.; Thygesen, K. S.; Jacobsen, K. W. *The Journal of Physical Chemistry Letters* **2015,** *6* (9), 1577-1585.

40. Greeley, J.; Jaramillo, T. F.; Bonde, J.; Chorkendorff, I.; Nørskov, J. K. *Nature Materials* **2006,** *5*, 909.

41. Zheng, Y.; Jiao, Y.; Zhu, Y.; Li, L. H.; Han, Y.; Chen, Y.; Du, A.; Jaroniec, M.; Qiao, S. Z. *Nature Communications* **2014,** *5*, 3783.

42. Chen, A.; Holt-Hindle, P. *Chemical Reviews* **2010,** *110* (6), 3767-3804.

43. Wasmus, S.; Küver, A. *Journal of Electroanalytical Chemistry* **1999,** *461* (1), 14-31.

44. Maillard, F.; Gloaguen, F.; Leger, J. M. *Journal of Applied Electrochemistry* **2003,** *33* (1), 1-8.

45. Ghosh, T.; Matsumoto, F.; McInnis, J.; Weiss, M.; Abruña, H. D.; DiSalvo, F. J. *Journal of Nanoparticle Research* **2009,** *11* (4), 965-980.

46. Qi, Z.; Xiao, C.; Liu, C.; Goh, T. W.; Zhou, L.; Maligal-Ganesh, R.; Pei, Y.; Li, X.; Curtiss, L. A.; Huang, W. *Journal of the American Chemical Society* **2017,** *139* (13), 4762-4768.

47. Kang, Y.; Pyo, J. B.; Ye, X.; Gordon, T. R.; Murray, C. B. *ACS Nano* **2012,** *6* (6), 5642-5647.

48. Popczun, E. J.; McKone, J. R.; Read, C. G.; Biacchi, A. J.; Wiltrout, A. M.; Lewis, N. S.; Schaak, R. E. *Journal of the American Chemical Society* **2013,** *135* (25), 9267-9270.

49. Lefèvre, M.; Proietti, E.; Jaouen, F.; Dodelet, J.-P. *Science* **2009,** *324* (5923), 71.

50. Debe, M. K. *Nature* **2012,** *486*, 43.

51. Li, M.; Zhao, Z.; Cheng, T.; Fortunelli, A.; Chen, C.-Y.; Yu, R.; Zhang, Q.; Gu, L.; Merinov, B.; Lin, Z.; Zhu, E.; Yu, T.; Jia, Q.; Guo, J.; Zhang, L.; Goddard, W. A.; Huang, Y.; Duan, X. *Science* **2016**.

52. Kim, D.; Resasco, J.; Yu, Y.; Asiri, A. M.; Yang, P. *Nature Communications* **2014,** *5*, 4948.

53. Gilroy, K. D.; Ruditskiy, A.; Peng, H.-C.; Qin, D.; Xia, Y. *Chemical Reviews* **2016,** *116* (18), 10414-10472.

54. Sankar, M.; Dimitratos, N.; Miedziak, P. J.; Wells, P. P.; Kiely, C. J.; Hutchings, G. J. *Chem Soc Rev* **2012,** *41* (24), 8099-8139.

55. Skúlason, E.; Tripkovic, V.; Björketun, M. E.; Gudmundsdóttir, S.; Karlberg, G.;

Rossmeisl, J.; Bligaard, T.; Jónsson, H.; Nørskov, J. K. *The Journal of Physical Chemistry C* **2010,** *114* (42), 18182-18197.

56. Casado-Rivera, E.; Gál, Z.; Angelo, A. C. D.; Lind, C.; DiSalvo, F. J.; Abruña, H. D. *ChemPhysChem* **2003,** *4* (2), 193-199.

57. Stamenkovic, V. R.; Fowler, B.; Mun, B. S.; Wang, G.; Ross, P. N.; Lucas, C. A.; Marković, N. M. *Science* **2007,** *315* (5811), 493.

58. Huang, X.; Zhao, Z.; Cao, L.; Chen, Y.; Zhu, E.; Lin, Z.; Li, M.; Yan, A.; Zettl, A.; Wang, Y. M.; Duan, X.; Mueller, T.; Huang, Y. *Science* **2015,** *348* (6240), 1230.

59. Chen, C.; Kang, Y.; Huo, Z.; Zhu, Z.; Huang, W.; Xin, H. L.; Snyder, J. D.; Li, D.; Herron, J. A.; Mavrikakis, M.; Chi, M.; More, K. L.; Li, Y.; Markovic, N. M.; Somorjai, G. A.; Yang, P.; Stamenkovic, V. R. *Science* **2014,** *343* (6177), 1339.

60. Bu, L.; Zhang, N.; Guo, S.; Zhang, X.; Li, J.; Yao, J.; Wu, T.; Lu, G.; Ma, J.-Y.; Su, D.; Huang, X. *Science* **2016,** *354* (6318), 1410.

61. Yan, Y.; Du, J. S.; Gilroy, K. D.; Yang, D.; Xia, Y.; Zhang, H. *Advanced Materials* **2017,** *29* (14), 1605997-n/a.

62. Cable, R. E.; Schaak, R. E. *Chemistry of Materials* **2007,** *19* (16), 4098-4104.

63. Wang, G.; Huang, B.; Xiao, L.; Ren, Z.; Chen, H.; Wang, D.; Abruña, H. D.; Lu, J.; Zhuang, L. *Journal of the American Chemical Society* **2014,** *136* (27), 9643-9649.

64. Zhang, N.; Chen, X.; Lu, Y.; An, L.; Li, X.; Xia, D.; Zhang, Z.; Li, J. *Small* **2014,** *10* (13), 2662-2669.

65. Wang, G.; Xiao, L.; Huang, B.; Ren, Z.; Tang, X.; Zhuang, L.; Lu, J. *Journal of Materials Chemistry* **2012,** *22* (31), 15769-15774.

66. Wang, X.; Altmann, L.; Stöver, J.; Zielasek, V.; Bäumer, M.; Al-Shamery, K.; Borchert, H.; Parisi, J.; Kolny-Olesiak, J. *Chemistry of Materials* **2013,** *25* (8), 1400-1407.

67. Chen, Q.; Zhang, J.; Jia, Y.; Jiang, Z.; Xie, Z.; Zheng, L. *Nanoscale* **2014,** *6* (12), 7019-7024.

68. Bu, L.; Guo, S.; Zhang, X.; Shen, X.; Su, D.; Lu, G.; Zhu, X.; Yao, J.; Guo, J.; Huang, X. *Nature Communications* **2016,** *7*, 11850.

69. Xia, B. Y.; Wu, H. B.; Wang, X.; Lou, X. W. *Journal of the American Chemical Society* **2012,** *134* (34), 13934-13937.

70. Jana, S.; Chang, J. W.; Rioux, R. M. *Nano Letters* **2013,** *13* (8), 3618-3625.

71. Ghosh, T.; Leonard, B. M.; Zhou, Q.; DiSalvo, F. J. *Chemistry of Materials* **2010,** *22* (7), 2190-2202.

72. Du, X. X.; He, Y.; Wang, X. X.; Wang, J. N. *Energy & Environmental Science* **2016,** *9* (8), 2623-2632.

73. Casado-Rivera, E.; Volpe, D. J.; Alden, L.; Lind, C.; Downie, C.; Vázquez-Alvarez, T.; Angelo, A. C. D.; DiSalvo, F. J.; Abruña, H. D. *Journal of the American Chemical Society* **2004,** *126* (12), 4043-4049.

74. Chen, D.-J.; Tong, Y. J. *Angewandte Chemie International Edition* **2015,** *54* (32), 9394-9398.

75. Jiang, L.; Hsu, A.; Chu, D.; Chen, R. *International Journal of Hydrogen Energy* **2010,** *35* (1), 365-372.

76. Maligal-Ganesh, R. V.; Xiao, C.; Goh, T. W.; Wang, L.-L.; Gustafson, J.; Pei, Y.; Qi, Z.; Johnson, D. D.; Zhang, S.; Tao, F.; Huang, W. *ACS Catalysis* **2016,** *6* (3), 1754-1763.

77. Jiao, L.; Wang, Y.; Jiang, H.-L.; Xu, Q. *Advanced Materials*, 1703663-n/a.

78. Long, J. R.; Yaghi, O. M. *Chem Soc Rev* **2009,** *38* (5), 1213-1214.

79. Zhou, H.-C.; Long, J. R.; Yaghi, O. M. *Chemical Reviews* **2012,** *112* (2), 673-674.

80. Zhou, H. C.; Kitagawa, S. *Chem Soc Rev* **2014,** *43* (16), 5415-5418.

81. Furukawa, H.; Cordova, K. E.; O'Keeffe, M.; Yaghi, O. M. *Science* **2013,** *341* (6149), 974-+.

82. Stock, N.; Biswas, S. *Chemical Reviews* **2012,** *112* (2), 933-969.

83. Li, B.; Wen, H.-M.; Zhou, W.; Chen, B. *The Journal of Physical Chemistry Letters* **2014,** *5* (20), 3468-3479.

84. Lustig, W. P.; Mukherjee, S.; Rudd, N. D.; Desai, A. V.; Li, J.; Ghosh, S. K. *Chem Soc Rev* **2017,** *46* (11), 3242-3285.

85. Britt, D.; Furukawa, H.; Wang, B.; Glover, T. G.; Yaghi, O. M. *Proceedings of the National Academy of Sciences* **2009,** *106* (49), 20637.

86. Della Rocca, J.; Liu, D.; Lin, W. *Accounts of Chemical Research* **2011,** *44* (10), 957-968.

87. Cui, Y.; Yue, Y.; Qian, G.; Chen, B. *Chemical Reviews* **2012,** *112* (2), 1126-1162.

88. Zhang, F.-M.; Dong, L.-Z.; Qin, J.-S.; Guan, W.; Liu, J.; Li, S.-L.; Lu, M.; Lan, Y.-Q.; Su, Z.-M.; Zhou, H.-C. *Journal of the American Chemical Society* **2017,** *139* (17), 6183-6189.

89. Yang, Q.; Xu, Q.; Jiang, H.-L. *Chem Soc Rev* **2017,** *46* (15), 4774-4808.

90. Burtch, N. C.; Jasuja, H.; Walton, K. S. *Chemical Reviews* **2014,** *114* (20), 10575-10612.

91. Shen, K.; Chen, X.; Chen, J.; Li, Y. *ACS Catalysis* **2016,** *6* (9), 5887-5903.

92. Wang, H.; Zhu, Q.-L.; Zou, R.; Xu, Q. *Chem* **2017,** *2* (1), 52-80.

93. An, B.; Cheng, K.; Wang, C.; Wang, Y.; Lin, W. *ACS Catalysis* **2016,** *6* (6), 3610-3618.

94. Yang, J.; Zhang, F.; Lu, H.; Hong, X.; Jiang, H.; Wu, Y.; Li, Y. *Angewandte Chemie International Edition* **2015,** *54* (37), 10889-10893.

95. Bai, C.; Li, A.; Yao, X.; Liu, H.; Li, Y. *Green Chemistry* **2016,** *18* (4), 1061-1069.

96. Ren, Q.; Wang, H.; Lu, X.-F.; Tong, Y.-X.; Li, G.-R. *Advanced Science*, 1700515-n/a.

97. Cao, X.; Tan, C.; Sindoro, M.; Zhang, H. *Chem Soc Rev* **2017,** *46* (10), 2660-2677.

98. Zhao, S.; Yin, H.; Du, L.; He, L.; Zhao, K.; Chang, L.; Yin, G.; Zhao, H.; Liu, S.; Tang, Z. *ACS Nano* **2014,** *8* (12), 12660-12668.

99. Zhang, P.; Sun, F.; Xiang, Z.; Shen, Z.; Yun, J.; Cao, D. *Energy & Environmental Science* **2014,** *7* (1), 442-450.

100. Xia, W.; Zou, R.; An, L.; Xia, D.; Guo, S. *Energy & Environmental Science* **2015,** *8* (2), 568-576.

101. Xia, B. Y.; Yan, Y.; Li, N.; Wu, H. B.; Lou, X. W.; Wang, X. *Nature Energy* **2016,** *1*, 15006.

102. Chen, W.; Pei, J.; He, C.-T.; Wan, J.; Ren, H.; Zhu, Y.; Wang, Y.; Dong, J.; Tian, S.; Cheong, W.-C.; Lu, S.; Zheng, L.; Zheng, X.; Yan, W.; Zhuang, Z.; Chen, C.; Peng, Q.; Wang, D.; Li, Y. *Angewandte Chemie International Edition* **2017,** *56* (50), 16086-16090.

103. Zhao, K.; Liu, Y.; Quan, X.; Chen, S.; Yu, H. *ACS Applied Materials & Interfaces* **2017,** *9* (6), 5302-5311.

104. Chen, Y.; Ji, S.; Wang, Y.; Dong, J.; Chen, W.; Li, Z.; Shen, R.; Zheng, L.; Zhuang, Z.; Wang, D.; Li, Y. *Angewandte Chemie International Edition* **2017,** *56* (24), 6937-6941.

105. Wang, X.; Chen, Z.; Zhao, X.; Yao, T.; Chen, W.; You, R.; Zhao, C.; Wu, G.; Wang, J.; Huang, W.; Yang, J.; Hong, X.; Wei, S.; Wu, Y.; Li, Y. *Angewandte Chemie International*

Edition **2018,** *57* (7), 1944-1948.

106. Wang, J.; Huang, Z.; Liu, W.; Chang, C.; Tang, H.; Li, Z.; Chen, W.; Jia, C.; Yao, T.; Wei, S.; Wu, Y.; Li, Y. *Journal of the American Chemical Society* **2017,** *139* (48), 17281-17284.

107. Anasori, B.; Lukatskaya, M. R.; Gogotsi, Y. *Nature Reviews Materials* **2017,** *2*, 16098.
108. Ingason, A. S.; Dahlqvist, M.; Rosen, J. *Journal of Physics: Condensed Matter* **2016,** *28* (43), 433003.

109. Khazaei, M.; Ranjbar, A.; Arai, M.; Sasaki, T.; Yunoki, S. *Journal of Materials Chemistry C* **2017,** *5* (10), 2488-2503.

110. Byeon, A.; Zhao, M.-Q.; Ren, C. E.; Halim, J.; Kota, S.; Urbankowski, P.; Anasori, B.; Barsoum, M. W.; Gogotsi, Y. *ACS Applied Materials & Interfaces* **2017,** *9* (5), 4296-4300.
111. Tang, Q.; Zhou, Z.; Shen, P. *Journal of the American Chemical Society* **2012,** *134* (40), 16909-16916.

112. Yan, J.; Ren, C. E.; Maleski, K.; Hatter, C. B.; Anasori, B.; Urbankowski, P.; Sarycheva, A.; Gogotsi, Y. *Advanced Functional Materials* **2017,** *27* (30), 1701264-n/a.

113. Yang, Q.; Xu, Z.; Fang, B.; Huang, T.; Cai, S.; Chen, H.; Liu, Y.; Gopalsamy, K.; Gao, W.; Gao, C. *Journal of Materials Chemistry A* **2017,** *5* (42), 22113-22119.

114. Mashtalir, O.; Cook, K. M.; Mochalin, V. N.; Crowe, M.; Barsoum, M. W.; Gogotsi, Y. *Journal of Materials Chemistry A* **2014,** *2* (35), 14334-14338.

115. Pan, H. *Scientific Reports* **2016,** *6*, 32531.

116. Gao, G.; O'Mullane, A. P.; Du, A. *ACS Catalysis* **2017,** *7* (1), 494-500.

CHAPTER 2. SUB-4 NM PTZN INTERMETALLIC NANOPARTICLES FOR ENHANCED MASS AND SPECIFIC ACTIVITIES IN CATALYTIC ELECTO-OXIDATION REACTION

Modified from a publication in the Journal of American Chemical Society

J. Am. Chem. Soc., **2017**, 139 (13), 4762-4768

Zhiyuan Qi,[†] Chaoxian Xiao,[†] Cong Liu,[#] Tian-Wei Goh,[†] Lin Zhou,[‡] Raghu Maligal-Ganesh,[†] Yuchen Pei,[†] Xinle Li,[†] Larry A. Curtiss,[§] Wenyu Huang[*, †, ‡]

[†] Department of Chemistry, Iowa State University, Ames, Iowa, 50011, United States

[‡] Ames Laboratory, U.S. Department of Energy, Ames, Iowa, 50011, United States

[#] Chemical Sciences and Engineering Division, Argonne National Laboratory, Lemont, Illinois, 60439, United States

[§] Materials Science Division, Argonne National Laboratory, Lemont, Illinois, 60439, United States

2.1 Abstract

Atomically ordered intermetallic nanoparticles (iNPs) have sparked considerable interest in fuel cell applications by virtue of their exceptional electronic and structural properties. However, the synthesis of small iNPs in a controllable manner remains a formidable challenge because of the high temperature generally required in the formation of intermetallic phases. Here we report a general method for the synthesis of PtZn iNPs (3.2 ± 0.4 nm) on multi-walled carbon nanotubes (MWNT) via a facile and capping agent-free strategy using a sacrificial mesoporous silica ($mSiO_2$) shell. The as-prepared PtZn iNPs exhibited ca. 10 times higher mass activity in both acidic and basic solution towards the methanol oxidation reaction (MOR) compared to larger PtZn iNPs

synthesized on MWNT without the $mSiO_2$ shell. Density functional theory (DFT) calculations predict that PtZn systems go through a "non-CO" pathway for MOR because of the stabilization of the OH* intermediate by Zn atoms, while a pure Pt system forms highly stable COH* and CO* intermediates, leading to catalyst deactivation. Experimental studies on the origin of the backward oxidation peak of MOR coincide well with DFT predictions. Moreover, the calculations demonstrate that MOR on smaller PtZn iNPs is energetically more favorable than larger iNPs, due to their high density of corner sites and lower-lying energetic pathway. Therefore, smaller PtZn iNPs not only increase the number but also enhance the activity of the active sites in MOR than larger ones. This work opens a new avenue for the synthesis of small iNPs with more undercoordinated and enhanced active sites for fuel cell applications.

2.2 Introduction

Intermetallic nanomaterials, featuring atomically ordered crystal structures and unique electronic/structural properties, have been garnering increasing research attention in past decades. Tremendous endeavors have been devoted to the investigation of intermetallic nanomaterials, particularly Pt-based, as fuel cell electrocatalysts with the aim of decreasing Pt usage, increasing poisoning tolerance and improving the catalysts activities and stabilities. A great many scientific efforts have been devoted to the preparation of Pt-based alloys and intermetallic compounds, such as PtSn,[1] PtTi,[2-3] PtMn,[4-5] PtCo,[6-8] PtFe,[9-10] PtBi,[11-12] PtPb,[11,13] Pt_3Ni,[5,14] PtZn,[15-18] and PtCu,[19-22] in the electro-oxidation of methanol or formic acid and electro-reduction of oxygen.

Among aforementioned intermetallic compounds, PtZn iNPs have been proven as active catalysts toward formic acid and methanol electrooxidation.[15] Regarding the synthesis of intermetallic PtZn, DiSalvo et al. reported the synthesis of PtZn iNPs by reaction of Pt nanoparticles with Zn vapor, and Murray et al. demonstrated the formation of Pt_3Zn intermetallic

NCs. However, since the formation of the intermetallic phase usually requires the use of high-temperature annealing (e.g., 600 ℃ for Pt_3Zn),[16] the aggregation of nanoparticles, either unprotected or capped with organic capping agents, is unavoidable. The aggregation also adversely renders PtZn iNPs with a broad size distribution ranging from 3 to 15 nm.[15-17] The larger particles limit catalytic activity due to their low surface to volume ratio, and thus hamper the effective utilization of precious metals. The lack of size control can also complicate the product selectivity in size-sensitive reactions. Therefore, the development of a new synthetic strategy to obtain well-defined and small PtZn iNPs is highly desired. To the best of our knowledge, there is no general method available for the synthesis of small iNPs.

Herein, we report the synthesis of small and uniform PtZn iNPs (3.2 ± 0.4 nm) supported on a conductive support (MWNTs), and their electro-oxidation activity is largely enhanced beneficial from such small size and dramatic monodispersity. These PtZn iNPs are capping agent-free and thus have a strong metal-support interaction with MWNTs. We used the mesoporous silica ($mSiO_2$) shell to prevent iNPs from aggregation during the high-temperature annealing to form the PtZn intermetallic phase (denoted as PtZn/MWNT@$mSiO_2$). This strategy has not been applied to synthesis iNPs supported on conductive supports.[23-29] On the contrast, the unprotected PtZn nanoparticles supported on MNWTs (denoted as PtZn/MWNT) experienced severe aggregation during annealing, and the formed PtZn iNPs have an average diameter of 27 nm. DFT calculations and experimental results have proved that the smaller iNPs are energetically more favorable for methanol oxidation reaction (MOR) and thus have enhanced both specific and mass activities in comparison to larger iNPs synthesized by a traditional wetness impregnation method without the $mSiO_2$ capping shell.

2.3 Experimental Section

2.3.1 Synthesis of Pt (IV)/MWNT

For a typical synthesis of $Pt(OH)_4$/MNWT, 150 mg of urea was first dissolved in 100 mL DI water. We then added 100 mg MWNT into the solution. After sonication for 30 min, 2.5 mL of 0.05 M H_2PtCl_6 aqueous solution was carefully added and stirred for 3 h. The mixture was heated to 90 ℃ and kept for 12 h. After it was cooled to room temperature, the catalyst was filtered, washed with water and dried at 60 ℃ overnight.

2.3.2 Synthesis of Pt/MWNT@mSiO$_2$

In a typical synthesis, 160 mg of CTAB was added to a mixture containing 120 mL ethanol, 30 mL DI water and 1.5 mL of ammonia (28 wt.%). The as-prepared $Pt(OH)_4$/MWNT was dispersed into the above solution and sonicated for 30 min. Subsequently, 1 mL TEOS was added, and the mixture was stirred for 6 h at room temperature. The obtained product was collected by centrifuge, washed with ethanol 3 times and dried under vacuum at 60 ℃. The dried sample was transferred into a tube furnace and reduced at 240 ℃ for 2 h under 10% H_2/argon flow. The sample was further purified by ion exchange (2.0 g of NH_4NO_3 in 120 mL of ethanol) to remove surfactants. The loading of Pt was measured by ICP-MS as 3.1 ± 0.1 wt.%.

2.3.3 Synthesis of PtZn/MWNT@mSiO$_2$

Pt/MWNT@$mSiO_2$ and $Zn(acac)_2$ (molar ratio of Pt/Zn =1) was dispersed into 15 mL oleylamine and 2.5 mL oleic acid mixture solution under argon atmosphere. The solution was heated to 330 ℃ and kept for 1 h. After it was cooled back to room temperature, the product was collected by centrifuge, washed with hexane 5 times and dried under vacuum at 60 ℃. The dried black powder was further annealed in a tube furnace at 600 ℃ for 2 h under 10% H_2/argon flow.

2.3.4 Synthesis of PtZn/MWNT control catalyst

8.6 nm PtZn/MWNT control catalyst was prepared by following the same procedure in 1.1. After $Pt(OH)_4$/MWNT was obtained, the sample was directly reduced at 240 ℃ for 2 h under 10% H_2/argon flow. The resultant 3.7 nm Pt/MWNT was used as seed and convert to PtZn/MWNT following the procedure in 1.3.

27 nm PtZn/MWNT control catalyst was prepared by wetness impregnation. In a typical synthesis, 100 mg of MWNT was dispersed into 50 mL of water and isopropanol mixture solvent (volume ratio of water/isopropanol = 1). K_2PtCl_4 and $ZnCl_2$ (molar ratio Pt/Zn =1) was added into the above solution and sonicate for 2 h while the Pt amount was controlled as 10 wt. %. The solution was heated to 60 ℃ and slowly evaporated under stirring. The dried sample was ground and transferred into a tube furnace and anneal at 600 ℃ for 2 h under 10 % H_2/argon flow.

2.3.5 Characterization

All the samples were characterized by powder XRD at room temperature using a STOE Stadi P powder diffractometer equipped with an image plate and a Cu Kα1 radiation source (λ = 1.5406 Å). TEM was carried out using a TECNAI G2 F20 operated at 200 kV. High-resolution HAADF STEM imaging was performed on a Titan Themis 300 probe corrected TEM with a Super-X EDX detector from Sensitive Instrument Facility of Ames Lab. BET Surface area measurements were performed by nitrogen sorption isotherms using a Micromeritics 3Flex surface characterization analyzer at 77 K. ICP-MS was measured by Thermo Fisher Scientific X Series 2 ICP-MS. Typically, solid samples were dissolved in $HClO_4$ to digest carbon after 100 μL of 30% HF solution was added to remove the $mSiO_2$ shell. XPS measurements were performed using a PHI 5500 Multitechnique system (Physical Electronics, Chanhassen, MN) with a monochromatized Al Kα X-ray source ($h\nu$ = 1486.6 eV)

2.3.6 Electrochemical measurements

All electrochemical measurements were performed in a three-electrode system using a potentiostat (VSP-300, Bio-Logic Science Instruments). Catalysts were loaded onto a rotational ring-disk electrode (RRDE, 5 mm), which is used as a working electrode. A platinum wire was used as the counter electrode, and a saturated Ag/AgCl electrode was used as the reference electrode. The electrochemical active surface area (ECSA) measurements in acidic condition were cycled from -0.05 V to 1.05 V vs. RHE at a sweep speed of 50 mV/s in 0.1 M perchloric acid solution until stable cyclic voltammetry (CV) curves were obtained. ECSA measurements in basic condition were carried out in 0.1 M potassium hydroxide solution and cycled from 0 V to 1.25 V vs. RHE at a sweep speed of 50 mV/s. The reactor was purged with argon before ECSA tests for 30 min in both cases. The ECSA was determined by integrating the adsorption of hydrogen between 0.05 and 0.4 V and assuming 210 μc/cm^2 is required for removing a monolayer of adsorbed hydrogen from Pt surface. All water used in the experiments was Millipore ultrapure water (18.2 MΩ).

All measurements of electro-oxidation of methanol were carried out at room temperature. The alkaline electrooxidation of methanol was done in a 0.1 M KOH + 0.5 M methanol solution while methanol oxidation in acid solution was carried out in a 0.5 M H_2SO_4 + 1 M methanol solution. The sweep speed was 50 mV/s if not specified.

2.3.7 Preparation of electrode

For MWNT supported catalysts, the samples were dispersed into a solvent mixture (H_2O: Isopropanol: 5% Nafion solution = 4: 1: 0.025), and the concentration of these supported catalysts was adjusted to 2 mg/mL. After sonication for 30 min, 10 μL of the catalyst ink was transferred onto a glass carbon RRDE (5 mm in diameter). For a Pt/Vulcan commercial catalyst, an aqueous

solution (0.5 mg /1 mL) was prepared and sonicated for 30 min. We then applied 20 μL of above catalyst ink onto the electrode.

2.3.8. DFT calculation

Density functional theory calculations were performed on the electrocatalytic reactions of methanol electro-oxidation reaction on PtZn and Pt materials. PtZn (111), stepped PtZn (211), $Pt_{24}Zn_{24}$ cluster and Pt (111) surface were taken into account. All the calculations were carried out using the PBE function[1] with a plane wave basis set implemented in the Vienna Ab initio Simulation Package (VASP), version 5.3.3).[2-5] The energy cutoff of 400 eV was used, and the Γ-point and a 3 × 3 × 1 k-point mash were used to sample the Brillouin zones for the molecules/clusters and surface systems, respectively. For both PtZn (111) and Pt (111), a unit cell with 4 × 4 × 4 metal atoms was built, and the unit cell of the stepped PtZn (211) contains 18 Pt and 18 Zn atoms. A 10 Å vacuum space above the surface was created to separate the surface slab and its periodic image. $Pt_{24}Zn_{24}$ was placed in a 20 × 20 × 20 Å box.

A reaction network containing 15 intermediates for possible electrochemical and chemical reactions was analyzed to identify the most favorable electrochemical reaction pathway for each of the four considered metal systems (Figure S13). 4-10 conformations were taken into account for each intermediate state for all the systems, and the lowest energy conformation was identified for each intermediate and used to calculate the reaction energies.

2.4 Results and Discussion

The preparation of MWNT supported PtZn iNPs was summarized in Figure 1a. $Pt(OH)_4$/MWNT@$mSiO_2$ was prepared using the precipitation-deposition method followed by $mSiO_2$ coating and H_2 reduction to form Pt/MWNT@$mSiO_2$. A Zn precursor was introduced into the Pt/MWNT@$mSiO_2$ to form $mSiO_2$-encapsulated PtZn alloy nanoparticles.[28] After separating the alloy nanoparticles from the solution, we annealed them at 600 ℃ to form the ordered iNP

PtZn/MWNT@$mSiO_2$. Finally, the insulating $mSiO_2$ shell was etched to test the PtZn/MWNT for electrocatalytic MOR.

To deposit Pt onto MWNT, chloroplatinic acid (H_2PtCl_6), MWNT and urea aqueous mixtures were heated to 90 ℃, at which temperature urea slowly decomposed to generate hydroxide ions (OH^-). The OH^- ions homogeneously precipitated Pt(IV) onto MWNT (denoted as $Pt(OH)_4$/MWNT).[30] The pH of the solution changed from 3 to 8, indicating the successful decomposition of urea and precipitation of Pt ions. The $mSiO_2$ shell was then coated on the $Pt(OH)_4$/MWNT by a sol-gel method using cetyltrimethylammonium bromide (CTAB) as the pore-directing agent. Figure 1b shows transmission electron microscopy (TEM) images of the pristine MWNT with an outer diameter in the range of 30-50 nm. After loading $Pt(OH)_4$, a 15 nm thick $mSiO_2$ shell was uniformly coated on MWNTs (Figure 1c). The deposited $Pt(OH)_4$ species was further reduced by 50 mL/min of 10% H_2 in an argon flow at 240 ℃ to form Pt nanoparticles. After removing CTAB surfactants by methanol refluxing to open the channels in the $mSiO_2$ shell, Pt/MWNT@$mSiO_2$ was obtained (Figure 1d). With the $mSiO_2$ shell inhibiting the aggregation, as-form Pt nanoparticles have an average diameter of 2.1 ± 0.3 nm (Figure S2a). These Pt nanoparticles were also evenly dispersed at the interface between the MWNT and $mSiO_2$ shell (Figure 1d), which indicates a strong interaction between Pt and MWNT. To prove this strong interaction, a control sample was prepared by loading polyvinylpyrrolidone (PVP)-capped Pt nanoparticles onto MWNT, followed by silica coating. As shown in Figure S3b, many Pt particles were not well confined at the interface between MWNT and $mSiO_2$, which could be easily detached from MWNT during etching.

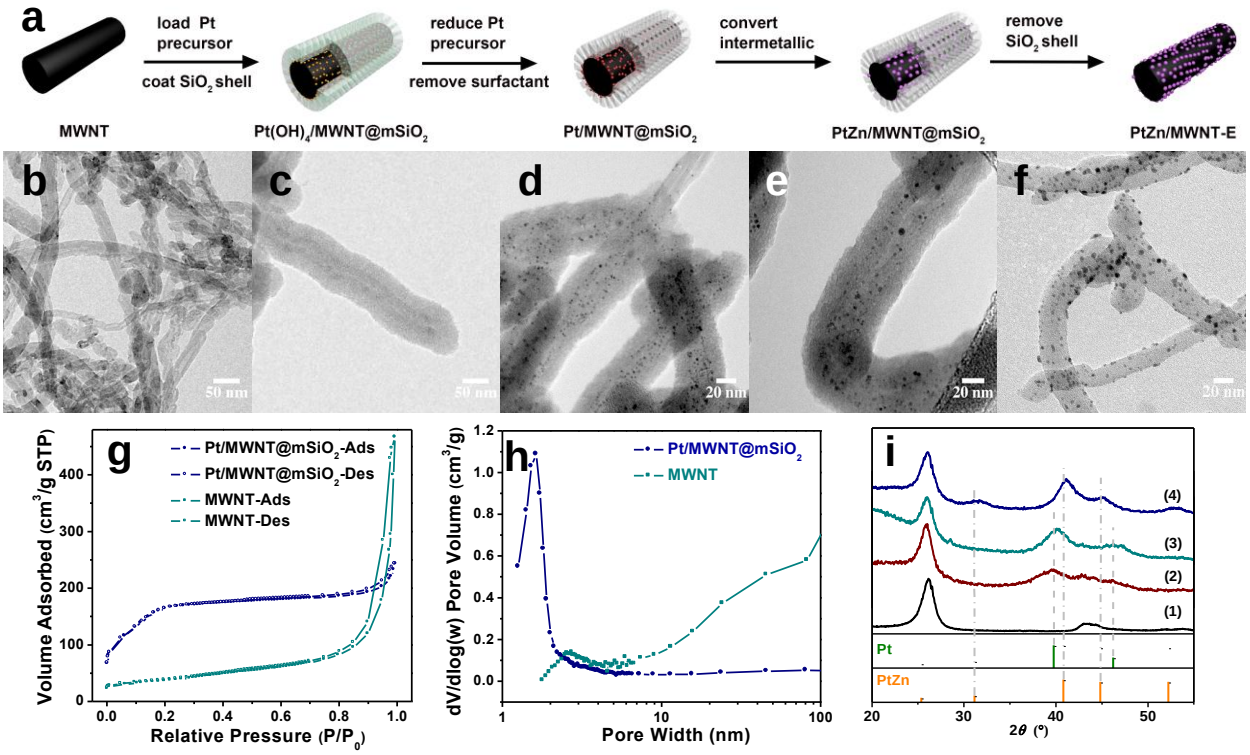

Figure 1. (a) Schematic representation of the synthesis route to PtZn/MWNT@mSiO$_2$. (b-f) TEM images of (b) pristine MWNT, (c) Pt(OH)$_4$/MWNT@SiO$_2$ formed after loading Pt and coating silica, (d) Pt/MWNT@mSiO$_2$ after H_2 reduction, (e) PtZn/MWNT@mSiO$_2$ prepared by annealing at 600 ℃, and (f) PtZn/MWNT-E after etching away the mSiO$_2$ shell. (g) Nitrogen adsorption and desorption isotherm of MWNT and Pt/MWNT@mSiO$_2$. (h) BJH pore size distribution of MWNT and Pt/MWNT@mSiO$_2$. (i) PXRD patterns of (i-1) pristine MWNT, (i-2) Pt/MWNT@mSiO$_2$ reduced at 240 ℃, (i-3) PtZn/MWNT@mSiO$_2$ prepared by solvothermal synthesis at 330 ℃, and (i-4) PtZn/MWNT@mSiO$_2$ annealed at 600 ℃.

N_2 sorption was measured to verify the mesoporous structure of the mSiO$_2$ shell (Figure 1g). Pristine MWNT shows weak adsorption of N_2 at lower relative pressure (P/P_0) until P/P_0 = 0.8 where an upward adsorption occurs, which leads to a small Brunauer-Emmett-Teller (BET) surface area of 129 m^2/g. After coating the mSiO$_2$ shell on the MWNT, the BET surface area of

Pt/MWNT@$mSiO_2$ increases to 633 m^2/g. Pt/MWNT@$mSiO_2$ exhibits a type-IV isotherm with a small capillary condensation step, indicating the existence of a mesoporous structure of the $mSiO_2$ shell. Based on the Barrett-Joyner-Halenda (BJH) pore size distribution (Figure 1h) the average pore diameter of the $mSiO_2$ is 1.8 nm, with a small amount of mesopores. The average pore diameter of the $mSiO_2$ shell matches the size of formed Pt nanoparticles, which suggests that the mesopore in the $mSiO_2$ shell restricts the growth of the confined Pt nanoparticles under reduction.

To introduce Zn, the Pt/MWNT@$mSiO_2$ was redispersed with $Zn(acac)_2$ (Pt:Zn molar ratio = 1:1) in oleic acid and oleylamine mixture, heated to 330 ℃ and maintained at this temperature for 1 h. The reaction was monitored by powder X-ray diffraction (PXRD) as shown in Figure 1i. At 330 ℃, we observed the formation of PtZn alloy nanoparticles. Only after annealing at 600 ℃, we observed the formation of ordered intermetallic PtZn phase. Due to the small size of nanoparticles, only peaks before $2\theta = 60°$ can be clearly observed. As shown in Figure 1i-3, Pt/MWNT@$mSiO_2$ has broad peaks at 39.8 ° and 46.2 °, indicating the formation of small Pt nanoparticles after the reduction of $Pt(OH)_4$/MWNT@$mSiO_2$. The intense diffraction peak around 26 °is assigned to graphitic carbon (002) from MWNT, as confirmed by PXRD pattern of pristine MWNT. Before annealing at 600 ℃, the fresh alloy PtZn/MWNT@$mSiO_2$ (Figure 1i-3) shows that the Pt diffraction peak at 39.8 °slightly shifts towards higher diffraction angle. This shift is due to the decreased lattice constant after incorporation of Zn into Pt to form PtZn alloy. After annealing at 600 ℃, a completely different set of diffraction peaks are formed (31.1 °, 40.8 °, 44.8 °, and 53.4 °) as shown by pattern (4) in Figure 1i. This set of diffraction peaks corresponds well with the standard PXRD pattern of intermetallic PtZn (P4/*mmm*), which has the tetragonal AuCu ($L1_0$ type) structure. However, all diffraction peaks have a slight shift to higher angle compared with the standard pattern of intermetallic PtZn. We are currently investigating the origin of this shift

and we believe this shift can be attributed to the ultrasmall size of the formed PtZn iNPs. The actual Pt:Zn molar ratio measured by inductively coupled plasma mass spectrometry (ICP-MS) is 1.03 ± 0.01, which indicate all added Zn from the precursor is incorporated into the final PtZn iNPs.

Using the Debye−Scherrer equation, the average size for PtZn iNPs in PtZn/MWNT@mSiO_2 was calculated as 3.2 nm, which is in good agreement with TEM measurements (Figure 1e-f and Figure S2b). To prove that mSiO_2 shell can effectively constrain the size and prevent the aggregation of metal nanoparticles, MWNT-supported Pt nanoparticles were prepared using the same precipitation method in the absence of mSiO_2 shell. After the same reduction treatment, Pt nanoparticles with average size of 3.7 ± 0.9 nm was observed from TEM images (Figure S4c and Table S1), which is almost double in size compared to Pt nanoparticles in Pt/MWNT@mSiO_2. Particle sizes of 27 ± 20 nm were observed for PtZn/MWNT (Figure S4d), prepared by wetness impregnation method without the mSiO_2 shell, which is nearly thirteen times larger than those prepared with the confinement of mSiO_2. Moreover, the particle size distribution also increased significantly without the confinement of the mSiO_2 shell. Even though PXRD (Figure S5) also shows the formation of PtZn phases in the absence of mSiO_2, it is clearly seen that both Pt and PtZn nanoparticles have larger sizes and broader size distributions compared to those prepared with the protection of the mSiO_2 shell. We thus suggest that the mSiO_2 shell can successfully restrict the growth of PtZn nanoparticles and significantly prevent them from aggregation under high-temperature annealing, required for the transition from the PtZn alloy to the intermetallic phase. Besides, the strong capping agents (i.e., oleylamine and oleic acid) could be removed during the 600 ℃ annealing. A detailed FTIR study (Figure S6) was conducted to

confirm the organic capping agent-free nature of PtZn iNPs. This approach could be used to prepare electrocatalysts of different compositions with clean surfaces.

The homogenous PtZn intermetallic structure is further confirmed by high-angle-annular-dark-field (HAADF) scanning transmission electron microscopy (STEM) imaging and energy-dispersive X-ray spectroscopy (EDS) elemental mapping using an aberration-corrected electron microscope. In Figure 2a, all PtZn iNPs in focus showed clear lattice fringes, indicating good crystallinity. A PtZn iNP is viewed along [010] zone axis in Figure 2b. The ordered intermetallic structure at the center of the NP is showed by alternating bright (Pt column) and darker (Zn column) contrast on {001} planes, due to greater electron scattering to large detector collection angles by heavier atoms. The two atomic plane distances were measured as 0.354 nm and 0.203 nm, which is in good agreement with the lattice spacing of intermetallic PtZn (P4/*mmm*) along [001] and [200] directions. EDS elemental mapping of as-formed PtZn iNPs was also obtained (Figure 2 c-f), which shows that the Pt map (Figure 2e) has a slightly larger area than the Zn map (Figure 2f), indicating a Pt-rich layer on the surface of the iNP (Figure 2d). EDS mapping of a larger area with c.a. 30 particles is given as Figure S7. Both Pt and Zn are homogeneously dispersed in these particles, which further confirms the uniform compositions from particle to particle.

The electro-catalytic properties of PtZn/MWNT were studied by the methanol oxidation reaction (MOR) under both acidic and basic conditions. To enhance the conductivity, the $mSiO_2$ shell was etched from Pt/MWNT@$mSiO_2$ and PtZn/MWNT@$mSiO_2$ using 1 M NaOH at room temperature before electrochemical tests (the last step in Figure 1a). These etched samples were labeled as Pt/MWNT-E and PtZn/MWNT-E. No obvious size increase was observed in PtZn/MWNT-E as evidenced by TEM images (Figure 1f, S4b, Table S1). ICP-MS confirmed that there's no metal loss during silica etching and the bulk Pt to Zn ratio was maintained as 1.03:1.

The measured surface ratio of Pt to Zn on PtZn/MWNT-E is 1.1 by X-ray photoelectron spectroscopy (XPS) as shown in Figure S8 and Table S2. The slightly Pt-rich surface in XPS agrees with the elemental mapping in Figure 2d-f.

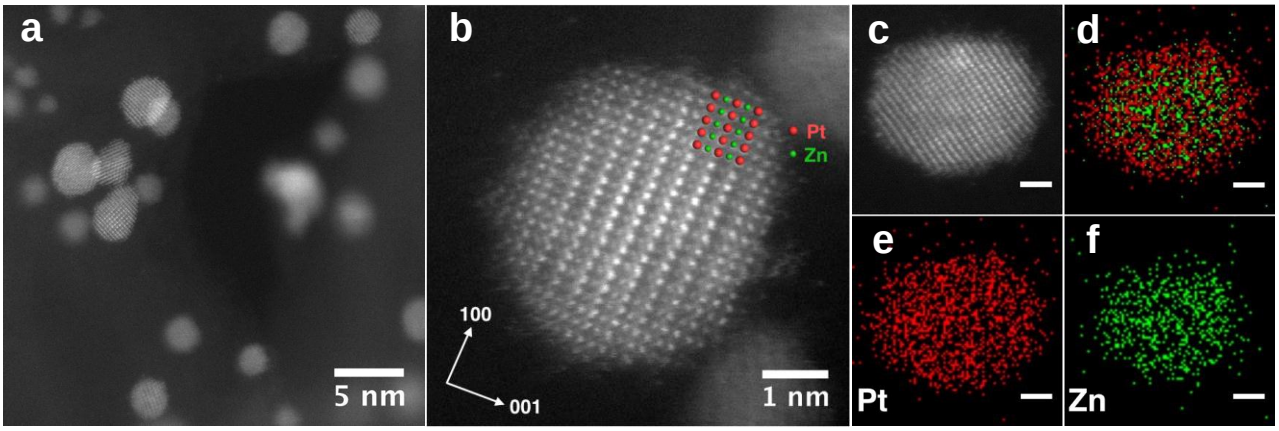

Figure 2. (a, b) High-resolution HAADF STEM images of PtZn iNPs. The red and green spheres in Figure 2b represent Pt and Zn atoms. (c) HAADF-STEM image of a single PtZn iNP. (d-f) Elemental mappings of Pt versus Zn (d), Pt (e), Zn (f). Scale bar, 1 nm.

The typical methanol oxidation polarization curves in acidic condition for PtZn/MWNT-E, Pt/MWNT-E, and commercial Pt/Vulcan catalysts are shown in Figure 3. According to the reported mechanism,[16] methanol is first oxidized to CO_2, CO and/or other carbonaceous intermediates during the forward sweep, contributing to the current density peak at around 0.65 V relative to the Ag/AgCl reference electrode. The adsorbed carbonaceous intermediates are further oxidized to CO_2 during the backward sweep, corresponding to the current density peak at around 0.4 V. To better investigate the electrochemical behaviors of PtZn/MWNT-E, we also evaluated the control sample, PtZn/MWNT, with larger PtZn iNPs, synthesized by co-reduction of Pt and Zn precursor on naked MWNT without the $mSiO_2$ shell (the green curve in Figure 3). PtZn/MWNT-E showed the highest activity due to its lower onset potential and higher current density among all

tested samples. The ratio of forward current density (J_f) to backward current density (J_b) can evaluate the tolerance of catalysts towards poisoning by carbonaceous species.[16] As shown in Figure 3a, the ratio of J_f/J_b for PtZn/MWNT-E (1.46) is much higher than PtZn/MWNT control sample (1.01), Pt/MWNT (0.83) and Pt/Vulcan (0.81) . It clearly shows that the PtZn iNP greatly enhances the tolerance of the catalyst against poisoning.

Figure 3b gives the chronoamperometry (CA) curves for MOR in acidic solution by holding the potential at 0.65 V vs. Ag/AgCl, which is the potential of the forward oxidation peak. The current density of PtZn/MWNT decays rapidly and becomes the smallest after 100 s. The rapid decay in activity for PtZn iNPs synthesized on MWNT without the confinement of $mSiO_2$ is because of their larger particle size. As proven previously by leaching tests performed on $PtNi_3$ nanoparticles, larger particles are more sensitive towards leaching in acidic conditions, leading to lower stability over time.[31] PtZn/MWNT-E shows the highest specific and mass activities, followed by Pt/MWNT-E, Pt/Vulcan, and PtZn/MWNT, which directly shows the incorporation of Zn can enhance the MOR activity. Additionally, the smaller size of particles can also facilitate the effective utilization of Pt and further promote the activity as proven by the fact that PtZn/MWNT-E has 10 times higher mass activity than PtZn/MWNT (Figure 3c).

Activities of different catalysts towards methanol oxidation were also evaluated in a basic solution containing 0.1 M KOH and 0.5 M methanol, as shown in Figure 3d-f. PtZn/MWNT-E still shows the highest current density in both CV and CA curves. CA curves were measured by holding the potential at – 0.1 V and the current densities of different catalysts follow a similar trend as that in the CV curves over time. PtZn/MWNT is found to be not stable in basic solution as shown in Figure 3e. The specific activity of PtZn/MWNT is two times worse than PtZn/MWNT-

E (Figure 3f), which indicates that the smaller size of PtZn iNPs can also enhance the MOR activity in basic condition.

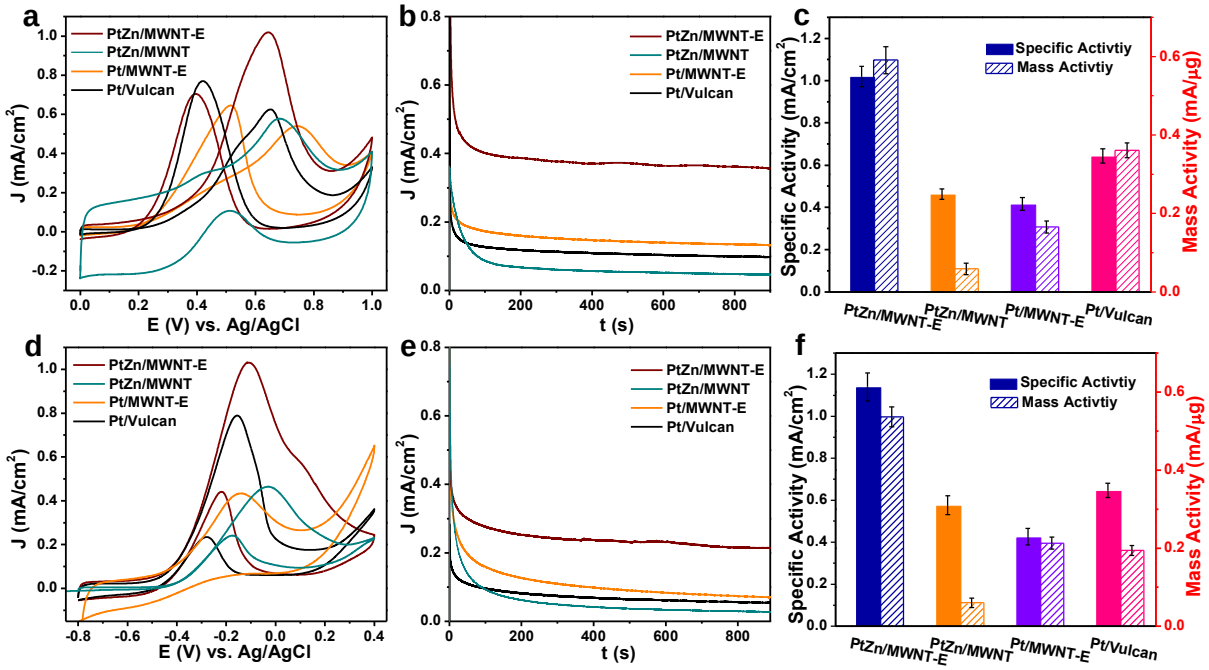

Figure 3. Cyclic voltammetry (a) and chronoamperometry (b) of PtZn/MWNT-E, Pt/MWNT-E, PtZn/MWNT (synthesized in the absence of $mSiO_2$) and commercial Pt/Vulcan catalysts measured at room temperature in argon-purged 0.5 M H_2SO_4 and 1 M methanol. (c) Specific activity and mass activity at 0.65 V vs. Ag/AgCl reference electrode, Cyclic voltammetry (d) and chronoamperometry (e) of PtZn/MWNT-E, Pt/MWNT-E, PtZn/MWNT (synthesized in absence of $mSiO_2$) and commercial Pt/Vulcan catalysts measured at room temperature in argon-purged 0.1 M KOH and 0.5 M methanol. (f) Specific activity and mass activity at -0.1 V vs. Ag/AgCl electrode, all the measurements were repeated 3 times and currents were normalized to the electrochemical surface area (ECSA).

To have a better insight into the structure and activity relationship, another two control samples (2.8 nm PtZn alloy/MWNT and 8.6 nm PtZn intermetallic/MWNT) were prepared (Figure

S10 and S11). Their electrocatalytic performance was compared with other catalysts and summarized in Table S3 and S4. PtZn iNPs has 2.3 and 1.7 times higher specific activities in the respective acidic and basic conditions, compared to that of PtZn alloy NPs with a comparable size (Figure S12). Moreover, the specific activity increases with the decrease of the particle size. We also compared the activity of PtZn/MWNT-E with the results from previously published literature (summarized in Table S5), among which PtZn/MWNT-E has the highest mass activity, comparable specific activity, and J_f/J_b values. Therefore, the smaller PtZn iNPs is highly favorable for MOR.

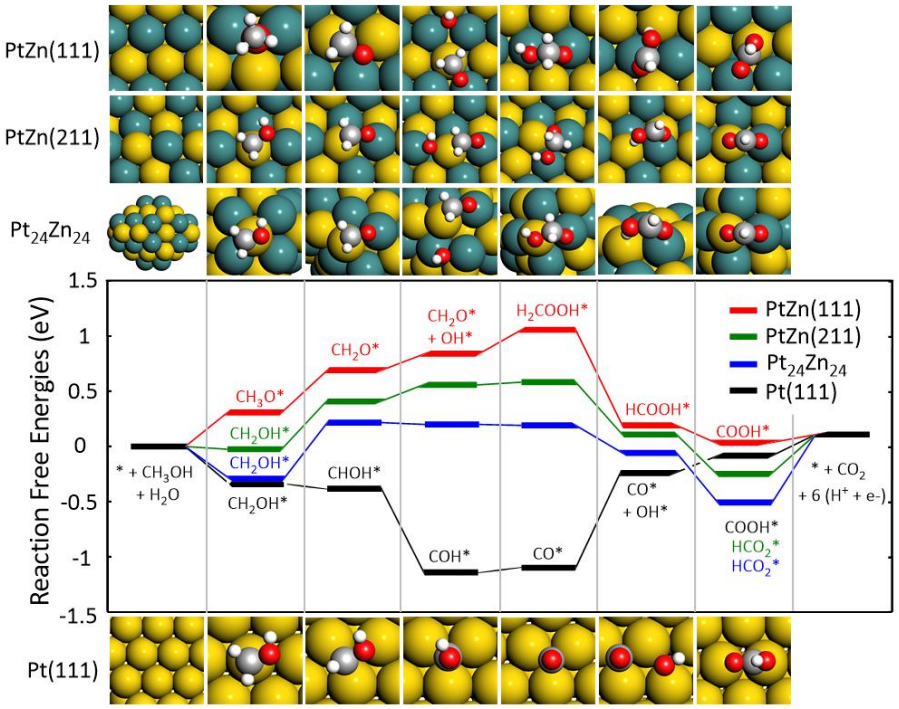

Figure 4. Calculated reaction mechanisms of MOR on PtZn (111), stepped PtZn (211), $Pt_{24}Zn_{24}$ cluster and Pt (111). For the reactions on PtZn (111), PtZn (211) and $Pt_{24}Zn_{24}$, all the elementary reaction steps, except for $CH_2O^* + OH^* \rightarrow H_2COOH^*$, involve the dissociation of a $(H^+ + e^-)$ pair. For the reaction on Pt (111), all the steps, except for $CO^* + OH^* \rightarrow COOH^*$, involve the dissociation of a $(H^+ + e^-)$ pair.

Density functional theory (DFT) calculations were carried out to investigate the reaction mechanisms of MOR on PtZn and Pt materials and the effect of particle size and metal composition. The reaction free energies of each electrochemical step were calculated using the computational hydrogen electrode (CHE) model,[32-34] which is independent of the pH value of the electrolyte (for the computational details, please refer to the supporting information). Although it is challenging to calculate the MOR on nanoparticles with different sizes, it is reasonable to investigate the particle size effect by considering different reaction sites (terrace, edge, and corner), because smaller nanoparticles generally have higher ratios of edge and corner sites than larger nanoparticles.[35] Therefore, in this study PtZn (111), stepped PtZn (211) and a $Pt_{24}Zn_{24}$ cluster were calculated to represent terrace, edge, and corner sites, respectively. As shown in Figure 4, all three PtZn systems undergo a non-CO reaction pathway, in which a key intermediate CH_2O* is formed from either CH_3O* or CH_2OH*, followed by its interaction with a surface hydroxyl (OH*) to form H_2COOH*. The H_2COOH* then releases a ($H^+ + e^-$) pair to form HCOOH*. The HCOOH* then goes through either COOH* or HCOO* to form CO_2. It is notable that the reaction pathways of the three PtZn systems follow an energetic trend: $Pt_{24}Zn_{24}$ < PtZn (211) < PtZn (111), suggesting that MOR on corner sites are likely to have smaller apparent barriers than that on edge and terrace sites. This is likely due to the enhanced binding strengths between the intermediate adsorbates and the under-coordinated metal atoms on the corner sites. This indicates that smaller PtZn iNPs are energetically more favorable for MOR than larger iNPs.

These computational results support the experimental observations that size-confined PtZn iNPs (PtZn/MWNT-E) are more active in both acidic and basic solutions than larger iNPs (PtZn/MWNT). Furthermore, the PtZn systems were compared with the Pt (111) surface to study the effect of metal composition (Figure 4). Differing from the PtZn systems, MOR on Pt (111)

undergoes a CO pathway, in which CHOH* is formed after CH_2OH*, followed by the formation of COH* and CO*. The CO* is then converted to COOH*, which is oxidized to form CO_2. This reaction pathway agrees well with a previous DFT study.[36]Although the reaction pathway of Pt (111) showed no apparent barrier, the highly stable COH* and CO* engender a "thermodynamic sink", and thus the conversion from CO* to CO_2 becomes energetically hindered (Figure 4). This could lead to the catalyst deactivation by CO poisoning. In addition, another key adsorbate, OH*, is found to have higher binding strength with Zn atoms compared to Pt atoms (Figure 4). The stabilization of OH* by Zn atoms leads to the ($CH_2O^* \rightarrow CH_2O^* + OH^* \rightarrow H_2COOH^*$) pathway for the PtZn systems instead of the ($CH_2O^* \rightarrow CHO^* \rightarrow CO^*$) pathway.

The different reaction paths between PtZn systems and pure Pt explained the experimentally observed higher tolerance of PtZn systems toward poisoning compared to commercial Pt catalyst and revealed the critical role of Zn atoms. With no remarkable barriers or thermodynamic sinks, the calculated $Pt_{24}Zn_{24}$ pathway reflects the better catalytic activity of PtZn/MWNT-E than larger PtZn iNPs and commercial Pt catalyst.

To support the non-CO pathway on PtZn surface, we conducted more experiments to study the origin of the backward oxidation peak of MOR by a previously reported method.[37] As shown in Figure S14a and c, CV scan (cycle 1) was first measured in an acidic solution without methanol. Methanol was added at the beginning of the second cathodic (backward) scan, at which point MOR intermediates have not been formed. Therefore, the backward peak observed during the second cathodic scan is purely induced by the freshly added methanol. We then compared the peak area of backward peak in the second and third cycles. The extra peak area (charge) in the third cathodic scan than the second one could be caused by intermediates generated in the third anodic (forward) scan. The fractions of contribution from intermediates were calculated as 34.8% for PtZn iNPs and

67.8% for Pt NPs, which indicates that fewer intermediates were generated on PtZn than on Pt (Figure S14a and c). In another experiment, we purged CO at the beginning of the second cathodic scan. As shown in Figure S14d, CO was immediately oxidized on the surface of Pt as indicated by the sudden current jump, while no CO oxidization was observed on PtZn iNPs (Figure S14b). These experimental results suggest that CO has a weaker interaction with PtZn than with Pt.

Leaching of Zn was only observed after 1000 cycles in the acidic electrolyte, while basic condition does not cause any obvious leaching of Zn even after 1000 cycles (Table S6). The specific activity of PtZn/MWNT-E and Pt/Vulcan catalysts before and after 1000 cycles were compared (Figure S15). Surprisingly, only 3% loss in specific activity was observed on PtZn/MWNT-E, while commercial Pt/Vulcan has a 50 % lost. It is highly possible that the PtZn iNPs transform to particles with thin Pt shells on PtZn intermetallic cores under the acidic condition. However, the PtZn intermetallic core could still alter the electronic structure of the Pt shell and lead to the enhanced MOR performance, as proposed by Abruña group.[17]

2.5 Conclusion

In summary, we have successfully synthesized sub-4 nm PtZn iNPs using a general and well-controlled manner benefiting from the MWNT@$mSiO_2$ platform. The $mSiO_2$ shell provides a confined environment for the growth of metal nanoparticles and prevents them from aggregating during high-temperature annealing, a step required for the formation of PtZn intermetallic phase. The smaller PtZn iNPs synthesized by the $mSiO_2$ shell confinement show better stability in both acidic and basic electrolytes and higher activity than commercial Pt catalyst and the larger PtZn iNPs directly synthesized without the protection of the $mSiO_2$ shell. DFT calculations are in good agreement with the experimental results. The calculations reveal that PtZn systems undergo a "non-CO" pathway for MOR, due to the stabilization of OH* by Zn atoms. However, pure Pt

system forms highly stable COH* and CO* intermediates, which could cause catalyst deactivation. Furthermore, the calculations demonstrate that the reaction pathways of smaller-size PtZn particles are energetically more favorable than those of larger particles, due to the enhanced adsorption energies by the under-coordinated corner atoms. This general synthesis strategy using the MWNT@mSiO_2 platform opens up fascinating opportunities for the synthesis of intermetallic nanomaterials with well-controlled particle sizes and improved monodispersity, which could lead to highly active heterogeneous catalysts with enhanced specific activity and stability in fuel cell applications.

2.6 Acknowledgment

This work was partially supported by National Science Foundation (NSF) grant CHE-1607305. We are also grateful for the support by the startup funds from Ames Laboratory (Royalty Account) and Iowa State University. The work at Ames Lab was supported in part by the U.S. Department of Energy (DOE), Office of Science, Basic Energy Sciences, Materials Science and Engineering Division under Contract DE-AC02-07CH11358, with additional capabilities made possible from LDRD funding. We thank Professor Gordon J. Miller for the use of the X-ray diffractometer. The U.S. Department of Energy, Office of Science, BES-Division of Materials Science and Engineering (computational study) and BES-Scientific User Facilities under Contract DE-AC02-06CH11357 supported the computational work. We acknowledge the computing resources operated by the Laboratory Computing Resource Center (ANL) and the ANL Center for Nanoscale Materials.

2.7 References

1. DeSario, D. Y.; DiSalvo, F. J. *Chem. Mater.* 2014, *26* (8), 2750-2757.

2. Abe, H.; Matsumoto, F.; Alden, L. R.; Warren, S. C.; Abruna, H. D.; DiSalvo, F. J. *J. Am. Chem. Soc.* 2008, *130* (16), 5452-5458.

3. Cui, Z. M.; Chen, H.; Zhao, M. T.; Marshall, D.; Yu, Y. C.; Abruna, H.; DiSalvo, F. J. *J. Am. Chem. Soc.* 2014, *136* (29), 10206-10209.

4. Kang, Y. J.; Murray, C. B. *J. Am. Chem. Soc.* 2010, *132* (22), 7568-+.

5. Ghosh, T.; Leonard, B. M.; Zhou, Q.; DiSalvo, F. J. *Chem. Mater.* 2010, *22* (7), 2190-2202.

6. Yang, H. Z.; Zhang, J.; Sun, K.; Zou, S. Z.; Fang, J. Y. *Angew Chem Int Edit* 2010, *49* (38), 6848-6851.

7. Liu, L. F.; Pippel, E.; Scholz, R.; Gosele, U. *Nano Lett.* 2009, *9* (12), 4352-4358.

8. Wang, D. L.; Xin, H. L. L.; Hovden, R.; Wang, H. S.; Yu, Y. C.; Muller, D. A.; DiSalvo, F. J.; Abruna, H. D. *Nat. Mater.* 2013, *12* (1), 81-87.

9. Chen, W.; Kim, J. M.; Sun, S. H.; Chen, S. W. *Langmuir* 2007, *23* (22), 11303-11310.

10. Wang, D. Y.; Chou, H. L.; Lin, Y. C.; Lai, F. J.; Chen, C. H.; Lee, J. F.; Hwang, B. J.; Chen, C. C. *J. Am. Chem. Soc.* 2012, *134* (24), 10011-10020.

11. Casado-Rivera, E.; Volpe, D. J.; Alden, L.; Lind, C.; Downie, C.; Vazquez-Alvarez, T.; Angelo, A. C. D.; DiSalvo, F. J.; Abruna, H. D. *J. Am. Chem. Soc.* 2004, *126* (12), 4043-4049.

12. Ji, X. L.; Lee, K. T.; Holden, R.; Zhang, L.; Zhang, J. J.; Botton, G. A.; Couillard, M.; Nazar, L. F. *Nat. Chem.* 2010, *2* (4), 286-293.

13. Matsumoto, F.; Roychowdhury, C.; DiSalvo, F. J.; Abruna, H. D. *J. Electrochem. Soc.* 2008, *155* (2), B148-B154.

14. Stamenkovic, V. R.; Fowler, B.; Mun, B. S.; Wang, G. F.; Ross, P. N.; Lucas, C. A.; Markovic, N. M. *Science* 2007, *315* (5811), 493-497.

15. Miura, A.; Wang, H. S.; Leonard, B. M.; Abruna, H. D.; DiSalvo, F. J. *Chem. Mater.* 2009, *21* (13), 2661-2667.

16. Kang, Y. J.; Pyo, J. B.; Ye, X. C.; Gordon, T. R.; Murray, C. B. *ACS Nano* 2012, *6* (6), 5642-5647.

17. Gregoire, J. M.; Kostylev, M.; Tague, M. E.; Mutolo, P. F.; van Dover, R. B.; DiSalvo, F. J.; Abruna, H. D. *J. Electrochem. Soc.* 2009, *156* (1), B160-B166.

18. Chen, Q. L.; Zhang, J. W.; Jia, Y. Y.; Jiang, Z. Y.; Xie, Z. X.; Zheng, L. S. *Nanoscale* 2014, *6* (12), 7019-7024.

19. Xu, D.; Liu, Z. P.; Yang, H. Z.; Liu, Q. S.; Zhang, J.; Fang, J. Y.; Zou, S. Z.; Sun, K. *Angew. Chem. Int. Edit.* 2009, *48* (23), 4217-4221.

20. Xia, B. Y.; Wu, H. B.; Wang, X.; Lou, X. W. *J. Am. Chem. Soc.* 2012, *134* (34), 13934-13937.

21. Sun, X. H.; Jiang, K. Z.; Zhang, N.; Guo, S. J.; Huang, X. Q. *ACS Nano* 2015, *9* (7), 7634-7640.

22. Saleem, F.; Zhang, Z. C.; Xu, B.; Xu, X. B.; He, P. L.; Wang, X. *J. Am. Chem. Soc.* 2013, *135* (49), 18304-18307.

23. An, K.; Alayoglu, S.; Musselwhite, N.; Plamthottam, S.; Melaet, G.; Lindeman, A. E.; Somorjai, G. A. *J. Am. Chem. Soc.* 2013, *135* (44), 16689-16696.

24. An, K.; Alayoglu, S.; Musselwhite, N.; Na, K.; Somorjai, G. A. *J. Am. Chem. Soc.* 2014, *136* (19), 6830-6833.

25. Li, W.; Yang, J. P.; Wu, Z. X.; Wang, J. X.; Li, B.; Feng, S. S.; Deng, Y. H.; Zhang, F.; Zhao, D. Y. *J. Am. Chem. Soc.* 2012, *134* (29), 11864-11867.

26. Shang, L.; Bian, T.; Zhang, B.; Zhang, D.; Wu, L.-Z.; Tung, C.-H.; Yin, Y.; Zhang, T. *Angew. Chem. Int. Edit.* 2014, *53* (1), 250-254.

27. Xiao, C.; Maligal-Ganesh, R. V.; Li, T.; Qi, Z.; Guo, Z.; Brashler, K. T.; Goes, S.; Li, X.; Goh, T. W.; Winans, R. E.; Huang, W. *ChemSusChem* 2013, *6* (10), 1915-1922.

28. Maligal-Ganesh, R.; Xiao, C.; Goh, T.; Wang, L.; Gustafson, J.; Pei, Y.; Qi, Z.; Jahson, D. D.; Zhang, S.; Tao, F.; Huang, W. *ACS Catal.* 2016, *6* (3), 1754-1764.

29. Pei, Y.; Maligal-Ganesh, R.; Xiao, C.; Goh, T.; Brashler, K.; Gustafson, J.; Huang, W. *Nanoscale* 2015, *7*, 16721-16728.

30. Fang, B.; Chaudhari, N. K.; Kim, M. S.; Kim, J. H.; Yu, J. S. *J. Am. Chem. Soc.* 2009, *131* (42), 15330-15338.

31. Gan, L.; Heggen, M.; O'Malley, R.; Theobald, B.; Strasser, P. *Nano Lett.* 2013, *13* (3), 1131-1138.

32. Peterson, A. A.; Abild-Pedersen, F.; Studt, F.; Rossmeisl, J.; Norskov, J. K. *Energ. Environ. Sci.* 2010, *3* (9), 1311-1315.

33. Norskov, J. K.; Rossmeisl, J.; Logadottir, A.; Lindqvist, L.; Kitchin, J. R.; Bligaard, T.; Jonsson, H. *J. Phys. Chem. B* 2004, *108* (46), 17886-17892.

34. Peterson, A. A.; Norskov, J. K. *J. Phys. Chem. Lett.* 2012, *3* (2), 251-258.

35. Gao, D. F.; Zhou, H.; Wang, J.; Miao, S.; Yang, F.; Wang, G. X.; Wang, J. G.; Bao, X. H. *J. Am. Chem. Soc.* 2015, *137* (13), 4288-4291.

36. Ferrin, P.; Mavrikakis, M. *J. Am. Chem. Soc.* 2009, *131* (40), 14381-14389.

2.8 Supporting Information

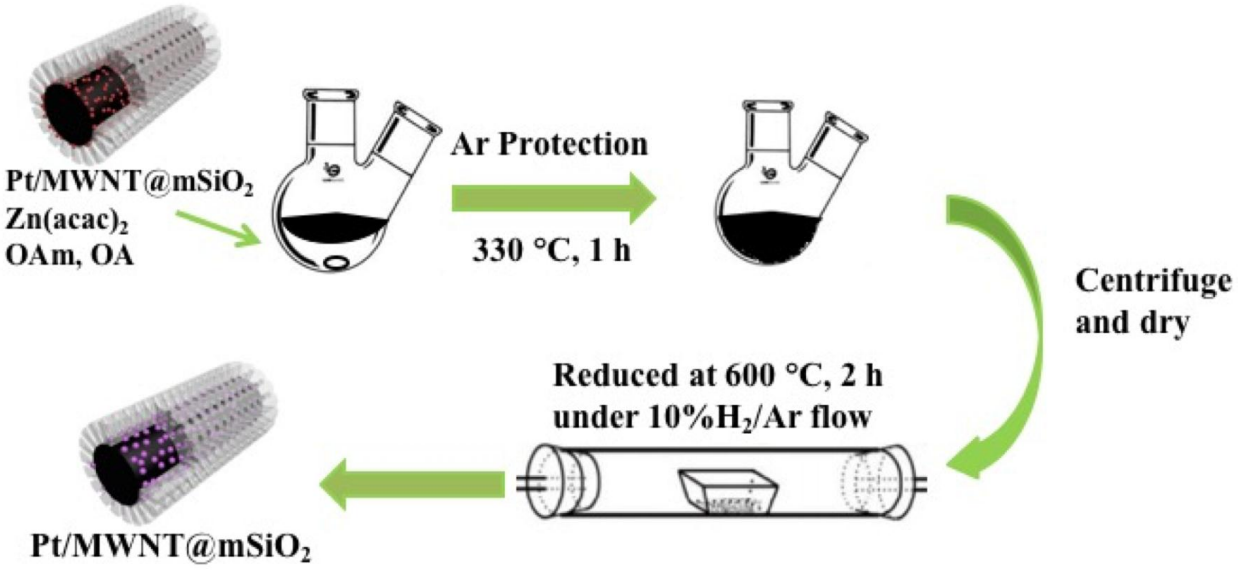

Figure S1. Schematic representation of the synthesis route for PtZn/MWNT@mSiO2.

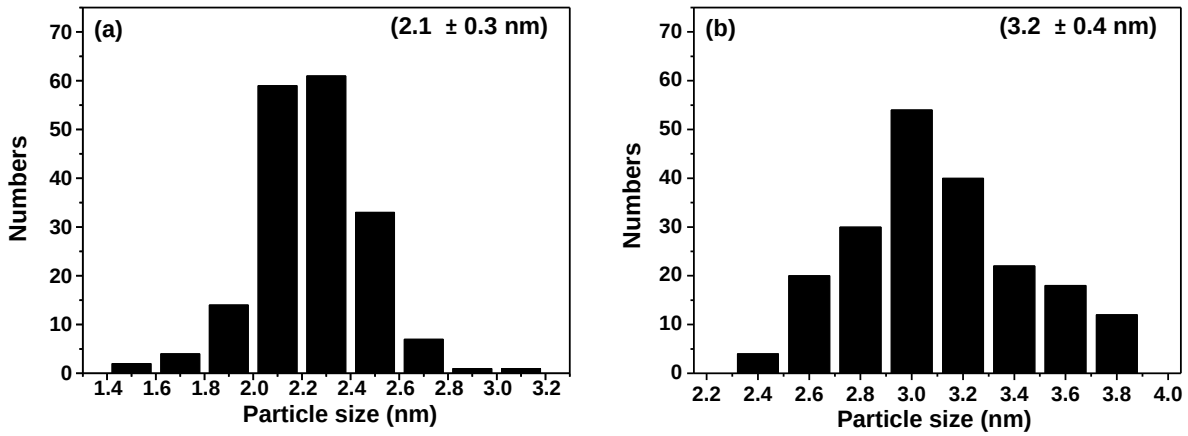

Figure S2. Size distribution of (a) Pt/MWNT@mSiO$_2$ and (b) PtZn/MWNT@mSiO$_2$. 200 particles were counted for each sample.

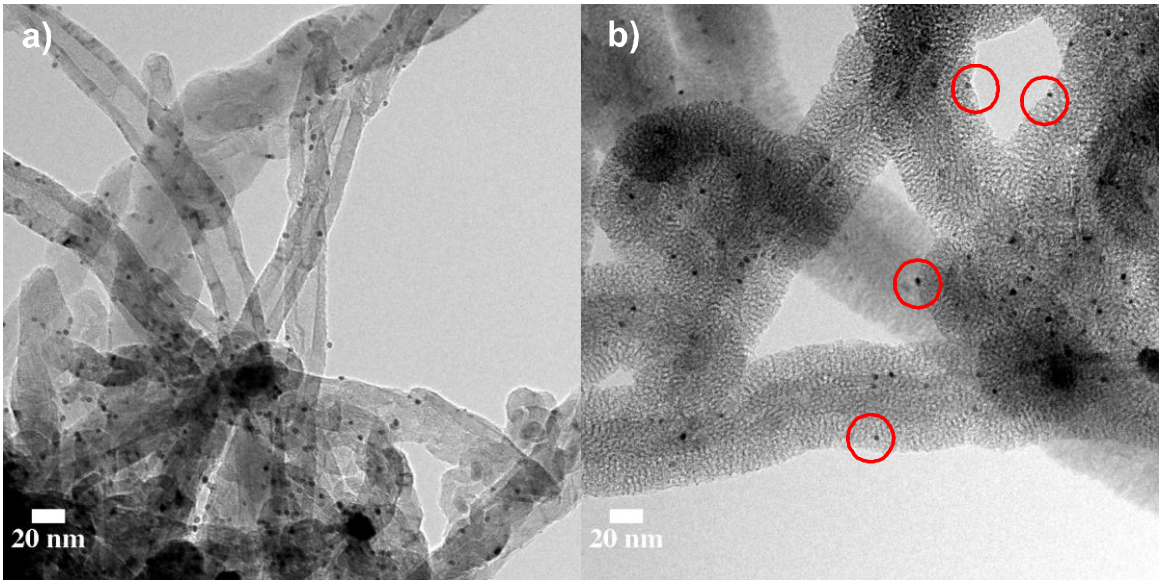

Figure S3. TEM images of (a) PVP–capped Pt/MWNT and (b) PVP-capped Pt/MWNT@mSiO$_2$. During the growth of the mSiO$_2$ shell, some Pt NPs were detached from MWNT and moved to the external surface of the mSiO$_2$ shell or encapsulated in the mesoporous channel (as indicated by the red circles in Figure S3b), which could be due to the weaker interaction between PVP-capped Pt NPs and MWNT. Besides, the Pt loading is much lower than Pt/MWNT@mSiO$_2$ prepared by the *in situ* reduction of Pt precursor.

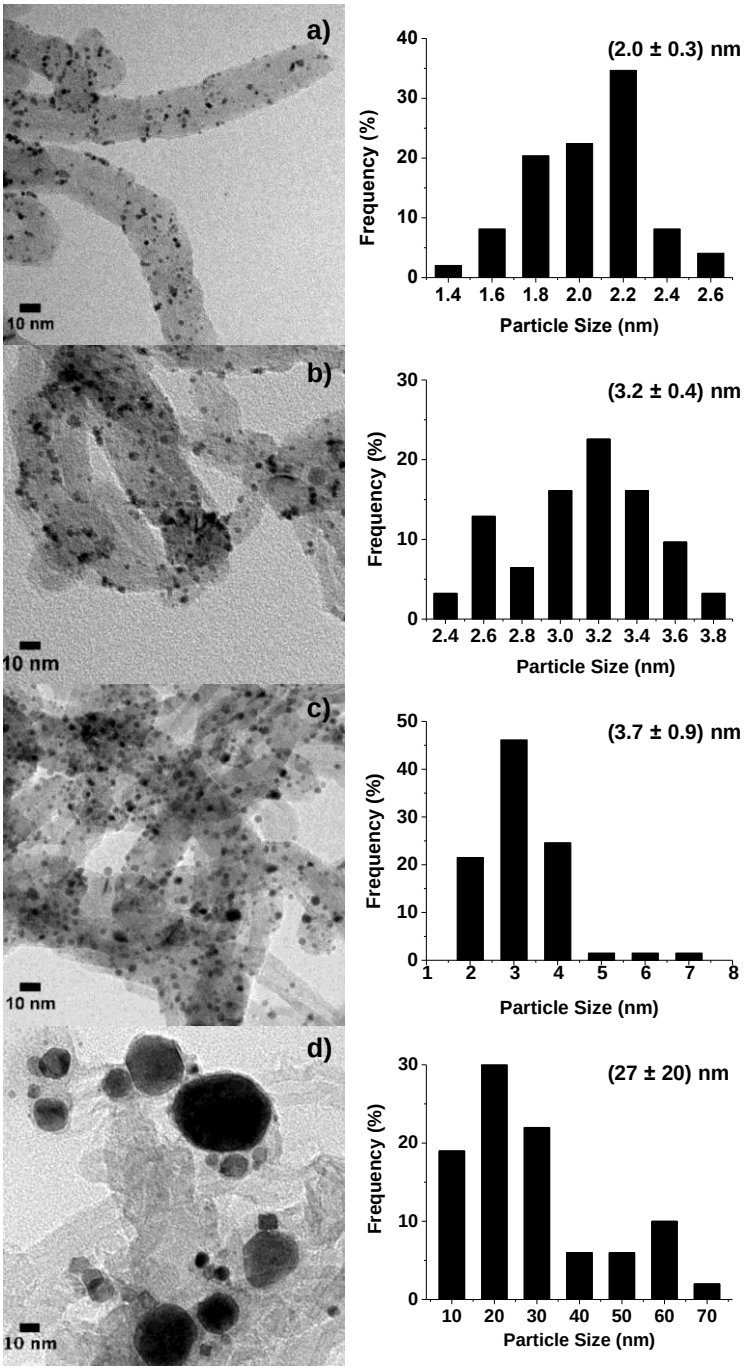

Figure S4. TEM images of (a) Pt/MWNT@mSiO$_2$ after etching away silica by 1 M NaOH; (b) PtZn/MWNT@mSiO$_2$ after etching away silica by 1 M NaOH; (c) Pt/MWNT synthesized without silica shell; and (d) PtZn/MWNT synthesized without silica shell. 200 particles were counted for each sample, and the size distribution plots are shown right beside the corresponding TEM images.

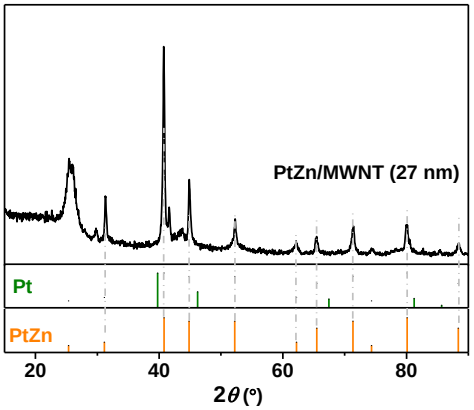

Figure S5. PXRD patterns of MWNT-supported PtZn NPs synthesized by wetness impregnation without the $mSiO_2$ coating.

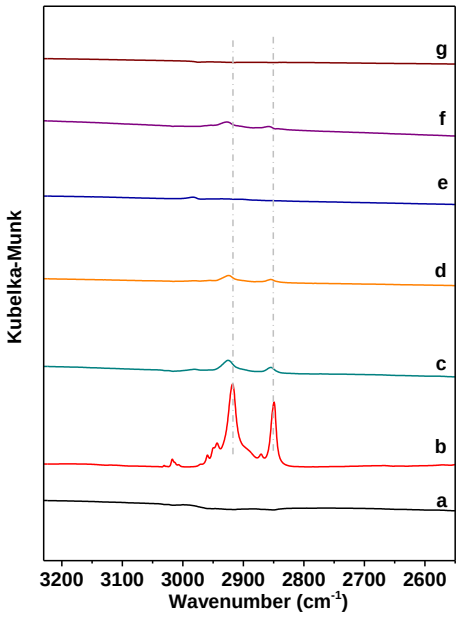

Figure S6. FTIR spectra of (a) pristine MWNT, (b) CTAB, (c) unreduced $Pt(OH)_4$/MWNT@SiO_2, (d) Pt/MWNT@SiO_2 reduced at 240 ˚C, (e) Pt/MWNT@$mSiO_2$ after refluxing (prepared by refluxing sample (d) in NH_4NO_3 ethanol solution to remove surfactant), (f) PtZn alloy/MWNT@$mSiO_2$ synthesized by solvothermal method at 330 ˚C, (g) PtZn/MWNT@$mSiO_2$ synthesized by annealing sample (f) at 600 ˚C. Spectra (c-g) were normalized by the peak intensity of Si-O-Si stretching (1060 cm^{-1}) to show the ratio between capping and silica.

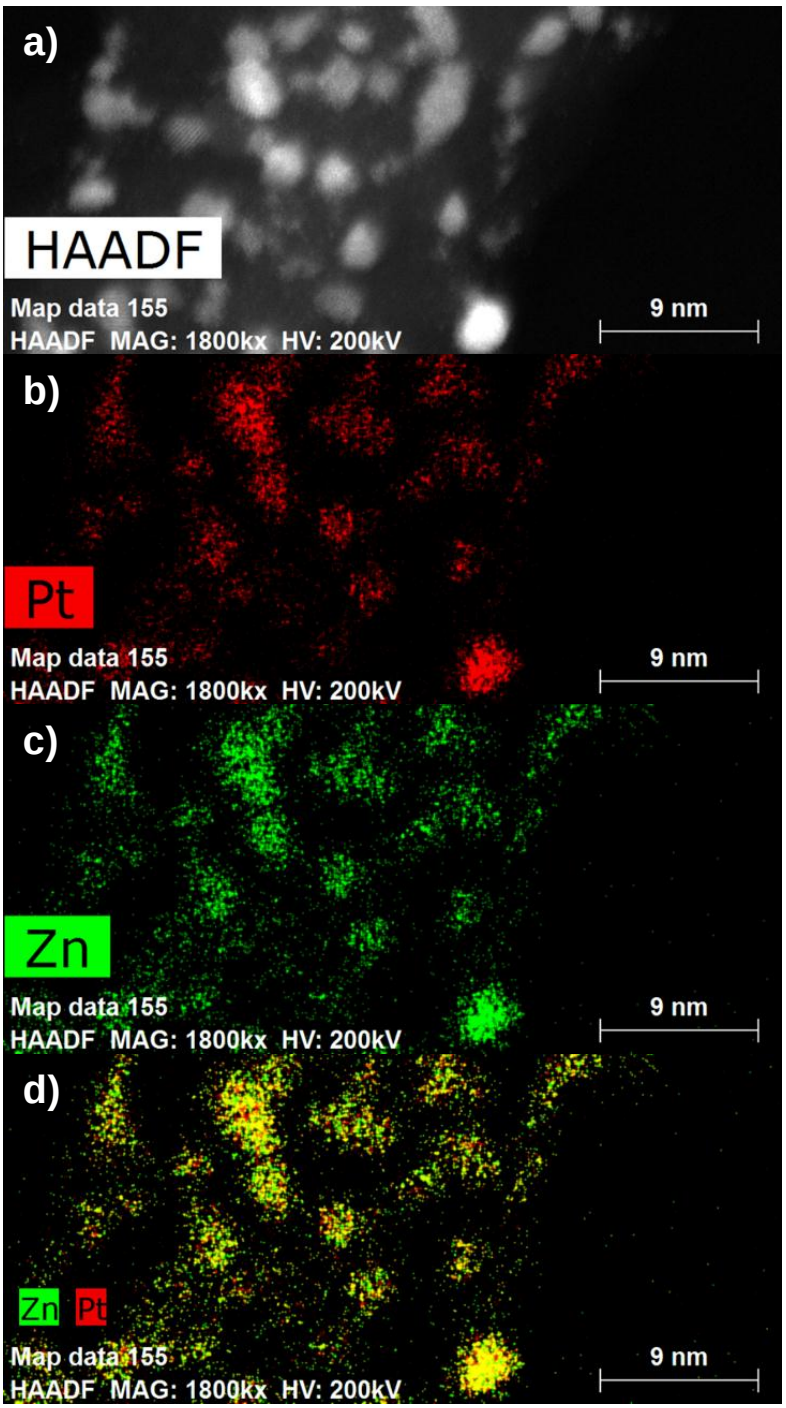

Figure S7. HAADF-STEM image of (a) PtZn/MWNT-E and EDX mappings of (b) Pt, (c) Zn, and (d) overlaid images of Pt and Zn signals.

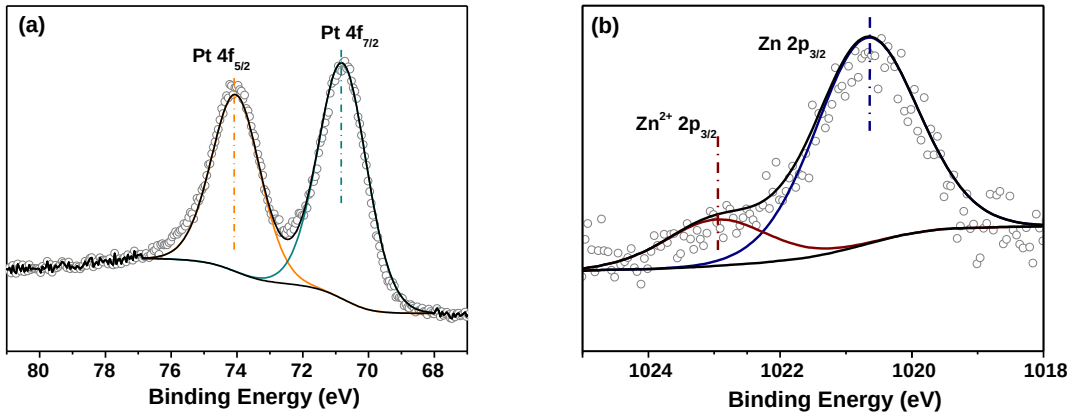

Figure S8. XPS spectra for (a) Pt 4f and (b) Zn 2p of PtZn/MWNT-E sample after etching away silica shell. All binding energies were calibrated by C1s (284.0 eV) as the reference.

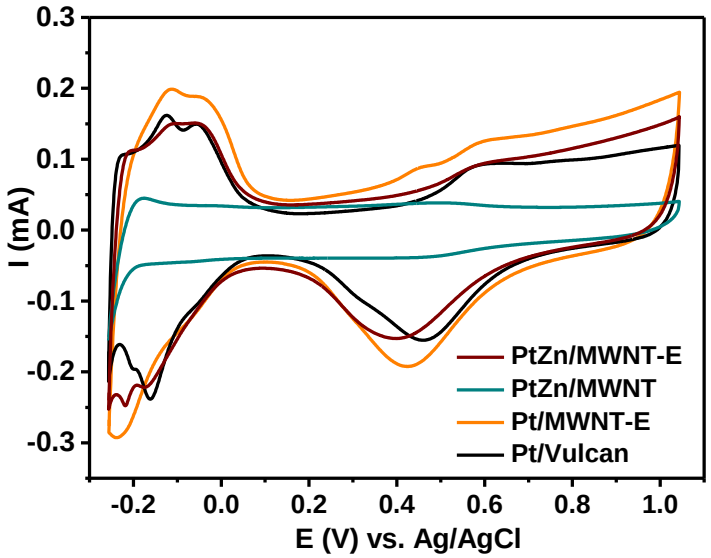

Figure S9. CV scans of PtZn/MWNT-E, PtZn/MWNT, Pt/MWNT, and Pt/Vulcan in 0.1 M $HClO_4$ solution. Argon was purged for 30 min before any test. Electrochemical active surface area (ECSA) was calculated by integrating the desorption peak of H_2 (0.05-0.4 V vs. RHE). The potential was converted to Ag/AgCl reference by using equation: E (vs. Ag/AgCl) = E (vs. RHE) - 0.059 × pH - 0.197. We also measured ECSA of Pt/Vulcan and PtZn/MWNT-E in 0.05 M H_2SO_4 solution, and the values are within 5% difference from those measured in $HClO_4$ solution.

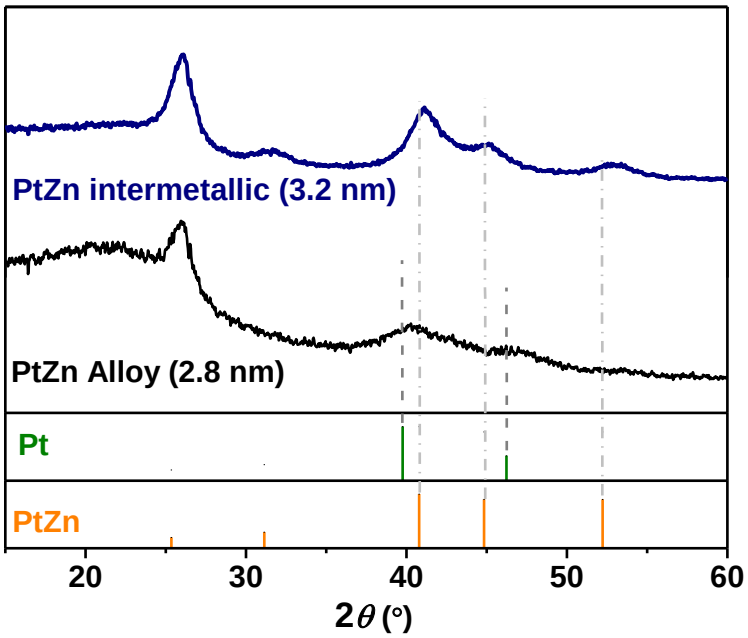

Figure S10. XRD patterns of PtZn/MWNT@mSiO$_2$(intermetallic, same as Figure 1i-4) and PtZn-alloy/MWNT@mSiO$_2$ control sample. The particle size of PtZn alloy NPs was calculated as 2.8 nm by using Debye-Scherrer equation.

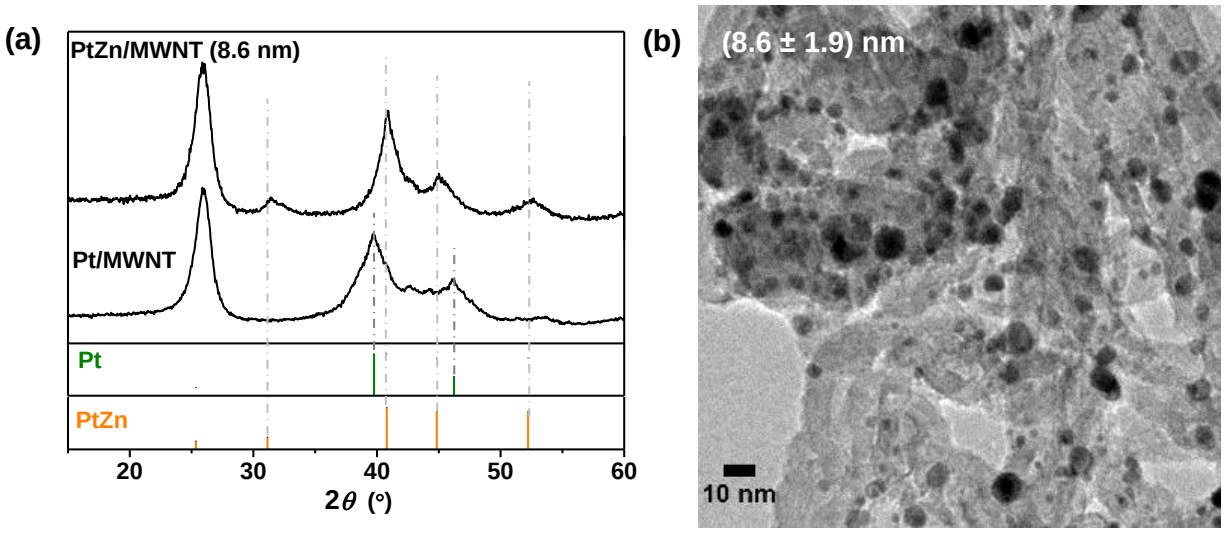

Figure S11. (a) XRD patterns and (b) a representative TEM image of 8.6 nm intermetallic PtZn/MWNT control catalyst, which was synthesized by using 3.7 nm Pt/MWNT without the protection of the mSiO$_2$ shell.

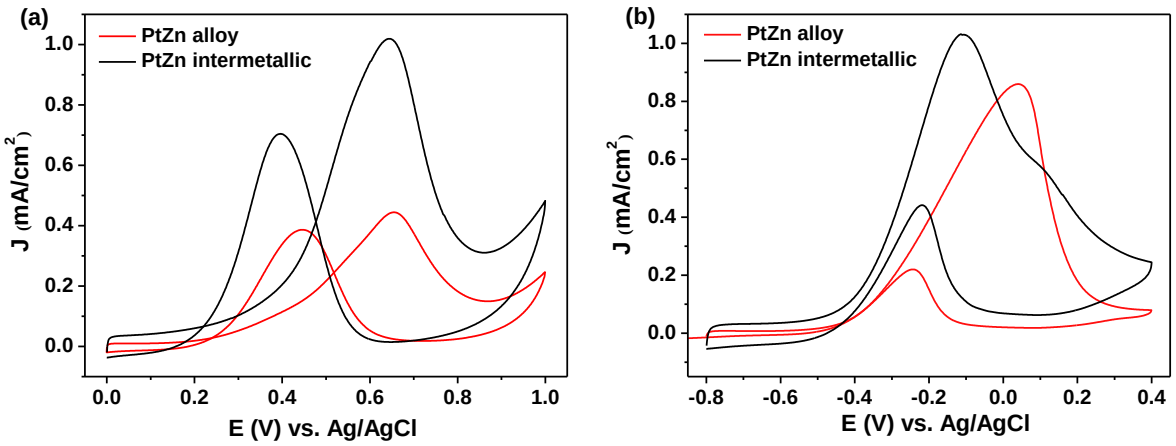

Figure S12. Methanol oxidation on PtZn-alloy/MWNT-E and PtZn/MWNT-E catalysts in (a) acidic and (b) basic conditions. Intermetallic PtZn iNPs show better specific activities in both acidic and basic electrolytes.

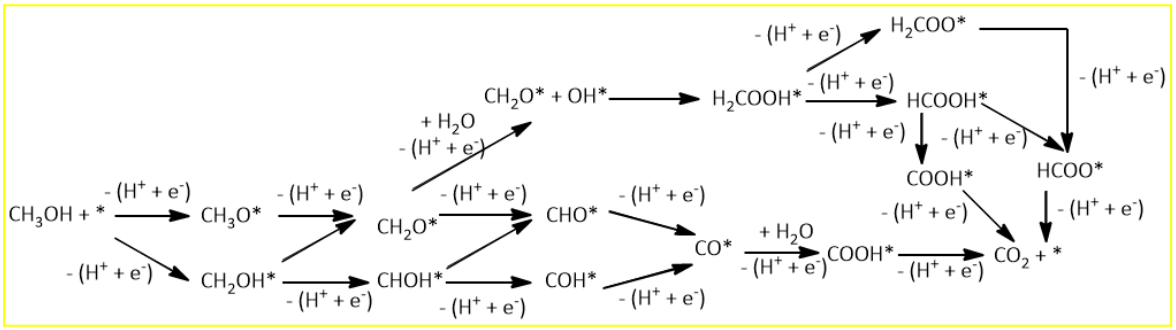

Figure S13. Reaction network of catalytic methanol oxidation reaction.

Each electrochemical reaction step considered in the present work involves a (H^+ + e^-) pair transfer from the adsorbed species on the metal surface/cluster to the solution. The free energy change of each (H^+ + e^-) pair transfer reaction was calculated using the computational hydrogen electrode (CHE) method suggested by Norskov et al.[6-8] The reaction free energy of each elementary reaction can be calculated using Eqn. 1:

$$\Delta \mathbf{G_{ele}} = = \boldsymbol{\mu}[\mathbf{Product}] - \boldsymbol{\mu}[\mathbf{Reactant}] - 0.\mathbf{5}\boldsymbol{\mu}[\mathbf{H_{2(g)}}] + \boldsymbol{eU} \quad (1)$$

where ΔG_{ele} represents the free energy change of the elementary step, μ is chemical potential, and U is applied electrical potential. When $U = 0V$, ΔG_{ele} is the limiting potential (U_L) of elementary hydrogenation reaction. The CHE method circumvents the explicit quantum mechanical calculations for solvated protons and all the solvent effect on geometries, and free energies were neglected. All the Gibbs free energies were calculated in gas phase at 25°C, in which all the gaseous molecules (CO_2 and H_2) and all the metal cluster-containing systems were calculated under the standard pressure, 101325Pa, while the liquid phase molecules (H_2O and CH_3OH) were calculated under their corresponding vapor fugacity, which comes from their vapor-liquid equilibrium with water corresponding to a liquid mole fraction of 0.01 (details are in Experimental Section, Supporting Information).[6] Free energies of intermediate adsorbates were calculated by treating 3N degrees of freedom of the adsorbate as vibrational. It is assumed that changes in the vibrations of the metal surface were minimal.[6] Vibrational modes were calculated using a normal-mode analysis. Zero-point energies, entropies, and heat capacities were calculated from these vibrations to convert the electronic energies into free energies at 25°C. The solvation effect at the water-solid interface was taken into account by adding an energy correction to the calculated total energy of certain adsorbates.[6] For instance, OH* was found to be stabilized in liquid water by approximately 0.5 eV,[5, 9] and hydroxyl group that is indirectly bound to the surface/cluster through other atoms, *ROH and *ROOH, was found to be stabilized by 0.25 eV.[10] Also, CO* was stabilized by 0.1 eV, which was applied to both CO* and CHO*.[6] The calculated total energies of CO_2, H_2, and H_2O by PBE functional were corrected based on the previous studies.[6]

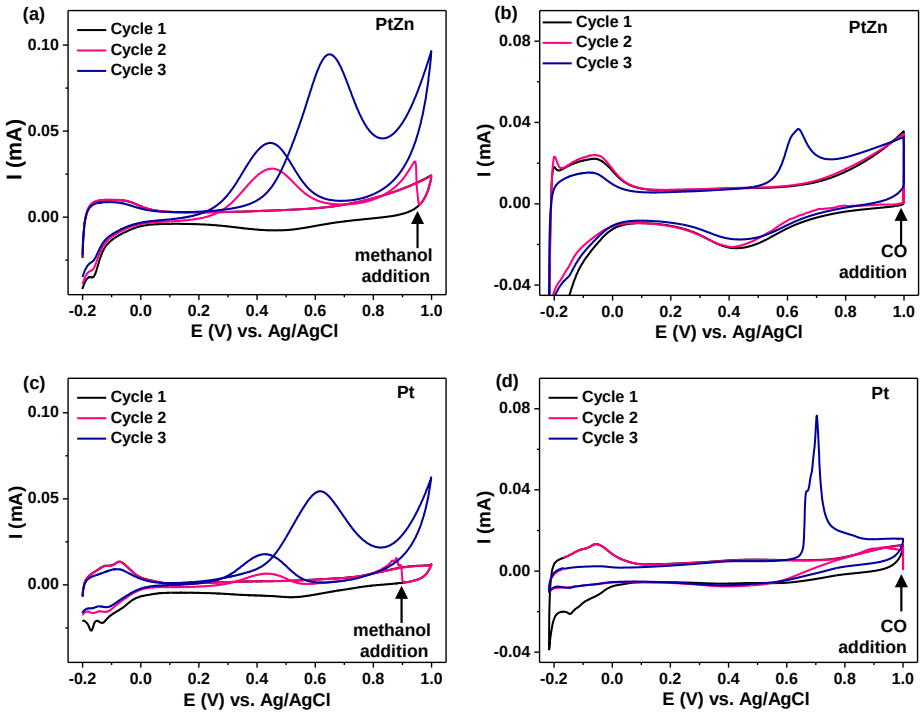

Figure S14. Study of backward oxidation peak in the MOR cathodic scan catalyzed by (a, b) PtZn/MWNT-E and (c, d) Pt/Vulcan. In a and c, the first cycle was conducted in 25 mL of argon-purged 0.5 M H_2SO_4 solution. 25 mL of 0.5 M H_2SO_4 + 2 M methanol was added at the indicated potential by the black arrows during the second backward scan. In b and d, the first cycle was conducted in 25 mL of argon-purged 0.5 M H_2SO_4 solution while potential was held at 1.00 V for 3 min before the backward scan. During the second scan, CO was purged into the system for 3 min when the potential was held at 1.00 V as indicated by the black arrows. Glass carbon electrode (3 mm in diameter) was used as the working electrode and applied catalyst ink was adapted based the electrode geometric area. All the scan speed was controlled as 10 mV/s.

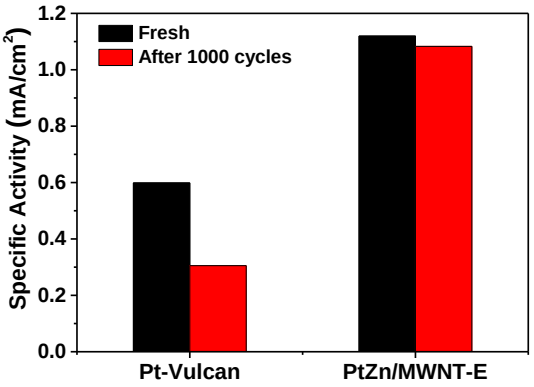

Figure S15. The specific activity at 0.65 V of Pt/Vulcan and PtZn/MWNT-E were compared before and after durability tests. Both catalysts were cycled in argon-purged 0.1 M $HClO_4$ solution for 1000 times at a scan speed of 100 mV/s. PtZn/MWNT-E has ca. 3% loss in specific activity while Pt/Vulcan lost 50% activity, which directly shows PtZn/MWNT-E has much higher stability under reaction conditions.

Table S1. Summary of particle size of different catalysts

	Pt/MWNT-E	PtZn/MWNT-E	Pt/MWNT	PtZn/MWNT
TEM	2.1 ± 0.3 nm	3.2 ± 0.4 nm	3.7 ± 0.9 nm	27 ± 20 nm
PXRD	1.7 nm	3.2 nm	3.2 nm	18.9 nm

Table S2. XPS result summary of PtZn/MWNT

	Binding Energy (eV)			
	Pt $4f_{7/2}$	Zn $2p_{3/2}$	$Zn^{2+}2p_{3/2}$	Pt/Zn
PtZn/MWNT	70.8	1020.7	1022.9	1.1

Table S3. Summary of onset potential, peak potential, peak current density, and J_f/J_b ratio of different catalysts in acidic solution.

	$E_{on\text{-}set}$ (V)	E_f(V)	J_f(mA/cm^2)	J_f/J_b
PtZn/MWNT-E (3.2 nm)	0.154	0.640	1.030	1.46
PtZn/MWNT (8.6 nm)	0.325	0.684	0.884	1.56
PtZn/MWNT (27 nm)	0.343	0.683	0.581	1.01
PtZn-alloy/MWNT (2.8 nm)	0.217	0.656	0.444	1.15
Pt/MWNT (2.1 nm)	0.165	0.742	0.533	0.83
Pt/Vulcan (2.0 nm)	0.247	0.651	0.625	0.81

Table S4. Summary of onset potential, peak potential, peak current density, and J_f/J_b ratio of different catalysts in basic solution.

	$E_{on\text{-}set}$ (V)	E_f(V)	J_f(mA/cm^2)	J_f/J_b
PtZn/MWNT-E (3.2 nm)	-0.498	-0.102	1.030	2.35
PtZn/MWNT (8.6 nm)	-0.406	-0.027	0.561	1.91
PtZn/MWNT (27 nm)	-0.425	-0.029	0.465	1.89
PtZn-alloy/MWNT (2.8 nm)	-0.419	0.037	0.859	3.90
Pt/MWNT (2.1 nm)	-0.453	-0.138	0.430	-
Pt/Vulcan (2.0 nm)	-0.493	-0.157	0.788	3.29

Table S5. Literature summary of electrocatalytic results in MOR of alloy and intermetallic NPs.

Sample	J_f/J_b [b]	Mass activity (mA/μg)	Specific activity (mA/cm^2)	Stability [c] (retained current %)	Ref.
Pt_3Ti/C	-	0.149 [a]	0.307 [a]	73.8	11
Pt_3V/C	-	0.200 [a]	0.384 [a]	76.6	11
core-shell Ag@Pt/C	~1.18	-	1.11	-	12
core-shell Au@Pt/C	~1.06	-	1.65	-	12
FePtPd NWs	~1.09	0.489	-	-	13
TP-BNGN	1.25	-	0.647	~63.0	14
PtRu/HPMo-CS-CNTs	~1.67	0.232	0.316	74.3	15
cubic Pt-Zn NC	1.80	-	~0.720	-	16
spherical Pt-Zn NC	1.46	~0.190	~0.980	-	16
PtZn/MWNT-E (3.2 nm)	1.46	0.612	1.08	96.8	This work

[a] All the activity are the values at 0.5 V vs. Ag/AgCl.

[b] J_f/J_b values in Ref 12,13,15 was estimated by reading the peak current values from CV curves.

[c] 1000 cycles were measured in the stability test if not specified. 500 cycles and 300 cycles were used to evaluate the stability of catalysts in ref 15 and 14, respectively.

Table S6. ICP analysis of the composition of PtZn iNPs after the reaction.

sample	reaction condition	retained Pt%	retained Zn%
PtZn/MWNT-E (3.2 nm)	100 cycles in H_2SO_4	92.0	93.0
	1000 cycles in H_2SO_4	91.1	53.6
	1000 cycles in KOH	94.3	96.5

CHAPTER 3. CONVERTING CONFINED METAL@ZIF-8 TO INTERMETALLIC NANOPARTICLES SUPPORTED ON NITROGEN-DOPED CARBON FOR ELECTROCATALYSIS

Modified from a publication on the Nano Research

Zhiyuan Qi[1,2], Yuchen Pei[1,2], Tian Wei Goh[1,2], Zhaoyi Wang[1,3], Xinle Li[1,2], Mary Lowe[1], Raghu V. Maligal-Ganesh[1,2], Wenyu Huang[1,2 a.]

[1] Department of Chemistry, Iowa State University, Ames, Iowa, 50011, USA

[2] Ames Laboratory, U.S. Department of Energy, Ames, Iowa, 50011, USA

[3] Department of Chemistry, Beijing Normal University, Beijing, 100875, China

3.1 Abstract

We report a facile synthesis of intermetallic nanoparticles (iNPs) as electrocatalysts via one-pot pyrolysis of a zeolitic imidazolate framework, ZIF-8, encapsulated precious metal nanoparticles (NPs). ZIF-8 not only acts as the precursor for the N-doped carbon (NC) but also provides Zn source for the formation of intermetallic or alloy NPs with the encapsulated metals. The resultant sub-4 nm PtZn iNPs embedded inside NC exhibit high resistance towards sintering up to 1000 ˚C. Importantly, the methodology allows the fine tunability of composition (i.e., PdZn, RhZn iNPs and AuZn, RuZn alloy NPs) and size (2.4, 3.7, and 5.4 nm PtZn) of as-formed bimetallic NPs. To the best of our knowledge, this is the first time that MOFs serve multi-functions as secondary metal source, carbon precursor, and size-regulating reagent affording the formation of iNPs. This work opens a new avenue for the synthesis of highly uniform and stable iNPs.

3.2 Background

Pt-based alloy electrocatalysts have been intensively studied in polymer electrolyte membrane fuel cells (PEMFCs) over decades [1-4]. The secondary metals in alloys can improve

the performance of fuel cell by reducing Pt usage, tuning the electronic properties of surface sites and altering the binding strength of molecules [5]. Therefore, many Pt alloy catalysts are more active than Pt for oxygen reduction reaction (ORR) and methanol oxidation reaction (MOR) [1-3, 6]. However, the activity loss is an application challenge for many alloys due to the leaching of metals via the oxidative dissolution under electrochemical reaction condition [7]. The leaching of metals can also lead to the inevitable surface reconstruction [8]. To further enhance the catalytic performance of Pt alloys, it is essential to improve their structural and compositional homogeneity. Intermetallic compounds are special alloys with ordered structures and defined stoichiometry [9], rending them an ideal alternate to random alloys in terms of activities, stabilities and mechanism studies [10-16]. However, one of the challenges for intermetallic nanoparticles (iNPs) synthesis is the sintering under high-temperature treatments required for the formation of intermetallic phases [9], resulting in large particles and insufficient utilization of Pt for catalysis.

Encapsulation of nanoparticles (NPs) in inorganic shells (i.e., silica, titania, zirconia) is an effective approach to enhance their thermal stability [17, 18]. By using mesoporous silica ($mSiO_2$) as the encapsulation shell, our group obtained small and uniform PtZn iNPs (3.2 ± 0.4 nm) on multi-walled carbon nanotube (MNNT) as enhanced electrocatalysts [16]. The encapsulation strategy has also been used for synthesizing other Pt-based alloys and iNPs [19, 20]. To use these iNPs for electrocatalysis, an etching process using hazardous chemicals (e.g., HF, NaOH) is needed to remove the poorly conductive $mSiO_2$ shell. Carbon encapsulation, on the other hand, can be used to prevent NPs from aggregation and provide a highly conductive matrix for electrocatalysis.

Metal-organic frameworks (MOFs), an emerging class of porous crystalline materials, are widely exploited in the synthesis of size-controlled metal NPs [21, 22]. Because of their high

functional tunability and uniform cavities, two main approaches, namely “ship in a bottle” [23, 24] and “bottle around the ship” [25] are used to confine the growth of the NPs [26]. However, most MOFs are only thermally stable ranging from 250 to 500 ˚C [27], which cannot be directly used as the matrix for the synthesis of iNPs that require high-temperature annealing. Recently, nanostructures derived via the pyrolysis of MOFs have garnered increasing attention [28-31], such as (heteroatom-doped) porous carbons, metal alloys/metal oxides, and their hybrid composites [32-37]. These MOF-derived carbon materials perform as highly efficient electrocatalysts or catalyst supports [38, 39].

Since the pyrolysis temperature is typically 600 ˚C-1000 ˚C that is sufficient for the formation of intermetallic compounds, we envision a simultaneous formation of iNPs and porous carbon could be achieved by one-pot pyrolysis of MOF-encapsulated metal NPs. This general methodology has the potential for the synthesis of a broad spectrum of iNPs supported on porous carbon. Here, we report the synthesis of uniform PtZn iNPs encapsulated within N-doped porous carbon (denoted as Pt-Zn@NC) using this facile method, starting from Pt NPs encapsulated in ZIF-8 (Pt@ZIF-8). The size of PtZn iNPs can be simply tuned by altering the original size of Pt NPs. To the best of our knowledge, the monodisperse PtZn iNPs (2.4 ± 0.4 nm) in this study ranks the smallest iNPs synthesized to date. Remarkably, these small iNPs in Pt-Zn@NC exhibited high resistance to aggregation up to 1000 ˚C. This facile methodology is extended to the synthesis of PdZn/RhZn iNPs and AuZn/RuZn alloyed NPs. This study constitutes the first attempt to use MOF-encapsulated metal NPs as the precursor for the synthesis of intermetallic compounds.

3.3 Experimental Section

We synthesized NC encapsulated M-Zn iNPs (denoted as M-Zn@NC) through the pyrolysis of metal NPs embedded in ZIF-8 (M@ZIF-8). To obtain M@ZIF-8, metal NPs were first

synthesized and introduced during the formation of ZIF-8. We thus applied a pyrolysis in a reducing atmosphere to covert M@ZIF-8 to M-Zn@NC.

3.3.1 Synthesis of Metal NPs

2.6 nm Pt NPs [40]: 533 mg polyvinylpyrrolidone (PVP, MW=29000), 180 mL methanol, and 20 mL aqueous solution of H_2PtCl_6 (6.0 mM) were mixed and refluxed at 100 ˚C in a 500 mL flask for 3 hours under air. After removing the methanol by a rotary evaporator, Pt NPs were precipitated by acetone and centrifuged at 8000 rpm for 10 minutes.

1.7 nm Pt NPs [41]: 5 mL ethylene glycol (EG) solution of NaOH (0.5 M) was added to another 5 mL EG solution of H_2PtCl_6 (50 mM). After reaction at 160 ˚C for 3 h with Ar bubbling, particles were precipitated by adding 0.4 mL HCl (2M) and re-dispersed in methanol containing 4.9 mg of PVP (MW = 29000).

4.5 nm Pt NPs [42]: 20.8 mg K_2PtCl_4, 505 mg tetradecyltrimethylammonium bromide (C_{14}TAB), and 222 mg PVP (MW = 40000) were mixed in 20 mL EG with sonication. After reaction at 140 ℃ for 2 h under Ar protection, Pt NPs were precipitated by adding excessive acetone. The precipitate was further washed 5 times by dissolution/precipitation using ethanol/hexane (1/6: v/v). Purified Pt NPs were dispersed in methanol.

4 nm Rh NPs and 1.8 nm Ru NPs [42]: The synthetic condition and purification procedure are the same as those of 4.5 nm Pt NPs except for using 20.7 mg $RhCl_3 \cdot xH_2O$ and 20.7 mg $RuCl_3 \cdot xH_2O$ respectively as starting materials.

4 nm Au NPs [43]: 20 mL aqueous solution containing $HAuCl_4$ (0.25 mM) and trisodium citrate (0.25 mM) was prepared, into which 0.6 mL ice-cold, freshly prepared $NaBH_4$ (0.1 M) solution

was added. After stirring for 2h, PVP was added to the solution and stirred for another 24 h to stabilize Au NPs.

3.0 nm Pd NPs [44]: 2.0 mM of H_2PdCl_4 aqueous stock solution was freshly prepared by mixing 106.4 mg $PdCl_2$, 6.0 mL HCl (0.2 M), and 294 mL of DI water. 15 mL of the above solution, 21 mL H_2O, 14 mL ethanol, and 66.7 mg PVP (MW = 29000) was then mixed and refluxed in a 100-mL flask for 3 h under air.

3.3.2 Synthesis of M@ZIF-8 and control samples

M@ZIF-8 was synthesized via a reported method with slight modifications [25]. For a typical preparation of Pt@ZIF-8, the as-synthesized Pt NPs were extensively washed by precipitation/dissolution using hexane/ethanol to remove the extra PVP and dispersed in methanol with the Pt concentration of 0.26 mg/mL (Pt NPs stock solution). 15 mL $Zn(NO_3)_2$ $6H_2O$ (25 mM) methanol solution was first mixed with 1 mL Pt NPs stock solution, then 15 mL 2-methylimidazole (2-mIm, 400 mM) methanol solution was sequentially added into the mixture without stirring. 2 mL Pt NPs solution were then added four times every 15 min. The final solution was kept at room temperature for 24 h, then centrifuged, washed with methanol 3 times and dried at 65 ˚C to afford Pt@ZIF-8 particles. Other metal NPs were also extensively washed to prevent the inefficient encapsulation of metal NPs induced by the competitive adsorption of free PVP [25], and dispersed in methanol. M@ZIF-8 was then synthesized through the identical procedure.

Synthesis of Pt-Zn/NC-800

Pure ZIF-8 particles were first synthesized by mixing 15 mL $Zn(NO_3)_2$ $6H_2O$ methanol solution (25 mM) and 15 mL 2-methylimidazole (2-mIm) methanol solution (400 mM). The

mixture solution was left at room temperature without stirring for 24 h. After centrifuged and washed by methanol 3 times, the as-synthesized ZIF-8 particles were dispersed into 30 mL of methanol by sonication. 9 mL of Pt NPs stock solution (0.26 mg/mL) was directly added into the ZIF-8 solution and stirred for 1 h. After washed and dried, the ground Pt/ZIF-8 powders were converted to Pt-Zn/NC-800 via pyrolysis under 10% H_2/argon flow at 800 ˚C for 4h, with a ramping rate of 2 ˚C/min.

Synthesis of Pt-Zn-IW@NC-800

Pure ZIF-8 particles were prepared and purified via the same method and dried at 65 ˚C. The desired amount of K_2PtCl_4 aqueous solution was added to the ground ZIF-8 powders to prepare homogeneous Pt^{2+}@ZIF-8 composites with 3.2% Pt loading. The volume of the solvent was controlled the same as the pore volume of used ZIF-8. Pt^{2+}@ZIF-8 was thus vacuum dried and converted to Pt-Zn-IW@NC-800 via pyrolysis under 10% H_2/argon flow at 800 ˚C for 4h, with a ramping rate of 2 ˚C/min.

3.3.3 Synthesis of M-Zn@NC through pyrolysis

M@ZIF-8 was first ground to powder, and then transferred to a small quartz vial and placed in the tube furnace. The pyrolysis was conducted under a 50 mL/min flow of 10% H_2/Ar at different temperatures for 4 h with a ramping rate of 2 ˚C/min.

3.3.4 Characterization

Powder X-ray diffraction (PXRD) patterns of the samples were acquired by a STOE Stadi P powder diffractometer using Cu *K*α radiation (40 kV, 40 mA, λ=0.1541 nm). N_2 physisorption

experiments were conducted by using Micromeritics 3Flex surface characterization analyzer at 77 K. All the samples were activated at 200 ˚C for 12 h under vacuum ($<10^{-5}$ torr) before measurements. Transmission electron microscopy (TEM) images were acquired by using a Tecnai G2 F20 electron microscope operated at 200 kV. High-angle annular dark-field scanning transmission electron microscope (HAADF-STEM) imaging was performed on a Titan Themis 300 probe corrected TEM with a Super-X Energy-dispersive X-ray Spectroscopy (EDX) detector. Inductively coupled plasmon-mass spectrometry (ICP–MS, X Series II, Thermo Scientific) was performed to determine the actual metal content. Samples were digested by boiled aqua regia before ICP analysis. X-ray photoelectron spectroscopy (XPS) spectra were measured by a PHI 5500 Multi-technique system (Physical Electronics, Chanhassen, MN) equipped with a monochromatized Al *K*α X-ray source (1486.6 eV).

3.3.5 Electrochemical Measurements

Electrochemical measurements were performed in a three-electrode system using a potentiostat (VSL-300 Bio-Logic Science Instruments). The catalysts were dispersed in a solvent mixture (H_2O: Isopropanol: 5% Nafion solution = 4: 1: 0.025), and the catalyst concentration was adjusted to 2 mg/mL. After sonication for 30 min, 10 μL of the well-dispersed catalyst ink was transferred onto a rotational ring-disk electrode (RRDE, 5 mm diameter), which was used as the working electrode. A platinum wire was used as the counter electrode and a saturated Ag/AgCl electrode was used as the reference electrode. The electrochemical cell was purged with Ar for 30 min before cyclic voltammetry (CV) tests. All water used in the experiments was Millipore ultrapure water (18.2 MΩ).

3.4 Results and Discussions

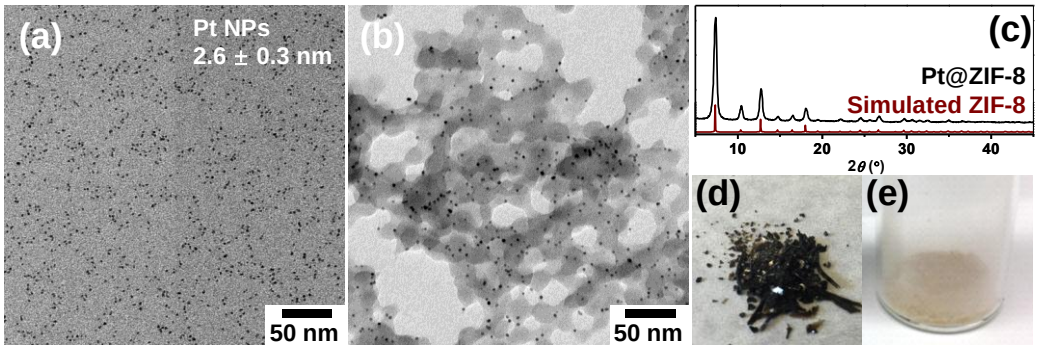

Figure 1 TEM images of (a) as-synthesized PVP-Pt NPs; (b) Pt@ZIF-8 nanocomposite; (c) PXRD pattern of Pt@ZIF-8; (d, e) digital photographs of dried Pt@ZIF-8 (d) before and (e) after grinding.

PVP-capped Pt NPs was first synthesized and encapsulated in ZIF-8 following a "bottle around ship" protocol [25]. As shown in Fig. 1a, the as-prepared Pt NPs have an average diameter of 2.6 ± 0.3 nm. After thoroughly washing away the excess PVP, the Pt NPs stock solution was mixed with precursor solutions of ZIF-8 (2-mIm/Zn ratio = 16) and kept at room temperature for 24 h without stirring to afford Pt@ZIF-8 composites (Fig. 1b). Using a high linker to metal ratio, small ZIF-8 NPs (~25 nm) are synthesized, which further assemble into a porous crosslinked network. Inter-particle pores (~20-50 nm) are formed during the assembly of ZIF-8 NPs. Pt NPs were encapsulated near edges of ZIF-8 NPs while few were located at the center, indicating that Pt NPs are not the nucleation centers for ZIF-8 growth. Therefore, we reasoned that ZIF-8 NPs were formed through homogenous nucleation, and Pt NPs were adsorbed during the growth of ZIF-8. The self-nucleation mechanism was further proved by that pure ZIF-8 NPs without encapsulated Pt NPs were also observed in Fig. 1b. The PXRD pattern of Pt@ZIF-8 nanocomposite (Fig. 1c) coincides well with the simulated pattern of ZIF-8. The diffraction peaks of Pt NPs are not observable in PXRD patterns, presumably due to the relatively low loadings

(3.2%) and small sizes (2.6 nm) of Pt NPs. Fig. 1d shows the dry Pt@ZIF-8 powders, which were ground thoroughly prior to pyrolysis to ensure a homogeneous heating.

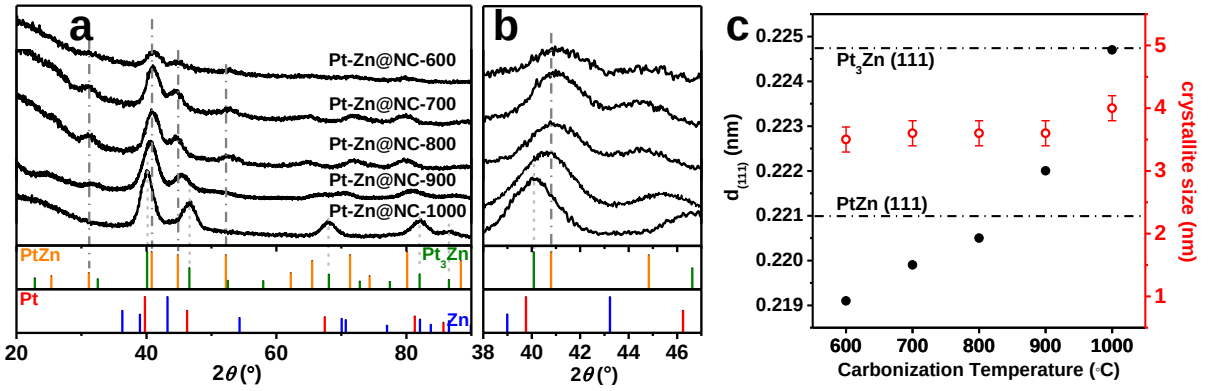

Figure 2 (a) PXRD patterns of Pt-Zn@NC-n samples synthesized at different pyrolysis temperature, ranging from 600 to 1000 ˚C; (b) the zoom-in region between 38˚ and 47˚ shows a shift to low angle of the most intense diffraction peak as pyrolysis temperature increases; (c) lattice distances and crystallite sizes of Pt-Zn@NC-n calculated from the most intensive diffraction peaks. The two horizontal dash lines represent the theoretical lattice distances of Pt_3Zn (111) (top) and PtZn (111) (bottom) respectively. The calculated lattice distances show the lattice expansion with the increasing temperatures while the crystallite sizes almost retained up to 1000 ˚C.

The pyrolysis of Pt@ZIF-8 was performed at different temperatures (600, 700, 800, 900, and 1000 ˚C). PXRD patterns of samples after pyrolysis (denoted as Pt-Zn@NC-n, n represents the pyrolysis temperature) were summarized in Fig. 2. The crystallinity of ZIF-8 was not retained after pyrolysis leading to the amorphous feature of derived carbon. Pt-Zn@NC-600, 700, 800 and 900 samples showed diffraction peaks aligning well with those of PtZn standard pattern, indicating the formation of PtZn intermetallic phases (P_4/mmm, $L1_0$ type, AuCu structure). The major intermetallic PtZn phase is readily obtained at 600 ˚C while the crystal structure becomes more

defined as temperature increases to 900 ˚C. However, when applying 1000 ˚C, the PXRD pattern of Pt-Zn@NC-1000 suggests the formation of another intermetallic phase, Pt_3Zn (Fig. 2a). We observed a consistent shift of the major peak at 40~41˚ to low angles associated with increasing pyrolysis temperatures (Fig. 2b). The shifting to the lower angle at higher pyrolysis temperatures can be correlated to the lattice expansion (Fig. 2c, Table S1 in the Electronic Supplementary Material (ESM)) due to the evaporation of metallic Zn, which is in line with ICP-MS measurements (Table S2 in the ESM). Even though less Zn (Zn/Pt = 0.54) remains in the samples treated at 900 ˚C, major intermetallic PtZn phase was maintained because intermetallic PtZn can be obtained with a Zn/Pt atomic ratio varying from 0.47 to 1 [45]. This wide range of Zn/Pt ratio also explains the variation of $d_{(111)}$ around the theoretical values (0.221 nm) induced by different carbonization temperatures (Fig. 2c). However, when elevated to 1000 ˚C, insufficient Zn (Zn/Pt = 0.44) will direct the formation of intermetallic Pt_3Zn phase. The crystallite sizes of Pt-Zn iNPs were calculated by Scherrer's equation using the major peaks (40~41˚, Table S3 in the ESM). Interestingly, the particle size was well retained as small as 4.0 nm up to 1000 ˚C while only slight increase (~ 0.5 nm) in the crystallite size was observed among different temperatures, as shown in Fig. 2c. Therefore, we conclude that ZIF-8 perform as a Zn source for the synthesis of iNPs and the ZIF-derived NC renders sufficient thermal stability to prevent iNPs sintering at high temperatures. Additionally, pyrolysis temperature plays a critical role in the final crystal structures by controlling the evaporation of Zn.

Structural information (i.e. particle size and morphology) of Pt-Zn@NC composites were further examined by TEM (Fig. 3 and Fig. S1 in the ESM). As shown in Fig. 3a, the morphology of ZIF-8 was no longer retained and larger carbon chunks were observed in Pt-Zn@NC-800, revealing the deformation of ZIF-8 during the pyrolysis. As for PtZn iNPs, no obvious aggregation

was observed, which is in line with the diffraction peak width in their XRD patterns. The monodispersity and well-confined particle sizes of Pt-Zn@NC-n synthesized at all other pyrolysis temperatures were further confirmed by TEM images (Fig. S1 in the ESM). Notably, the average particle diameters of PtZn iNPs (e.g., 3.7 ± 0.6 nm for Pt-Zn@NC-800) were almost identical regardless of the pyrolysis temperature, as shown in Fig. 3d and summarized in Table S3 in the ESM. Comparing the small sizes as extracted from XRD and TEM, we suggest that the ZIF-derived NC could strictly confine the growth of intermetallic particles. It is worth to emphasize that the average particle diameters based on TEM are similar to the calculated crystallite size from PXRD patterns, indicating the single crystallinity of these PtZn iNPs. The high crystallinity of PtZn was further characterized by HRTEM (Fig. 3c). Two lattice distances were measured as 0.35 nm and 0.22 nm, which are in good agreement with the lattice spacing of PtZn (001) and (111) planes. EDS elemental mapping of Pt-Zn@NC-800 (Fig. 3 e-h) shows that Zn and Pt are homogeneously dispersed in all particles. However, Zn signals also present in the NC support and near the particle surfaces. We hence confer that the extra Zn content determined by ICP-MS and XPS (Table S2 and S4 in the ESM) remains in the NC. To evaluate the sintering resistance of PtZn iNPs, we calculated the theoretical particle diameter range of PtZn and Pt_3Zn (green and orange rectangles in Fig. 3d) induced by the Zn incorporation. The measured diameters of Pt-Zn@NC-n (600-900) agree well with the theoretical values with only 10% overgrowth (0.4 nm). The overgrowth in sizes of Pt-Zn@NC-1000 increases to 30%, but the particle sizes were still ca. 3.7 nm, which is considerably small, given 1000 ˚C pyrolysis temperature and the high Pt loading. Therefore, ZIF-8 could effectively prevent the sintering of encapsulated NPs at high temperatures through the cage confinement of the derived carbon.

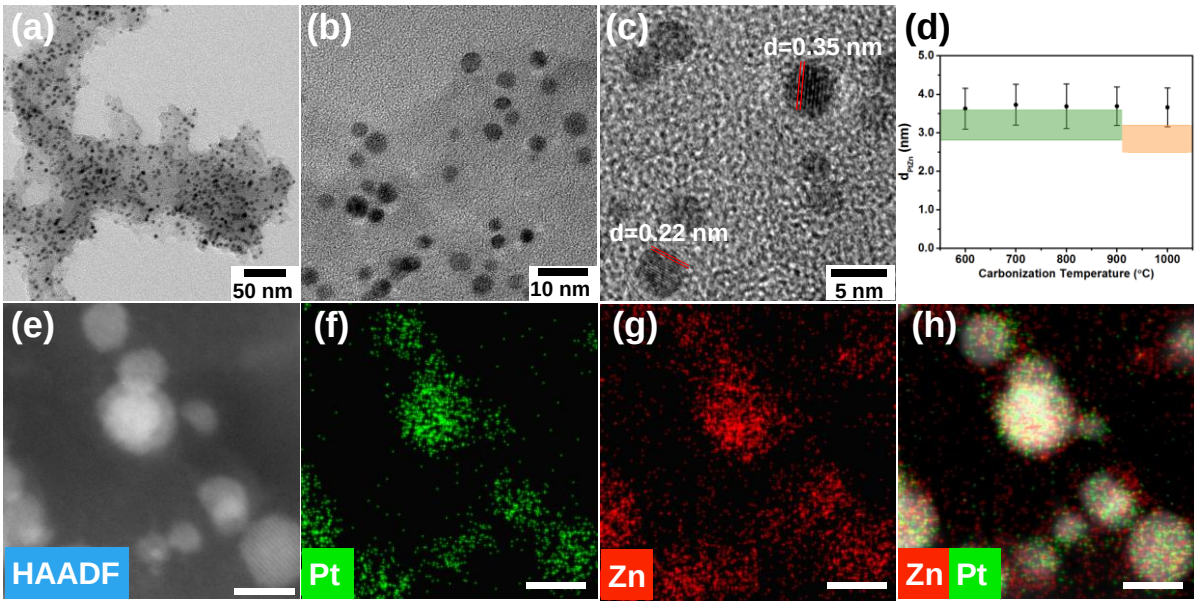

Figure 3 (a, b) TEM images of Pt-Zn@NC-800, (c) HRTEM image of PtZn iNPs and (d) average diameters of PtZn@NC-n particles measured from TEM images (200 counts). Shaded green and orange areas are the theoretical average particle diameter range of PtZn and Pt_3Zn iNPs, calculated by the diameter of parent Pt NPs and associated crystal densities. (e) HAADF-STEM image of Pt-Zn@NC-800 and its' EDX elemental mapping of (f) Pt, (g) Zn, and (h) Pt + Zn. Scale bar is 4 nm for (e-h).

To further demonstrate the significance of cage-confinement, two control samples (Pt/ZIF-8 and Pt^{2+}@ZIF-8) were synthesized. Pt/ZIF-8 were prepared by adding 9 mL Pt NPs stock solution to pre-synthesized ZIF-8 solution, and the Pt NPs were expected to be deposited on the external surface of ZIF-8. Pt^{2+}@ZIF-8 were synthesized by an incipient wetness impregnation (IW) method to introduce Pt precursor (i.e., K_2PtCl_4) inside ZIF-8, where $PtCl_4^{2-}$ ions can more freely diffuse in ZIF-8 frameworks. Both samples were treated under the identical pyrolysis condition to afford Pt-Zn/NC-800 and Pt-Zn-IW@NC-800. As shown in Fig. S2 (in the ESM), larger PtZn iNPs with big size deviation were formed in both Pt-Zn/NC-800 (8.6 ± 3.4 nm) and Pt-Zn-IW@NC-800 (28.3 ± 14.5 nm), indicating the lack of size confinement in both samples. The sever

aggregation observed on Pt-Zn-IW@NC suggests the bigger Pt NPs were formed even before the decomposition of ZIF-8, as IW method generally produces the particles on the surface of the framework [46, 47]. This result not only confirms the successful encapsulation of Pt NPs using our methodology but also suggests that the cage confinement is critical to effectively constrain the growth of iNPs.

We employed N_2 physisorption to study the porosity of ZIF-8, Pt@ZIF-8, and Pt-Zn@NC-800 (Fig. 4). The isotherms of the three samples show type-IV characteristics with a distinct H1 type hysteresis loop starting around $P/P_0 = 0.8$, which is not typical for ZIF-8 [25, 48, 49]. The Barrett-Joyner-Halenda (BJH) pore sizes distributions in 2-100 nm region (Fig. 4c) show that ZIF-8 and Pt@ZIF-8 both have the pores with an average diameter of ~23 nm that are larger than the pore diameter of Pt-Zn@NC-800 (14 nm), indicating the shrinkage of the whole framework during pyrolysis. We infer that these pores are originated from inter-particle pores in the crosslinked structure induced by the assembly of ZIF-8 nanocrystals (Fig. 1b). We noticed that some micropores were partially lost and smaller micropores were generated during pyrolysis, as evidenced by the pore size distributions of Pt-Zn@NC-800 in Fig. 4b by using Non-Local Density Function Theory (NLDFT) method. The Brunauer-Emmett-Teller (BET) surface area of ZIF-8 was measured as 1500 m^2/g and decreased to 1400 m^2/g in Pt@ZIF-8 (Table S5 in the ESM) due to the loading of Pt NPs. After pyrolysis, BET surface area of Pt-Zn@NC-800 (990 m^2/g) is still high while the decrease is due to the decomposition of the ZIF-8 structure.

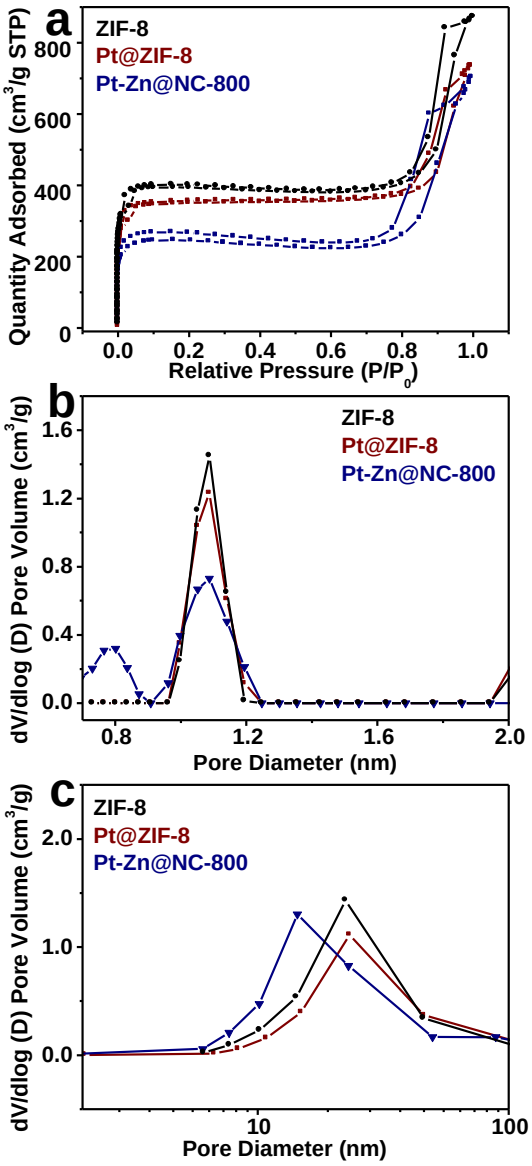

Figure 4 (a) N_2 physisorption isotherm and the corresponding size distribution (b, c) of pure ZIF, Pt@ZIF-8, and Pt-Zn@NC-800. Pore diameter distribution in (b) the microporous region from 0.7 to 2 nm using NLDFT method and (c) the mesoporous region from 2 to 100 nm using BJH method.

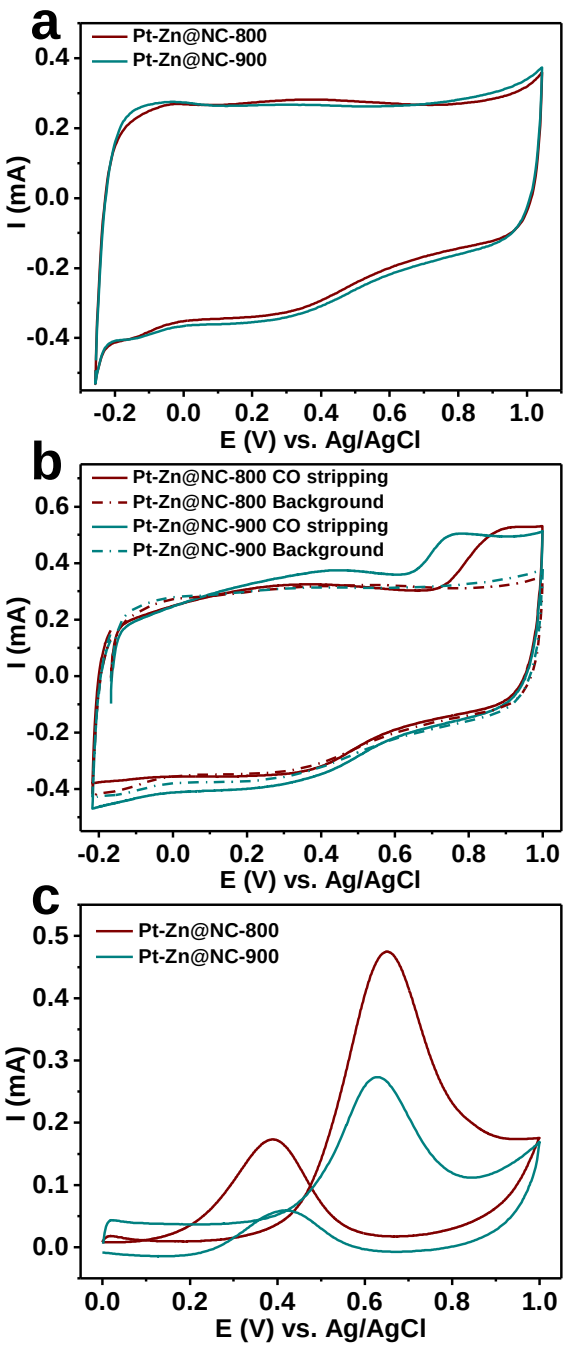

Figure 5 CV scans of Pt-Zn@NC-800, 900 in (a) Ar purged 0.1 M $HClO_4$; (b) CO stripping and (c) 0.1 M $HClO_4$ + 1 M methanol solutions (capacitive current removed). Both H_2 and CO have weak adsorption on Pt-Zn surface, leading to the higher tolerance of poisoning in MOR.

With the desired characterization of Pt-Zn@NC samples, we investigated their electrocatalytic performance by MOR. The catalysts were activated by 3 M HCl etching overnight to remove the extra Zn in the NC framework. The PtZn crystal structure was retained after etching and no Pt loss was observed, as confirmed by PXRD (Fig. S3 in the ESM) and ICP-MS analysis (Table S2 in the ESM). CV scans were first applied in 0.1 M $HClO_4$. A large charging current was observed while the hydrogen redox peaks (between -0.2 to 0.15 V vs. Ag/AgCl) were not clearly observed, indicating the inhibition of the H_2 adsorption. As shown in Fig. 5b, CO molecules were also weakly adsorbed onto the Pt-Zn surface. It is possible that Pt-Zn surface was partially covered by an amorphous carbon layer weakening the adsorption of small molecules. To better evaluate the MOR activity of Pt-Zn@NC, we remove the capacitive current (Fig. S4 in the ESM) and the adjusted CV curves are presented in Fig. 5c. Although the activities of both Pt-Zn@NC-800 and 900 are limited by the surface carbon coverage, Pt-Zn@NC-800 shows a better activity than Pt-Zn@NC-900, probably due to the less carbon coverage, high N content (Fig. S5, Table S4 in the ESM) and more precise Pt-Zn crystal structure. It is noteworthy that the forward to backward peak ratios of both Pt-Zn@NC-800 and 900 are large as 2.6 and 4.2, showing a high tolerance towards poisoning effect from intermediates [15].

The methodology for the synthesis of intermetallic compounds embedded within N doped porous carbon can be extended to other metal NPs and particle sizes. A series of M@ZIF-8 were successfully prepared including Au (4.0 nm), Pd (3.2 nm), Ru (1.8 nm), Rh (3.3 nm) and Pt (1.7 nm and 4.3 nm). The loading of metal NPs was confirmed by TEM images (Fig. S6 in the ESM). PXRD patterns demonstrate that all M@ZIF-8 composites possess identical diffraction patterns to that of ZIF-8 (Fig. S7 in the ESM). M@ZIF-8 was then converted to M-Zn@NC via the pyrolysis at 800 ˚C in 10% H_2/Ar. Similar to Pt-Zn@NC-800, ZIF-8 can efficiently prevent the aggregation

of encapsulated particles (Fig. S6, Table S6 in the ESM). PXRD patterns of resultant M-Zn particles (Fig. S8 in the ESM) indicate PdZn and RhZn intermetallic iNPs were readily formed, while AuZn and RuZn NPs exhibit alloy phases under this pyrolysis condition. Moreover, the size of PtZn iNPs can be easily tuned by changing the size of parent Pt NPs leading to three different sizes (2.4 nm, 3.7 nm, 5.4 nm) of PtZn iNPs (Fig. S9-10 and Table S7 in the ESM). It is noteworthy that PtZn (2.4 ± 0.4 nm) is the smallest iNPs synthesized and stable at 800 ˚C to date (Table S8 in the ESM) [50-57]. We demonstrated the size and compositional tunability of our method in synthesizing ZIF-8 derived iNPs, and the scope of using different types of MOFs is currently underway.

3.5 Conclusion

In summary, we have demonstrated a facile one-pot *in situ* strategy for the synthesis of various iNPs embedded in N-doped porous carbon via direct pyrolysis of M@ZIF-8 in a reducing atmosphere. During the pyrolysis, N-doped porous carbon derived from ZIF-8 serves as an effective capsule to prevent the sintering of iNPs through the cage-confinement. Meanwhile, ZIF-8 also functions as the Zn source for iNPs. The generality of the synthetic method was proved by controlling the size and composition of metal NPs. The obtained iNPs feature tunable sizes, excellent thermal stability, and active for electrocatalysis. This novel synthesis of size-tunable, monodisperse and thermally stable iNPs-embedded porous carbon composites from the pyrolysis of metal NPs-embedded MOFs opens up new opportunities for the development of high-performance electrocatalysts.

3.6 Acknowledgements

Acknowledgment is made to the donors of the American Chemical Society Petroleum Research Fund for support of this research. We thank Gordon J. Miller for the use of the X-ray diffractometer. We also thank Dapeng Jing at the Materials analysis and research laboratory (MARL) of Iowa State University for the assistance on XPS measurement.

3.7 References

1. Wang, Y. J.; Zhao, N. N.; Fang, B. Z.; Li, H.; Bi, X. T. T.; Wang, H. J. *Chem. Rev.* **2015,** *115* (9), 3433-3467.

2. Shao, M. H.; Chang, Q. W.; Dodelet, J. P.; Chenitz, R. *Chem. Rev.* **2016,** *116* (6), 3594-3657.

3. Wu, J. B.; Yang, H. *Accounts Chem. Res.* **2013,** *46* (8), 1848-1857.

4. You, H. J.; Yang, S. C.; Ding, B. J.; Yang, H. *Chem. Soc. Rev.* **2013,** *42* (7), 2880-2904.

5. Furukawa, S.; Komatsu, T. *ACS Catal.* **2017,** *7* (1), 735-765.

6. Bing, Y. H.; Liu, H. S.; Zhang, L.; Ghosh, D.; Zhang, J. J. *Chem. Soc. Rev.* **2010,** *39* (6), 2184-2202.

7. Watanabe, M.; Tsurumi, K.; Mizukami, T.; Nakamura, T.; Stonehart, P. *J Electrochem Soc* **1994,** *141* (10), 2659-2668.

8. Wu, J. F.; Yuan, X. Z.; Martin, J. J.; Wang, H. J.; Zhang, J. J.; Shen, J.; Wu, S. H.; Merida, W. *J Power Sources* **2008,** *184* (1), 104-119.

9. Yan, Y. C.; Du, J. S. S.; Gilroy, K. D.; Yang, D. R.; Xia, Y. N.; Zhang, H. *Adv. Mater.* **2017,** *29* (14).

10. Bu, L. Z.; Zhang, N.; Guo, S. J.; Zhang, X.; Li, J.; Yao, J. L.; Wu, T.; Lu, G.; Ma, J. Y.; Su, D.; Huang, X. Q. *Science* **2016,** *354* (6318), 1410-1414.

11. Chen, C.; Kang, Y. J.; Huo, Z. Y.; Zhu, Z. W.; Huang, W. Y.; Xin, H. L. L.; Snyder, J. D.; Li, D. G.; Herron, J. A.; Mavrikakis, M.; Chi, M. F.; More, K. L.; Li, Y. D.; Markovic, N. M.; Somorjai, G. A.; Yang, P. D.; Stamenkovic, V. R. *Science* **2014,** *343* (6177), 1339-1343.

12. Huang, X. Q.; Zhao, Z. P.; Cao, L.; Chen, Y.; Zhu, E. B.; Lin, Z. Y.; Li, M. F.; Yan, A. M.; Zettl, A.; Wang, Y. M.; Duan, X. F.; Mueller, T.; Huang, Y. *Science* **2015,** *348* (6240), 1230-1234.

13. Li, M. F.; Zhao, Z. P.; Cheng, T.; Fortunelli, A.; Chen, C. Y.; Yu, R.; Zhang, Q. H.; Gu, L.; Merinov, B. V.; Lin, Z. Y.; Zhu, E. B.; Yu, T.; Jia, Q. Y.; Guo, J. H.; Zhang, L.; Goddard, W. A.; Huang, Y.; Duan, X. F. *Science* **2016,** *354* (6318), 1414-1419.

14. Stamenkovic, V. R.; Fowler, B.; Mun, B. S.; Wang, G. F.; Ross, P. N.; Lucas, C. A.; Markovic, N. M. *Science* **2007,** *315* (5811), 493-497.

15. Kang, Y. J.; Pyo, J. B.; Ye, X. C.; Gordon, T. R.; Murray, C. B. *ACS Nano* **2012,** *6* (6), 5642-5647.

16. Yang, Q.; Xu, Q.; Jiang, H.-L. *Chem Soc Rev* **2017,** *46* (15), 4774-4808.

17. Xiao, C. X.; Maligal-Ganesh, R. V.; Li, T.; Qi, Z. Y.; Guo, Z. Y.; Brashler, K. T.; Goes, S.; Li, X. L.; Goh, T. W.; Winans, R. E.; Huang, W. Y. *Chemsuschem* **2013,** *6* (10), 1915-1922.

18. Joo, S. H.; Park, J. Y.; Tsung, C. K.; Yamada, Y.; Yang, P. D.; Somorjai, G. A. *Nat. Mater.* **2009,** *8* (2), 126-131.

19. Pei, Y. C.; Maligal-Ganesh, R. V.; Xiao, C. X.; Goh, T. W.; Brashler, K.; Gustafson, J. A.; Huang, W. Y. *Nanoscale* **2015,** *7* (40), 16721-16728.

20. Maligal-Ganesh, R. V.; Xiao, C. X.; Goh, T. W.; Wang, L. L.; Gustafson, J.; Pei, Y. C.; Qi, Z. Y.; Johnson, D. D.; Zhang, S. R.; Tao, F.; Huang, W. Y. *ACS Catal.* **2016,** *6* (3), 1754-1763.

21. An, B.; Cheng, K.; Wang, C.; Wang, Y.; Lin, W. *ACS Catalysis* **2016,** *6* (6), 3610-3618.

22. Yang, Q. H.; Xu, Q.; Yu, S. H.; Jiang, H. L. *Angew. Chem. Int. Edit.* **2016,** *55* (11), 3685-3689.

23. Li, X. L.; Goh, T. W.; Li, L.; Xiao, C. X.; Guo, Z. Y.; Zeng, X. C.; Huang, W. Y. *ACS Catal.* **2016,** *6* (6), 3461-3468.

24. Li, X. L.; Van Zeeland, R.; Maligal-Ganesh, R. V.; Pei, Y. C.; Power, G.; Stanley, L.; Huang, W. Y. *ACS Catal.* **2016,** *6* (9), 6324-6328.

25. Lu, G.; Li, S. Z.; Guo, Z.; Farha, O. K.; Hauser, B. G.; Qi, X. Y.; Wang, Y.; Wang, X.; Han, S. Y.; Liu, X. G.; DuChene, J. S.; Zhang, H.; Zhang, Q. C.; Chen, X. D.; Ma, J.; Loo, S. C. J.; Wei, W. D.; Yang, Y. H.; Hupp, J. T.; Huo, F. W. *Nat. Chem.* **2012,** *4* (4), 310-316.

26. Zhu, Q. L.; Xu, Q. *Chem. Soc. Rev.* **2014,** *43* (16), 5468-5512.

27. Furukawa, H.; Cordova, K. E.; O'Keeffe, M.; Yaghi, O. M. *Science* **2013,** *341* (6149), 974-+.

28. Liu, B.; Shioyama, H.; Akita, T.; Xu, Q. *J. Am. Chem. Soc.* **2008,** *130* (16), 5390-+.

29. Zhao, S. L.; Yin, H. J.; Du, L.; He, L. C.; Zhao, K.; Chang, L.; Yin, G. P.; Zhao, H. J.; Liu, S. Q.; Tang, Z. Y. *ACS Nano* **2014,** *8* (12), 12660-12668.

30. You, B.; Jiang, N.; Sheng, M. L.; Drisdell, W. S.; Yano, J.; Sun, Y. J. *ACS Catal.* **2015,** *5* (12), 7068-7076.

31. Xu, Y. T.; Xiao, X. F.; Ye, Z. M.; Zhao, S. L.; Shen, R. G.; He, C. T.; Zhang, J. P.; Li, Y. D.; Chen, X. M. *J. Am. Chem. Soc.* **2017,** *139* (15), 5285-5288.

32. Pei, Y. C.; Qi, Z. Y.; Li, X. L.; Maligal-Ganesh, R. V.; Goh, T. W.; Xiao, C. X.; Wang, T. Y.; Huang, W. Y. *J. Mater. Chem. A* **2017,** *5* (13), 6186-6192.

33. Li, X. L.; Zhang, B. Y.; Fang, Y. H.; Sun, W. J.; Qi, Z. Y.; Pei, Y. C.; Qi, S. Y.; Yuan, P. Y.; Luan, X. C.; Goh, T. W.; Huang, W. Y. *Chem. Eur. J.* **2017,** *23* (18), 4266-4270.

34. Yang, Q. H.; Xu, Q.; Jiang, H. L. *Chem. Soc. Rev.* **2017,** *46* (15), 4774-4808.

35. Ji, S. F.; Chen, Y. J.; Fu, Q.; Chen, Y. F.; Dong, J. C.; Chen, W. X.; Li, Z.; Wang, Y.; Gu, L.; He, W.; Chen, C.; Peng, Q.; Huang, Y.; Duan, X. F.; Wang, D. S.; Draxl, C.; Li, Y. D. *J. Am. Chem. Soc.* **2017,** *139* (29), 9795-9798.

36. Chen, Y. J.; Ji, S. F.; Wang, Y. G.; Dong, J. C.; Chen, W. X.; Li, Z.; Shen, R. A.; Zheng, L. R.; Zhuang, Z. B.; Wang, D. S.; Li, Y. D. *Angew. Chem. Int. Edit.* **2017,** *56* (24), 6937-6941.

37. Chen, Y. Z.; Wang, C. M.; Wu, Z. Y.; Xiong, Y. J.; Xu, Q.; Yu, S. H.; Jiang, H. L. *Adv. Mater.* **2015,** *27* (34), 5010-5016.

38. Xia, W.; Mahmood, A.; Zou, R. Q.; Xu, Q. *Energ. Environ. Sci.* **2015,** *8* (7), 1837-1866.

39. Zhang, W.; Wu, Z. Y.; Jiang, H. L.; Yu, S. H. *J. Am. Chem. Soc.* **2014,** *136* (41), 14385-14388.

40. Teranishi, T.; Hosoe, M.; Tanaka, T.; Miyake, M. *J Phys Chem B* **1999,** *103* (19), 3818-3827.

41. Song, H.; Rioux, R. M.; Hoefelmeyer, J. D.; Komor, R.; Niesz, K.; Grass, M.; Yang, P. D.; Somorjai, G. A. *J. Am. Chem. Soc.* **2006,** *128* (9), 3027-3037.

42. Pei, Y. C.; Xiao, C. X.; Goh, T. W.; Zhang, Q. H.; Goes, S. N.; Sun, W. J.; Huang, W. Y. *Surf. Sci.* **2016,** *648*, 299-306.

43. Jana, N. R.; Gearheart, L.; Murphy, C. J. *Langmuir* **2001,** *17* (22), 6782-6786.

44. Li, Y.; Boone, E.; El-Sayed, M. A. *Langmuir* **2002,** *18* (12), 4921-4925.

45. Massalski, T. B.; Okamoto, H.; Subramanian, P. R.; Kacprzak, L., *Binary Alloy Phase Diagrams, 2nd Edition*. ASM International: Ohio, 1990.

46. Rosler, C.; Fischer, R. A. *Crystengcomm* **2015,** *17* (2), 199-217.

47. Stephenson, C. J.; Hupp, J. T.; Farha, O. K. *Inorg Chem Front* **2015,** *2* (5), 448-452.

48. Park, K. S.; Ni, Z.; Cote, A. P.; Choi, J. Y.; Huang, R. D.; Uribe-Romo, F. J.; Chae, H. K.; O'Keeffe, M.; Yaghi, O. M. *Proc. Natl. Acad. Sci. USA* **2006,** *103* (27), 10186-10191.

49. Jiang, H. L.; Liu, B.; Akita, T.; Haruta, M.; Sakurai, H.; Xu, Q. *J. Am. Chem. Soc.* **2009,** *131* (32), 11302-11303.

50. Zhou, H. R.; Yang, X. F.; Li, L.; Liu, X. Y.; Huang, Y. Q.; Pan, X. L.; Wang, A. Q.; Li, J.; Zhang, T. *ACS Catal.* **2016,** *6* (2), 1054-1061.

51. Iihama, S.; Furukawa, S.; Komatsu, T. *ACS Catal.* **2016,** *6* (2), 742-746.

52. Furukawa, S.; Yoshida, Y.; Komatsu, T. *ACS Catal.* **2014,** *4* (5), 1441-1450.

53. Du, X. X.; He, Y.; Wang, X. X.; Wang, J. N. *Energ. Environ. Sci.* **2016,** *9* (8), 2623-2632.

54. Cui, Z. M.; Chen, H.; Zhou, W. D.; Zhao, M. T.; DiSalvo, F. J. *Chem. Mater.* **2015,** *27* (21), 7538-7545.

55. Shim, J.; Lee, J.; Ye, Y.; Hwang, J.; Kim, S. K.; Lim, T. H.; Wiesner, U.; Lee, J. *ACS Nano* **2012,** *6* (8), 6870-6881.

56. Chung, D. Y.; Jun, S. W.; Yoon, G.; Kwon, S. G.; Shin, D. Y.; Seo, P.; Yoo, J. M.; Shin, H.; Chung, Y. H.; Kim, H.; Mun, B. S.; Lee, K. S.; Lee, N. S.; Yoo, S. J.; Lim, D. H.; Kang, K.; Sung, Y. E.; Hyeon, T. *J. Am. Chem. Soc.* **2015,** *137* (49), 15478-15485.

57. Magno, L. M.; Sigle, W.; van Aken, P. A.; Angelescu, D.; Stubenrauch, C. *Phys Chem Chem Phys* **2011,** *13* (20), 9134-9136.

3.8 Supporting Information

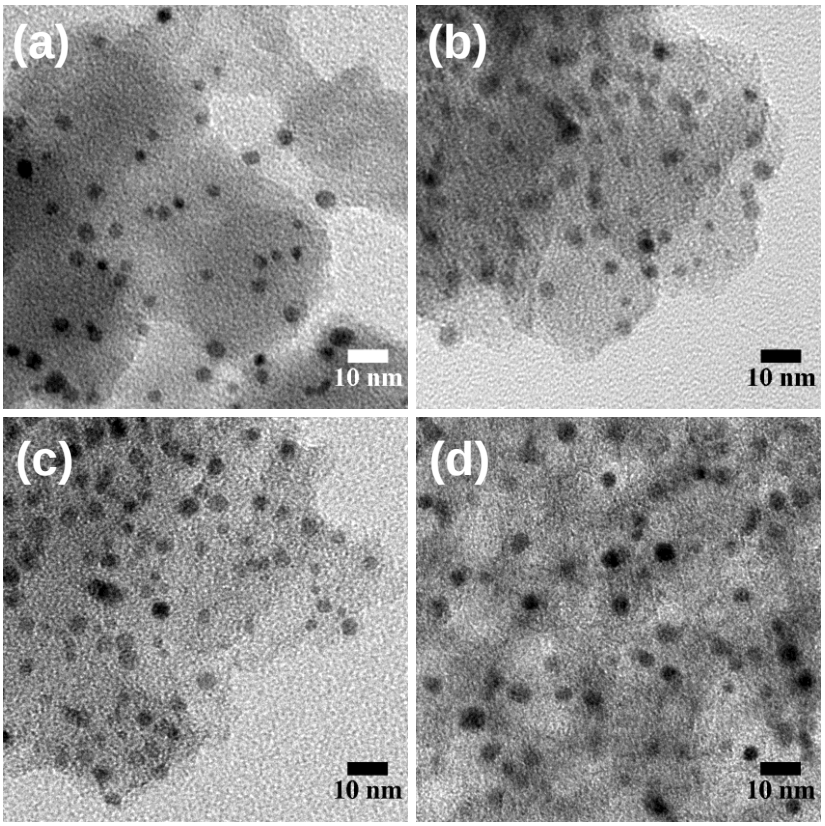

Figure S1 TEM images of (a) Pt-Zn@NC-600, (b) Pt-Zn@NC-700, (c) Pt-Zn@NC-900, (d) Pt-Zn@NC-1000.

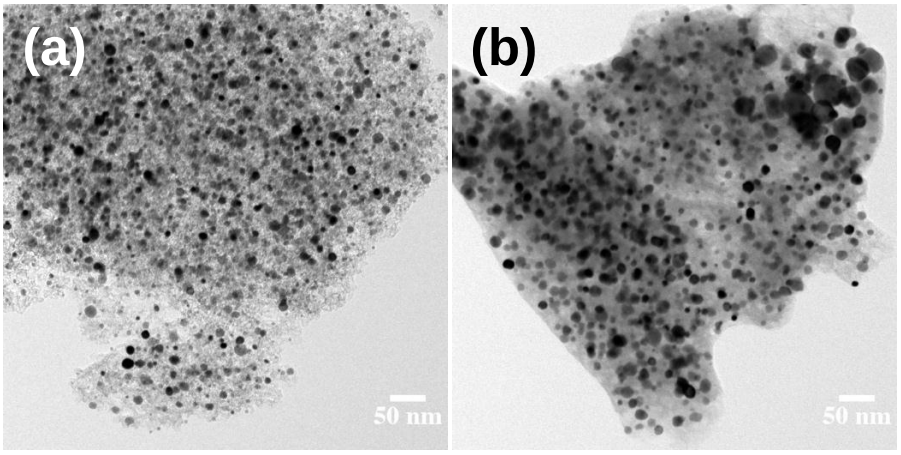

Figure S2 TEM images of (a) Pt-Zn/NC-800, (b) Pt-Zn-IW@NC-800. Severe aggregation was observed in Pt-Zn-IW@NC-800 sample.

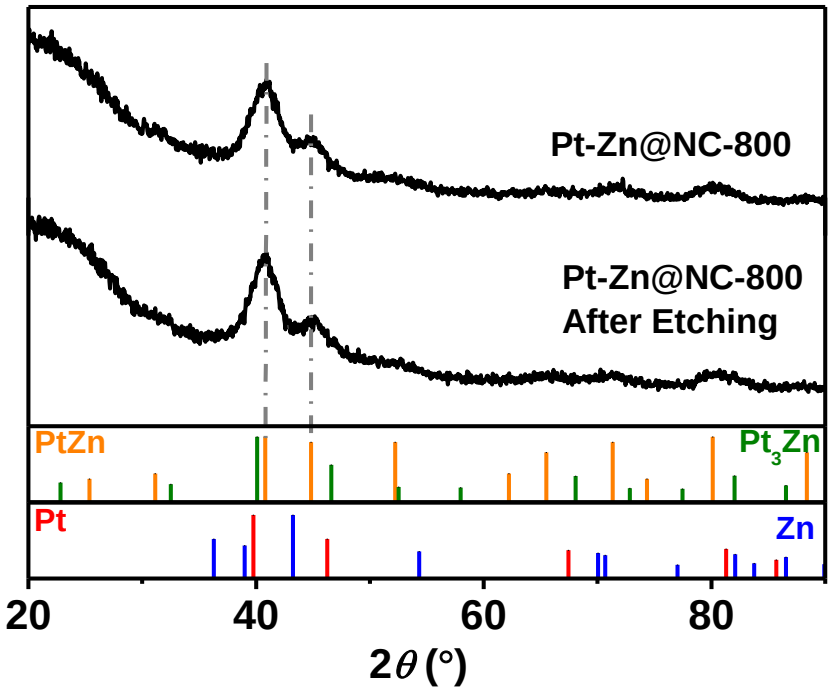

Figure S3 PXRD patterns of Pt-Zn@NC-800 before and after etching by 3 M HCl. The crystal structure was retained after etching.

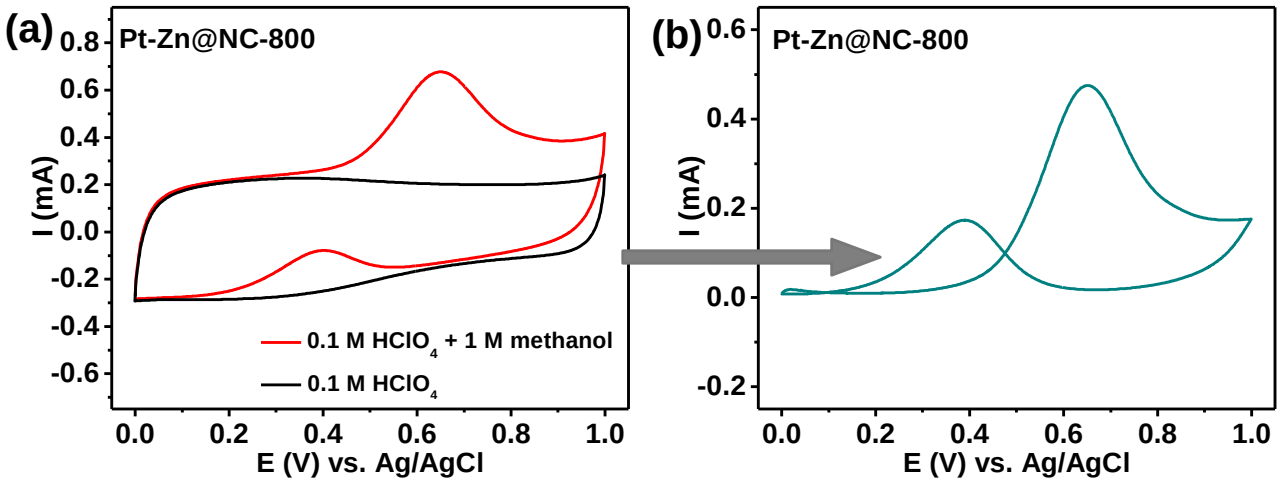

Figure S4 (a) CV curves measured in pure 0.1 M $HClO_4$ (solution1, black curve) and 0.1 M $HClO_4$ + 1 M methanol mixture (solution2, red curve); (b) calculated CV curve by subtraction CV curve of solution1 from that of solution2.

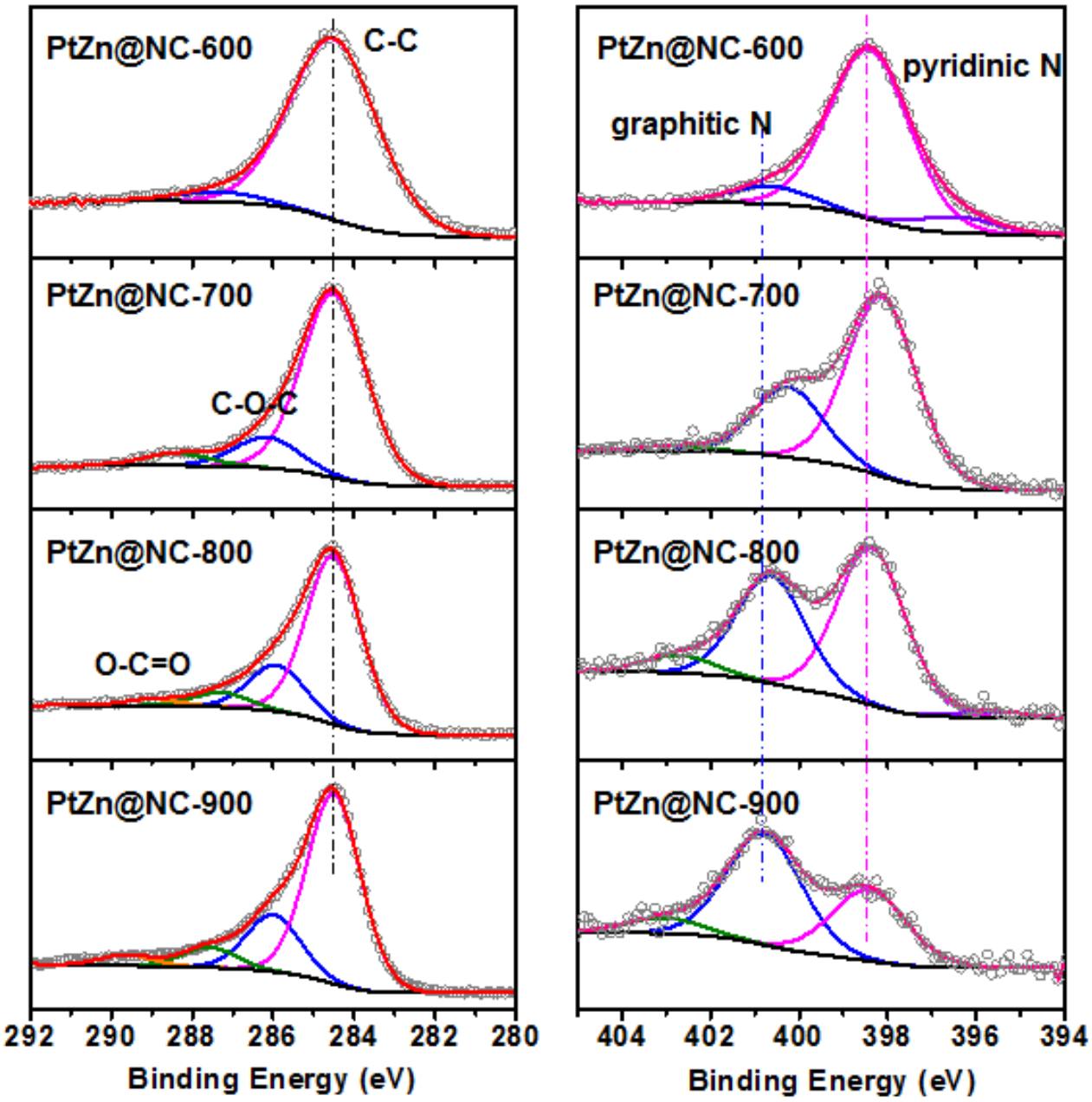

Figure S5 XPS spectra of Pt-Zn@NC-n (n from 600 to 900 ˚C): a) C; b) N. All the peak positions were calibrated by referring to C1s (284.5 eV).

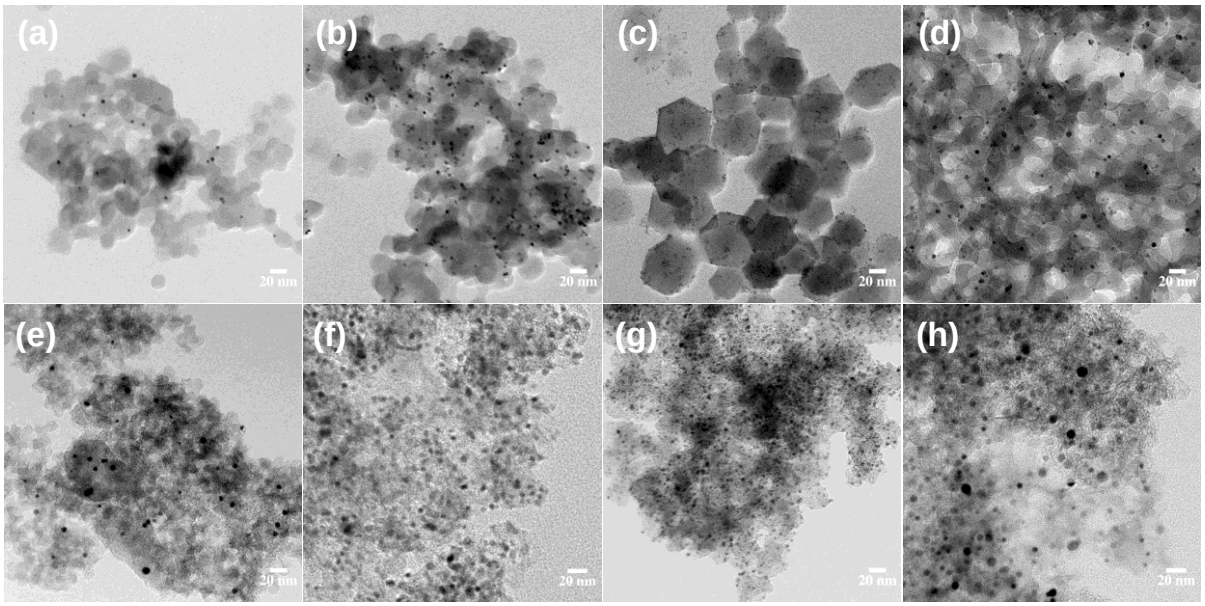

Figure S6 TEM images of M@ZIF-8 particles: (a) Au@ZIF-8; (b) Rh@ZIF-8; (c) Ru@ZIF-8; (d) Pd@ZIF-8 and samples after pyrolysis (e) Au-Zn@NC; (f) Rh-Zn@NC; (g) Ru-Zn@NC and (h) Pd-Zn@NC. Pyrolysis of the ground M@ZIF-8 samples was performed at 800 ˚C in 10% H_2/argon atmosphere.

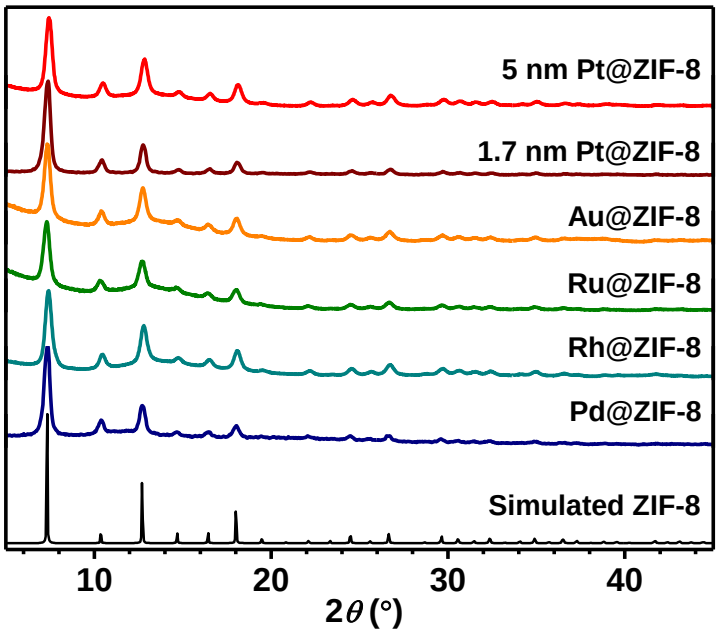

Figure S7 PXRD patterns of M@ZIF-8 samples (M= Ru, Au, Pd, Rh, Pt) and simulated ZIF-8 standard, which are all well aligned.

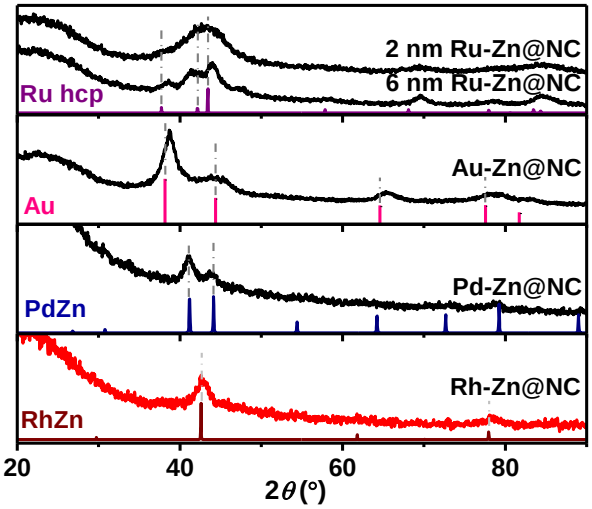

Figure S8 PXRD patterns of M-Zn@NC samples (M= Ru, Au, Pd, Rh) and their corresponding XRD standard patterns. All the as-synthesized M@ZIF-8 samples were carbonized at 800 ˚C under 10% H_2/argon atmosphere.

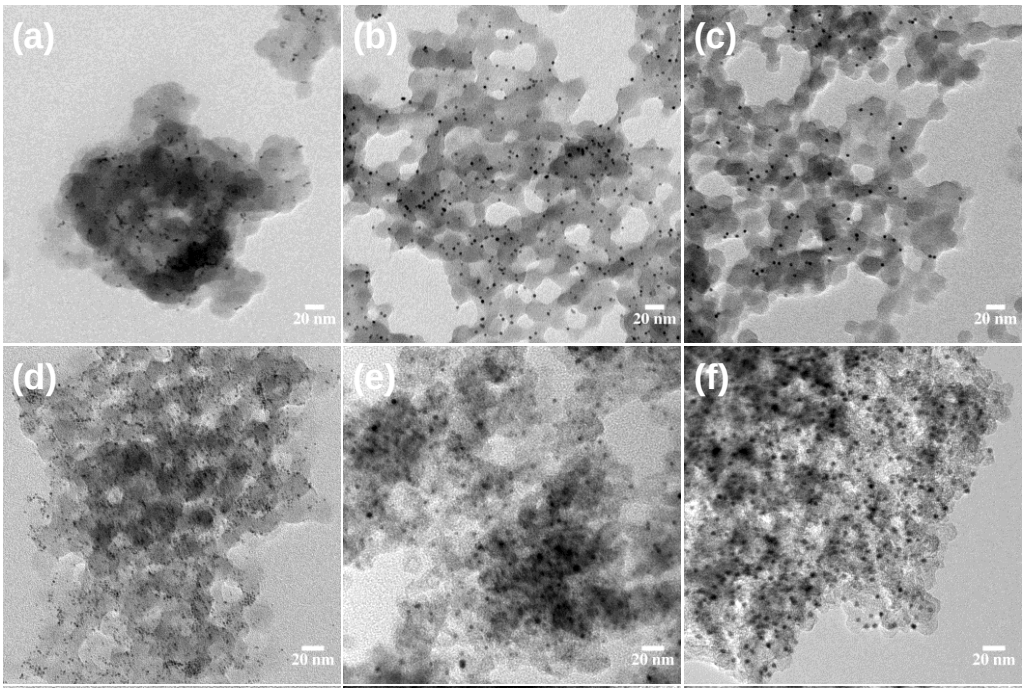

Figure S9 TEM images of PVP-capped Pt@ZIF-8 before (top) and after (bottom) pyrolysis. 1.7 nm Pt (a, d), 2.6 nm Pt (b, e) and 4.3 nm Pt (c, f). Pyrolysis of Pt@ZIF-8 samples was performed at 800 ˚C under 10% H_2/argon atmosphere.

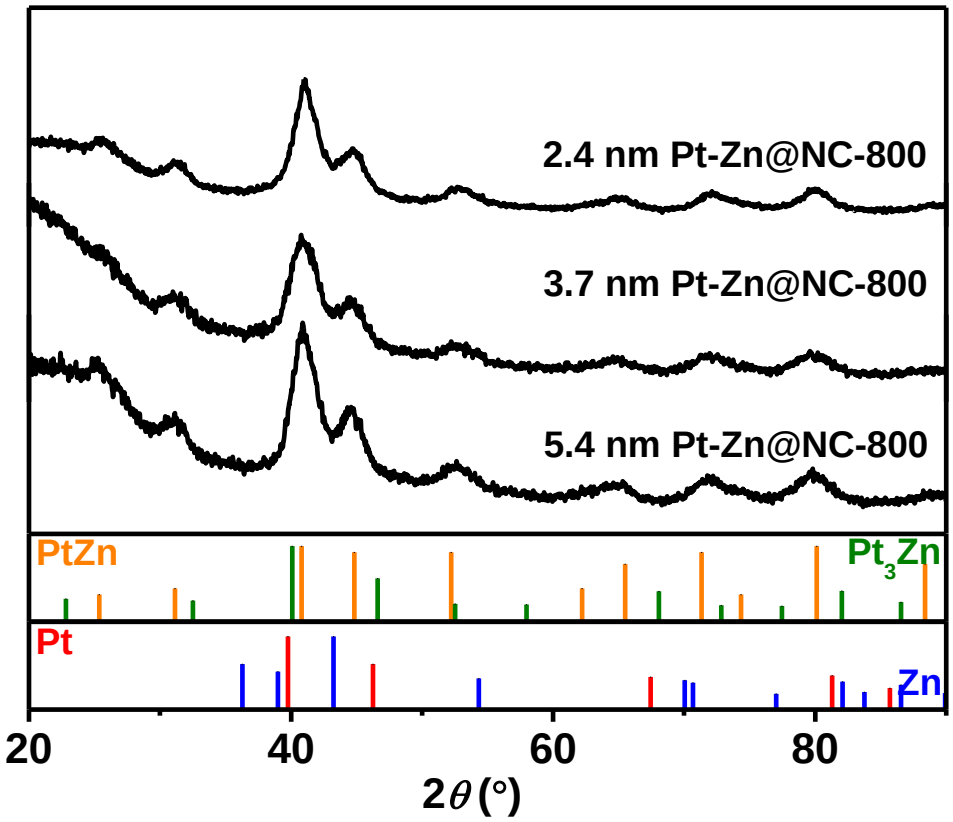

Figure S10 (a) PXRD patterns of Pt-Zn@NC samples. 1.7 nm, 2.6 nm and 4.3 nm PVP-capped Pt NPs were first synthesized and encapsulated inside ZIF-8. All the as-synthesized Pt@ZIF-8 samples were carbonized at 800 ˚C under 10% H_2/argon atmosphere.

Table S1 The lattice distances calculated from the major peaks of Pt-Zn@NC-n in Fig. 2a.

Samples	2θ (°)	d (Å)
Pt-Zn@NC-600	41.158	2.191
Pt-Zn@NC-700	41.004	2.199
Pt-Zn@NC-800	40.899	2.205
PtZn (#06-0604)*	40.796	2.2100
Pt-Zn@NC-900	40.608	2.220
Pt-Zn@NC-1000	40.089	2.247
Pt_3Zn (#65-3257)*	40.084	2.2476

***** The related values of PtZn and Pt_3Zn (111) lattice distances are given from standard PDF card.

Table S2 ICP-MS analysis of Pt-Zn@NC-n synthesized in 10% H_2/Ar atmosphere.

Samples	Weight loss (%)[a]	Pt loading (%)	Zn loading (%)	Zn/Pt
Pt-Zn@NC-600	36.0	4.4	24.7	16.8
Pt-Zn@NC-700	66.4	6.5	11.9	5.1
Pt-Zn@NC-800	79.4	12.4	7.6	1.8
Pt-Zn@NC-900	79.5	12.3	2.2	0.54
Pt-Zn@NC-1000	79.4	9.7	1.4	0.44
Pt-Zn@NC-800 (after etching)	-	12.7	4.9	1.1

[a] Weight loss refers to the mass lost during pyrolysis.

Table S3 Summary of particle sizes of Pt-Zn@NC-n.

Samples	Pt-Zn crystallite size (nm)[a]	average Pt-Zn diameter (nm)[b]	overgrowth ratio in diameter [c]
Pt-Zn@NC-600	3.5 ±0.2	3.6 ±0.5	1.13
Pt-Zn@NC-700	3.6 ±0.2	3.7 ±0.5	1.16
Pt-Zn@NC-800	3.6 ±0.2	3.7 ±0.6	1.16
Pt-Zn@NC-900	3.6 ±0.2	3.8 ±0.6	1.19
Pt-Zn@NC-1000	4.0 ±0.2	3.7 ±0.6	1.31

[a] Crystallite size was calculated by Scherrer's equation from the most intensive diffraction peak around 40-41˚.

[b] Average Pt-Zn diameter was averaged from 200 particles counted in the TEM images.

[c] Theoretical PtZn average particle diameter (3.2 nm) was calculated through the average diameter of Pt (2.6 nm) and densities of Pt (21.37 g/cm^3) and PtZn (15. 28 g/cm^3). Pt_3Zn average particle diameter (2.8 nm) was calculated through the average diameter of Pt (2.6 nm) and densities of Pt (21.37 g/cm^3) and Pt_3Zn (18.31 g/cm^3).

We assume the particles are spherical and use $V=4/3\pi r^3$ to calculate the volume of each particle. To calculate the theoretical diameter of PtZn, we use the equation below

$$\frac{V_{Pt} * D_{Pt}}{M_{Pt}} = \frac{V_{PtZn} * D_{PtZn}}{M_{PtZn}}$$

while V, D, and M represent volume, density, and molar mass.

A similar method was used to calculate the theoretical average diameter of Pt_3Zn.

The overgrowth ratio in diameter was calculated using average Pt-Zn diameter divided by theoretical average particle diameter.

Table S4 XPS analysis of Pt-Zn@NC-n composites.

Samples	N /%	C /%	Pt /%	Zn /%	O /%	Zn/Pt
Pt-Zn@NC-600	23.6	60.1	0.21	9.48	6.69	45.1
Pt-Zn@NC-700	7.86	78.2	0.22	2.43	11.3	11.0
Pt-Zn@NC-800	9.04	84.2	0.47	2.66	3.62	5.66
Pt-Zn@NC-900	3.93	90.9	0.55	0.57	4.00	1.04

N analysis	Pyridinic-N (398.6 ± 0.1 eV) /%	Graphitic-N (400.7 ± 0.2 eV) /%	Oxidized-N (403.0 ± 0.3 eV) /%
Pt-Zn@NC-600	83.2	8.8	-
Pt-Zn@NC-700	68.3	27.2	2.3
Pt-Zn@NC-800	54.1	37.5	6.3
Pt-Zn@NC-900	36.0	56.2	7.8

All the percentage are atomic percent.

Table S5 Summary of BET surface areas, pore sizes and pore volumes

Samples	BET surface area (m^2/g)	Pore diameter[(a)] (nm)	Pore volume[(b)] (cm^3/g)	Micropore volume[(c)] (cm^3/g)
ZIF-8	1550	1.1 &23	0.75	0.47
Pt@ZIF-8	1400	1.1 & 24	0.61	0.46
Pt-Zn@NC-800	990	0.8 & 1.1 & 14	0.74	0.36

(a) Micropore size distribution was calculated by DFT pore size method, and mesopore size distribution was calculated by BJH method.
(b) Cumulative pore volume from BJH adsorption
(c) Micropore volume calculated from T-plot.

Table S6 Summary of particle size of M-Zn@NC-800 composites.

	sample			
	Au-Zn	Rh-Zn	Ru-Zn	Pd-Zn
crystallite size (nm) [a]	4.2 ±0.2	5.7 ±0.7	3.6 ±0.6	5.9 ±0.9
average M-Zn particle diameter (nm) [b]	5.4 ±1.0	5.1 ±0.9	3.0 ±0.7	5.4 ±1.1
average M particle diameter (nm) [b]	3.9 ±0.8	3.3 ±0.6	1.8 ±0.2	3.2 ±1.0
theoretical M-Zn particle size (nm)	4.2 ±0.9	4.1 ±0.8	-	3.9 ±1.2
overgrowth ratio in diameter	1.28	1.24	-	1.38

[a] Crystallite size was calculated by Scherrer's equation from the most intensive diffraction peak around 40-41°.
[b] average M-Zn and M NPs size was averaged from the diameters of 200 particles counted in the TEM images.
[c] Theoretical particle sizes of intermetallic Rh-Zn and Pd-Zn were calculated through density difference of M and M-Zn. Alloy Au-Zn were calculated from the lattice distance read from XRD.

Table S7 Summary of particle size of size-controlled Pt-Zn@NC.

	Pt-Zn@NC		
average Pt particle diameter (nm) [a]	4.3 ±0.3	2.6 ±0.3	1.7 ±0.2
average Pt-Zn particle diameter (nm) [a]	5.3 ±0.7	3.7 ±0.6	2.4 ±0.4
Pt-Zn crystallite size (nm) [b]	4.6 ±0.2	3.6 ±0.2	3.0 ±0.2
theoretical Pt-Zn particle size (nm) [c]	5.2 ±0.4	3.2 ±0.4	2.0 ±0.2
overgrowth ratio in diameter	1.02	1.15	1.20

[a] Average Pt-Zn and Pt NPs size was averaged from the diameters of 200 particles counted in the TEM images.

[b] Crystallite size was calculated by Scherrer's equation from the most intensive diffraction peak around 40-41°.

[c] Theoretical particle sizes of intermetallic PtZn were calculated through density difference of Pt and PtZn.

Table S8 Literature summary of sizes of reported intermetallic nanoparticles.

Samples	Temperature (˚C)	Synthetic method	Size (nm)	Ref.
Pt-Zn@NC	800	Pyrolysis in H_2	2.4 ± 0.4	This work
PtZn/CNT@mSiO_2	600	Thermal annealing	3.2 ± 0.4	[S1]
PtZn/SiO_2	600	WI, H_2 reduction	2-7	[S2]
Pt–M/SiO_2 (M = Fe, Co, Ni, Cu, Ga)	600, 800, 900		4-6[a], 12	
PdZn/ZnO	400	WI, H_2 reduction	3-15	[S3]
$Pd_{13}Pb_9/SiO_2$	800	WI, H_2 reduction	13	[S4]
Pd−M/SiO_2 (M = Cu, Ga, Zn)	500, 600, 1000		4-8[a]	
Rh−M′/ SiO_2 (M′ = Fe, Ni, Pb, Sb, Sn, Ti)				
PtPb NPs	28-35	microemulsions, $NaBH_4$ reduction	3.0–5.4	[S5]
PtFe/C	700	Thermal annealing	~6.5	[S6]
PtPb-OMCS	700	Thermal annealing	11.9, 13.1	[S7]
Pt_3Cr	600	Anneal, KCl matrix	~5	[S8]
PtFe/C	900	Thermal annealing	3.6	[S9]

[a] Particle size is referred to the crystallite size calculated from XRD via Scherrer's equation.

References

[S1]. Qi, Z. Y.; Xiao, C. X.; Liu, C.; Goh, T. W.; Zhou, L.; Maligal-Ganesh, R.; Pei, Y. C.; Li, X. L.; Curtiss, L. A.; Huang, W. Y. *J. Am. Chem. Soc.* **2017,** *139* (13), 4762-4768.

[S2]. Iihama, S.; Furukawa, S.; Komatsu, T. *ACS Catal.* **2016,** *6* (2), 742-746.

[S3]. Zhou, H. R.; Yang, X. F.; Li, L.; Liu, X. Y.; Huang, Y. Q.; Pan, X. L.; Wang, A. Q.; Li, J.; Zhang, T. *ACS Catal.* **2016,** *6* (2), 1054-1061.

[S4]. Furukawa, S.; Yoshida, Y.; Komatsu, T. *ACS Catal.* **2014,** *4* (5), 1441-1450.

[S5]. Magno, L. M.; Sigle, W.; van Aken, P. A.; Angelescu, D.; Stubenrauch, C. *Phys Chem Chem Phys* **2011,** *13* (20), 9134-9136.

[S6]. Chung, D. Y.; Jun, S. W.; Yoon, G.; Kwon, S. G.; Shin, D. Y.; Seo, P.; Yoo, J. M.; Shin, H.; Chung, Y. H.; Kim, H.; Mun, B. S.; Lee, K. S.; Lee, N. S.; Yoo, S. J.; Lim, D. H.; Kang, K.; Sung, Y. E.; Hyeon, T. *J. Am. Chem. Soc.* **2015,** *137* (49), 15478-15485.

[S7]. Shim, J.; Lee, J.; Ye, Y.; Hwang, J.; Kim, S. K.; Lim, T. H.; Wiesner, U.; Lee, J. *ACS Nano* **2012,** *6* (8), 6870-6881.

[S8]. Cui, Z. M.; Chen, H.; Zhou, W. D.; Zhao, M. T.; DiSalvo, F. J. *Chem. Mater.* **2015,** *27* (21), 7538-7545.

[S9]. Du, X. X.; He, Y.; Wang, X. X.; Wang, J. N. *Energ. Environ. Sci.* **2016,** *9* (8), 2623-2632.

CHAPTER 4. TWO DIMENSIONAL ULTRATHIN TI3C2 MXENE NANOSHEET SUPPORTED PT3TI INTERMETALLIC NANOPARTICLES FOR ENHANCED HYDROGEN EVOLUTION REACTION

A paper to be submitted, collaborated with Prof. Yue Wu and Zhe Li

Zhiyuan Qi[†,‡], Zhe Li, [§] Yue Wu, [*,§] and Wenyu Huang, [*,†,‡]

[†]Department of Chemistry, Iowa State University, Ames, Iowa, 50011, United States

[‡]The Ames Laboratory, Ames, IA, 50011, United States

[§]Department of Chemical and Biological Engineering, Iowa State University, Ames, Iowa, 50011, United States

4.1 Abstract

Design an efficient catalyst for hydrogen evolution reaction (HER) is urgently needed for its practical application. Pt_3Ti intermetallic nanoparticles (iNPs) supported by two-dimensional Ti_3C_2 MXene is synthesized via facial high-temperature annealing of MXene loaded with dispersed Pt precursors. Due to a synergistic effect between Pt_3Ti iNPs and the MXene support, the catalyst exhibits superior HER performance in acid condition with an overpotential of 33.8 mV and Tafel slope of 38.3 $mVdec^{-1}$. To the best of our knowledge, this work represents the first example of Ti_3C_2 MXene working as both support and second metal precursor in the synthesis of iNPs and demonstrates its great potential in electrocatalysis.

4.2 Introduction

Hydrogen evolution reaction (HER) serves as a critical link between renewable energy sources and energy conversion applications such as hydrogen fuel cells.[1] To minimize the required overpotential of HER, considerable research efforts have been devoted to rationally design

efficient electrocatalysts with low cost in the past decades, including transition metal sulfides, phosphides, carbides, and nitrides.[2-7] However, there's no denying that platinum (Pt) is still the most efficient HER catalyst but its widespread application is significantly limited by the high cost.[8] To fulfill the cost-effective utilization of Pt, either reducing the particle size to increase the number of active sites or tuning the electronic structures through alloying to improve the activity of each site have been practiced.[1,9-14] For example, 3.2 nm PtZn intermetallic nanoparticles have shown the enhancement of both mass activity and specific activity towards methanol oxidation reaction (MOR) compared to larger PtZn and commercial Pt catalyst.[10] Therefore, Pt-based alloys and intermetallics with small sizes are promising candidates for electrochemical applications.

Ti_3C_2 is a representative composition of the emerging family of MXenes, which are generally produced via selective etching away the "A" elements from MAX phase (formulated as $M_{n+1}AX_n$ (n = 1,2,3) to form two dimensional graphene-like structures.[15] The MXenes have a general formula as $M_{n+1}X_nT_x$ where M represents the early transition metals (e.g., Ti, Nb, V, Mo), X is carbon and/or nitrogen, and T_x represents the surface termination (e.g., fluorine, hydroxyl, oxygen) dependent on the etching method. [16] To simplify, we use Ti_3C_2 in this paper while F and/or OH actually exist on the surface. As the first MXene reported in 2011,[17] Ti_3C_2 gains the major research focus due to its well-established etching conditions and numerous investigation of its electronic, dielectric, magnetic, optical, chemical stability, electrochemical and catalytic properties.[15,17-20] Because of its metallic conductivity, layered structure, small band gaps and hydrophilic nature, Ti_3C_2 is also intensively studied for electrochemical energy storage application, such as supercapacitors,[21] rechargeable batteries.[22-23] However, few experimental studies have been reported so far for its applications in electrocatalysis.

Herein, we report a facial synthesis of Pt_3Ti nanoparticles (NPs) supported on Ti_3C_2 MXene by simply annealing the Ti_3C_2 supported Pt precursors at high temperatures. The catalysts demonstrate the superior HER performance in terms of smaller overpotential, lower Tafel slope, excellent stability and higher mass activity compared to commercial platinum/carbon (Pt/C) catalysts. Furthermore, the cause of enhanced HER was investigated via carefully designed control experiments and was found to be the synergistic effect between Ti_3C_2 support and Pt_3Ti iNPs. To the best of our knowledge, it is the first attempt that demonstrates Mxene as a second metal source in the synthesis of intermetallic and its potential in electrocatalysis.

4.3 Experimental Section

4.3.1 Synthesis of bulk Ti_3AlC_2 and Ti_3C_2 MXene nanosheets

The Synthesis of bulk Ti_3AlC_2 vis hot pressing was carried out by Zhe Li in Prof. Yue Wu's lab. The as-synthesize Ti_3AlC_2 bulk was ground and etched by boiled HF to form Ti_3C_2 Mxenes nanosheets.[17]

4.3.2 Synthesis of series of Pt/Ti_3C_2

For a typical synthesis, 50 mg of as-synthesized Ti_3C_2 MXene powder was immersed by 25 μL of $Pt(NH_3)_4(NO_3)_2$ aqueous solution (0.02 g Pt/mL). The mixture was vacuum dried and ground to ensure the homogeneity, labeled as 1 wt.% Pt/Ti_3C_2. The powder was then transferred into a tube furnace and reduced at different temperatures for 30 min under 3% H_2/Ar flow with a ramping rate of 5 ˚C/min to obtained Pt/Ti_3C_2-*n* (*n* indicates the applied reduction temperature).

4.3.3 Synthesis of Pt_3Ti/Vulcan control samples

20% Pt_3Ti/Vulcan was synthesized by first thoroughly grinding the commercial 20% Pt/Vulcan catalyst and TiH_2 solid mixture (Pt: Ti = 3:1). 2% Pt_3Ti/Vulcan was synthesized by

thoroughly grinding K_2PtCl_4, TiH_2, and Vulcan XC-72 carbon solid mixture (Pt: Ti = 3:1). Both samples were reduced at 700 ˚C for 4 h under 10% H_2/Ar with a ramping rate of 5 ˚C/min.

4.3.4 Characterizations

The mass loading of Pt was determined by using a Thermo Fisher Scientific X Series 2 inductively coupled plasma mass spectroscopy (ICP-MS). All the Pt-containing samples were digested in the boiling aqua regia solution, and the clear top layers were used for further analysis. X-ray diffraction (XRD) patterns were recorded at room temperature by a Bruker diffractometer with Cu K_α radiation source (λ=1.5406 Å). Transmission electron microscopy (TEM) images were recorded using a TECNAI G2 F20 electron microscope operated at 200 kV. High-resolution high angle annular dark field (HAADF) scanning transmission electron microscopy (STEM) imaging was acquired on a Titan Themis 300 probe corrected TEM with a Super-X EDX detector in the Sensitive Instrument Facility of Ames Lab. Extended X-ray absorption fine structure (EXAFS) measurement were performed in Argonne National Lab.

4.3.5 Electrochemical Measurements

All the electrochemical measurements were carried out in a three-electrode system using an electrochemical station (VSP-300, Bio-Logic Science Instruments). Typically, 10 mg of catalysts were dispersed in 100 μL of the mixture solution (water: isopropanol: Nafion solution (5 wt%) = 45: 45: 10) by sonication for 30 min to obtain a homogeneous ink. 20 μL of the above catalyst ink was then transferred onto 1 cm^2 area on a carbon fiber electrode (Toray Paper 030) and dried at room temperature in air. HER was conducted in a home-made H-cell with two counterparts isolated by a Nafion-115 film, utilizing carbon fiber electrode with loaded catalysts as a working electrode, Ag/AgCl (saturated KCl) as a reference electrode, and a Pt gauze as the counter electrode. In a typical measurement, the Pt gauze counter electrode was placed in one

counterpart while working electrode and reference electrode were placed in the other counterpart containing the electrolyte saturated with H_2. Both 0.1 M $HClO_4$ and 0.1 M KOH aqueous solution were used as the electrolyte. All the water used in electrochemistry study is the Millipore water (18.2 MΩ cm).

4.4 Results and Discussion

The details of synthesizing the pristine Ti_3C_2 MXene will not be discussed in this dissertation, as this part of work was solely contributed by Zhe Li from Prof. Yue Wu's group. In general, the bulk Ti_3AlC_2 synthesized via hot pressing method was exfoliated via HF etching to remove the aluminum (Al) layers and followed by sonication to obtain the two-dimensional Ti_3C_2 MXene with OH and/or F functional group terminated on the surface, as illustrated in Figure 1a. The PXRD pattern of the as-synthesized MXene has no diffraction peaks from the bulk Ti_3AlC_2 but matches well with the simulate Ti_3C_2 patterns,[17] indicating the successful exfoliation and the formation of Ti_3C_2 (Figure 1b). The morphology of Ti_3C_2 MXene was further analyzed by both scanning electron microscopy (SEM) and transmission electron microscopy (TEM). The SEM image in Figure 1c shows a nano-accordion multilayer structure of Ti_3C_2 Mxene and one thin layer of Ti_3C_2 Mxene was observed by TEM (The lacey background is from the TEM grid). The XPS and elemental mapping results show the amount of Al was negligible and Ti was partially oxidized once exposed to air (The XPS and elemental mapping raw date will not be presented in this dissertation).

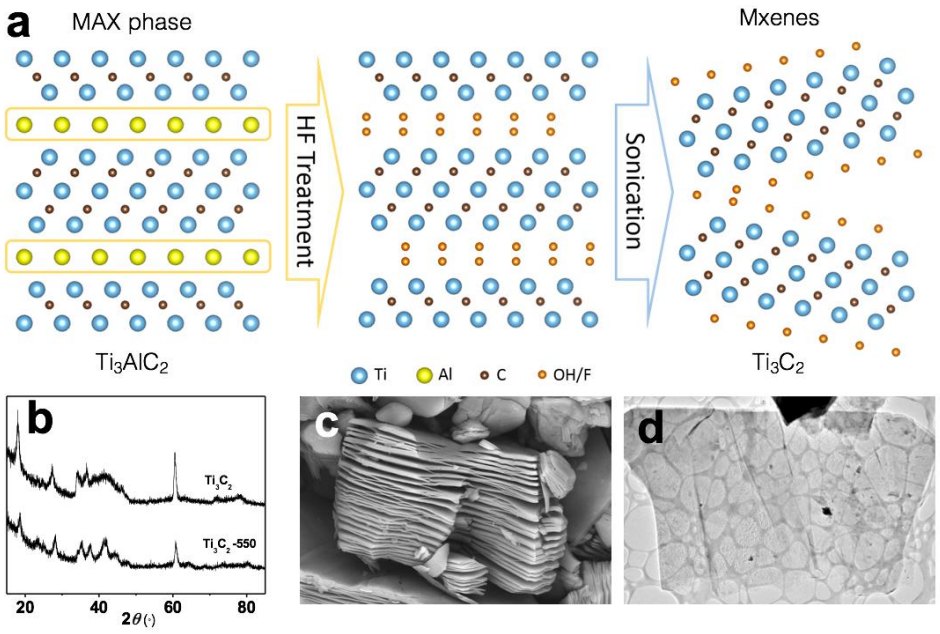

Figure 1 (a) The schematic representation of the synthesis of Ti_3C_2 MXene via HF etching and sonication, (b) The XRD patterns of the pristine Ti_3C_2 MXene and Ti_3C_2 after 550 ˚C annealing, (c) SEM image and (d) TEM image of Ti_3C_2 Mxene.

With the careful characterization of the Ti_3C_2 MXene, Pt precursors were deposited onto the Ti_3C_2 MXene via wetness impregnation. To investigate the effect of annealing temperature on the formation of Pt-Ti alloys and the resultant electrochemical activities, the as-synthesized Pt/ Ti_3C_2 was annealed at 4 different temperatures (200, 400, 550, and 700 ˚C) under 3% H_2/Ar atmosphere. The exact loading was confirmed by ICP-MS, summarized in Table 1. It is noted that higher temperature leads to more weight loss, which is due to the decomposition of Ti_3C_2. Pt/Ti_3C_2-700 has the highest Pt loading of 1.2 wt% due to the largest weight loss. We could not determine the Pt/Ti ratio in nanoparticles by ICP-MS, because of a large amount of Ti in the Mxene support.

Table 1. Pt loading and weight loss of Pt/Ti_3C_2 at different annealing temperatures.

Entry	Temperature (°C)	Weight loss (%)	Pt loading (%)
pristine	-	-	0.9
1	200	1.6	0.9
2	400	3.9	1.0
3	550	8.8	1.0
4	700	12.7	1.2

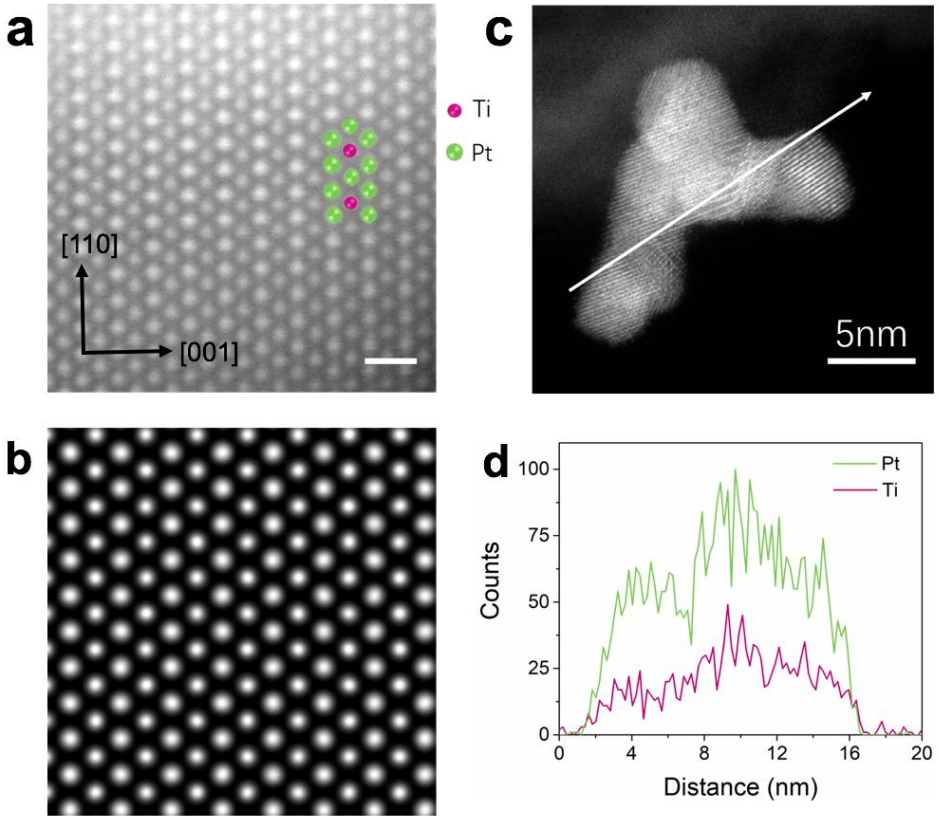

Figure 2. (a, b) High-resolution HAADF-STEM image and simulated HRTEM images of Pt_3Ti ordered structures. The green and pink spheres were presenting Pt and Ti atoms respectively. The scale bar is 0.5 nm (c, d) HAADF-STEM image of several particles on edge without underbeneathTi_3C_2 support and corresponding EELS line scan profiles. scale bar: 5 nm.

Table 2 Quantitative information of the XANES data and EXAFS fits

Sample	Edge Energy (keV)	Scattering Pair	S_0^2	CN #	r (Å) #	ΔE_0 (eV) #	σ^2 (Å ^{2}) #
Pt Foil	11.5640	Pt-Pt	0.77	12	2.76	7.7	0.004
2% Pt/SiO_2	11.5640	Pt-Pt	0.77 *	8.6	2.74	7.1	0.006
Pt/Ti_3C_2 200 ˚C	11.5653	Pt-N	0.77 *	4.1	2.06	7.7	0.003
Pt /Ti_3C_2 400 ˚C	11.5640	Pt-Pt	0.77 *	8.8	2.75	4.6	0.006
Pt/Ti_3C_2 550 ˚C	11.5646	Pt-Pt	0.77 *	6.6	2.75	6.8	0.006
		Pt-Ti		3.4	2.75		0.015
Pt /Ti_3C_2 700 ˚C	11.5648	Pt-Pt	0.77 *	7.2	2.75	5.9	0.006
		Pt-Ti		4.1	2.74		0.015

* The S_0^2 is fixed at the value obtained by fitting a Pt foil reference.

The error of all the fitted parameters are very close. The average error in CN (coordination number) is 0.5, in r (bond length) is 0.003 Å, in ΔE_0 (energy shift) is 0.5 eV and in σ^2 (Debye-Waller factor) is 0.001 Å^2.

With the broad XRD diffraction peaks between 2θ = 35-50˚ from F or OH-terminated Ti_3C_2, the diffraction peaks of Pt or Pt_3Ti is hard to distinguish due to the low metal loading (1 wt% Pt or Pt_3Ti) and the small particle size. Therefore, we used the high resolution HAADF-STEM to study the ordering of the resultant Pt_3Ti nanoparticles. An ordered Pt_3Ti{110} facet with two alternating columns was observed as shown in Figure 2a, where brighter columns consist of all Pt atoms and the darker columns alternate Pt atoms (green spheres) and Ti atoms (pink spheres). The lattice distances 0.28 nm and 0.39 nm match well with the theoretical lattice spacing along [110] and [001] directions of intermetallic Pt_3Ti. Besides, the measured TEM images are in good

agreement of the simulated $Pt_3Ti\{110\}$ crystal plane, which further confirms the formation of ordered intermetallic Pt_3Ti phase with definite composition and atomic arrangement. The homogeneity of Pt_3Ti particles was confirmed by EELS line scan measurement, as shown in Figure 1c-d. For the analyzed assembly of several close particles with average size of 5 nm, the Pt and Ti signals are evenly distributed across the particles and no core-shell structure or phase separation was observed.

As has been mentioned above, the PXRD is not able to represent the crystal structures of Pt or Pt_3Ti clearly in the presence of Ti_3C_2 support. Meanwhile, the TEM could only show some representative images of particles. Therefore, we use EXAFS to analyze the overall chemical environment of the catalysts annealed at different temperatures. The fitting results of 1 wt% Pt/Ti_3C_2 *in-situ* annealed at different temperatures with two references of Pt foil and 2 wt% Pt/SiO_2 were summarized in Table 2. Pt is not reduced at 200 ˚C but remains as the precursor $Pt(NH_3)_4^{2+}$ and dispersed on the support, showing 4 Pt-N bonds at 2.06 Å. Formation of Pt nanoparticles was clearly observed in Pt /Ti_3C_2-400 with an average Pt-Pt bond length of 2.75 Å and a coordination number (CN) of 8.8, which is similar to the 2 wt% Pt/SiO_2 reference. Although EXAFS fitting does not show a significant amount of Pt-Ti scattering in Pt /Ti_3C_2-400, it is still possible a small portion of Ti alloyed with Pt NPs. Increasing the annealing temperature to 550 ˚C leads to the formation of Pt_3Ti NPs, whose average Pt-Pt CN (6.6) is about twice than that of Pt-Ti CN (3.4). Annealing the sample at 700 ˚C results in further Ti enrichment in the NPs. The Pt-Pt and Pt-Ti CNs increase to 7.2 and 4.0, respectively, with minor changes in bond distances (Table 2). Notably, the total CN (Pt-Pt +Pt-Ti) increases with higher annealing temperature, indicating an increase in average particle size.

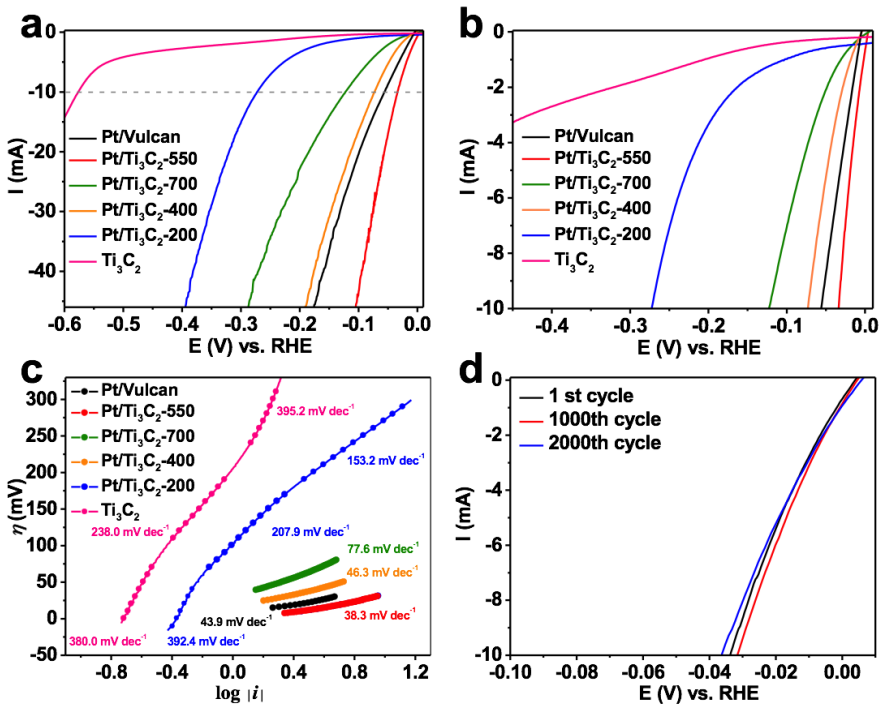

Figure 3. (a) HER polarization curves at 2 mV s^{-1} in H_2 saturated 0.1 M $HClO_4$; (b) is the zoom-in region of 0 ~ 10 mA; (c) Tafel curves calculated by η = b log|i| +a; (d) HER curves before and after stability tests.

Table 3 HER catalyzed by different Pt-Ti/MXene catalysts.

	Pt wt%	m_{Pt} (μg)	η@10 mA (mV)	η@40 mA (mV)
Pt/Vulcan	20.0	22.0	55.8	159
Pt/Ti_3C_2-550	1.0	21.9	33.8	95.2
Pt /Ti_3C_2-700	1.2	30.7	122	269
Pt /Ti_3C_2-400	1.0	20.4	73.5	176
Pt /Ti_3C_2-200	0.89	21.1	272	381
Ti_3C_2	-		576	-

With the nature of the catalysts were confirmed by the standard characterization, we thus study the HER performance of Pt/Ti_3C_2-*n* via using a three-electrode system with Pt counter electrode separated in another counterpart to avoid Pt contamination. All the potentials are automatically *i*-R corrected by the potentiostat. It is noteworthy that the different annealing temperatures lead to quite different activities. As shown in Figure 3, all the Pt/Ti_3C_2 catalysts have enhanced HER activities compared to the bare Ti_3C_2 support that has a large overpotential at 10 mA (η_{10mA}) of 576 mV. Pt/Ti_3C_2-550 has the smallest overpotential η at both 10 mA and 40 mA, followed by Pt/Ti_3C_2-400, 700 and 200 samples (as summarized in Table 3). As Pt is not reduced at 200 ˚C, a higher η_{10mA} of 272 mV was observed in Pt/Ti_3C_2-200. The lower HER activity of Pt/Ti_3C_2-400 is probably due to the less incorporation of Ti. The larger particle size and a higher degree of support decomposition explain the further drop in HER activity of Pt/Ti_3C_2-700. Remarkably, η_{10mA} of Pt/Ti_3C_2-550 is even 20 mV lower than that of the commercial Pt/Vulcan catalyst with the same applied amount of Pt. The superior activity of Pt/Ti_3C_2-550 is presumably due to the formation of ordered Pt_3Ti and the strong interaction between the nanoparticles and the support. As shown in Figure 3c, Pt/Ti_3C_2-550 has the lowest Tafel slope as 38.3 mV/dec in the range of ~1-10 mA, which suggests the best HER kinetic among all the tested catalysts. A lower Tafel slope suggests a more rapid increase in HER rate with a smaller overpotential, which is beneficial in the real application. The stability of Pt/Ti_3C_2-550 was tested via accelerating stability test (AST) by sweeping the potential between -0.2 V and 0.1 V. The HER activity after 1000 cycles and 2000 cycles AST was compared with the original HER polarization curve (Figure 3d). Interestingly, after 1000th cycle, the η_{10mA} even decreased by 2.3 mV, and only 2.5 mV increase was observed in the 2000th cycle. Overall, Pt/Ti_3C_2-550 is a superior HER catalyst with enhanced activity and great durability.

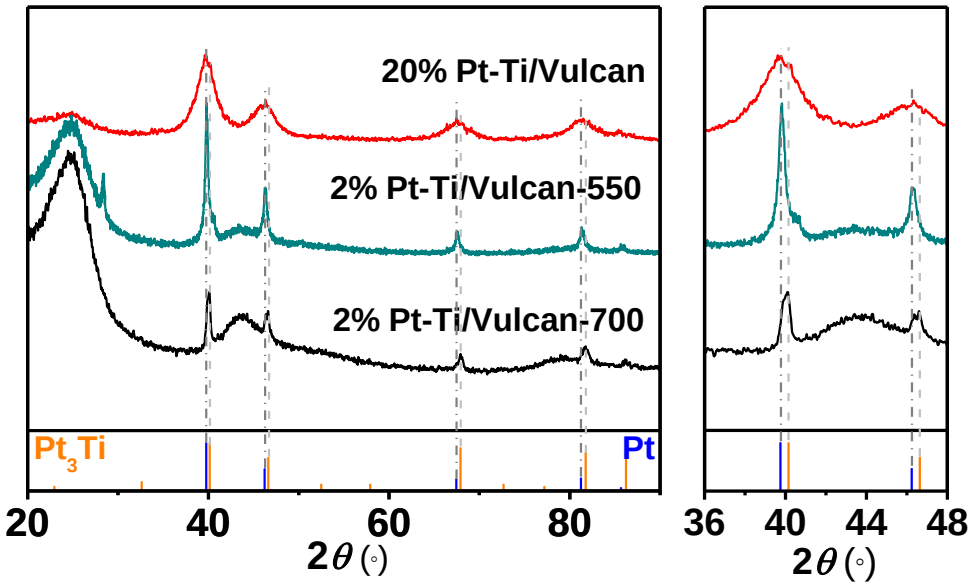

Figure 4. XRD patterns of control samples: 20% Pt-Ti/Vulcan, 2% Pt-Ti/Vulcan-550 and 700.

To investigate the support effect on the synthesis, we synthesized 2% Pt_3Ti/Vulcan by annealing solid mixture of Vulcan carbon, Pt and Ti precursors at 700 ˚C. Figure 4 shows the successful formation of Pt_3Ti with a crystallite size of 21 nm, as calculated by Scherrer equation. However, the PXRD pattern of 2% Pt-Ti/Vulcan-550 matches with the Pt standard, suggesting 550 ˚C is not sufficient for the formation of Pt_3Ti when using Vulcan as support and starting from precursors. The conversion from Pt to Pt_3Ti is not achieved by annealing the mixture of Ti precursor and 20% Pt/Vulcan which already has formed Pt NPs at 700 ˚C. It is clearly demonstrated the benefit of using Ti_3C_2 MXene as the Ti source for the synthesis of Pt_3Ti, not only lower the intermetallic transition temperature, but also constrain the particle size.

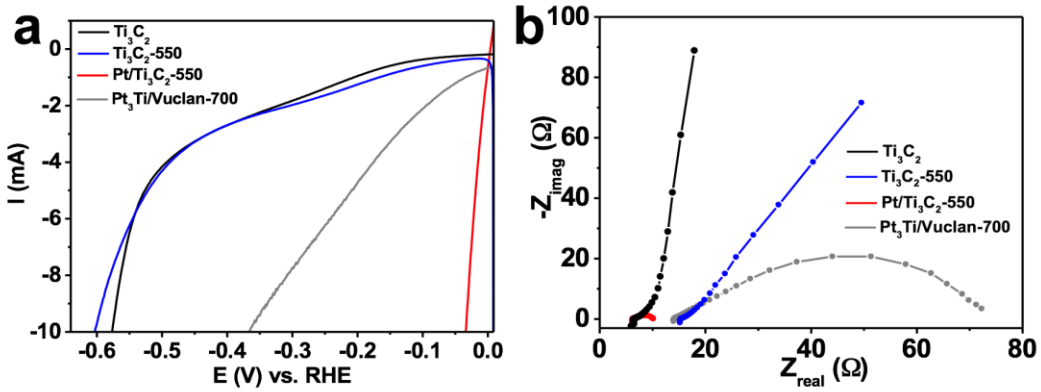

Figure 5. (a) HER polarization curves and (b) Nyquist plot of Pt/Ti_3C_2-550, Ti_3C_2 and two control samples Ti_3C_2-550 and 2% Pt_3Ti/Vulcan-700.

The MXene support also plays an important role in HER activity. We compared the HER performance of annealed support Ti_3C_2-550, as-prepared support Ti_3C_2, Pt_3Ti/Vulcan with of Pt/Ti_3C_2-550. As shown in Figure 5a, the HER overpotential η_{10mA} of Ti_3C_2 support slightly increases after 550 ˚C annealing, which might occur due to the minor decomposition. The activity of Pt/Ti_3C_2-550 is much better than that of 2% Pt_3Ti/Vulcan-700 by a ~350 mV shift in η_{10mA}, as the Pt_3Ti nanoparticles (~ 5 nm) supported on Ti_3C_2 is ~4 times smaller than Vulcan supported nanoparticles. We have demonstrated the great enhancement of both mass activity and specific activity with the smaller PtZn nanoparticles,[10] and we believe the size effect also improves the activity of Pt_3Ti nanoparticle. The Nyquist plot in Figure 5b suggests that Pt/Ti_3C_2-550 has the lowest impedance among the compared catalysts. Both support Ti_3C_2 and Ti_3C_2-550 are mass-transfer limited at low-frequency range while only charge transfer dominates in the presence of Pt_3Ti. The mass transfer resistance of Pt/Ti_3C_2-550 is much smaller than that of Pt_3Ti/Vulcan-700, indicating a good conductivity of Ti_3C_2 and the stronger interaction between the Pt_3Ti and MXene support. Therefore, we could conclude the HER enhancement of Pt/Ti_3C_2-550 is due to the synergistic effect between the Pt_3Ti and Ti_3C_2 support.

4.5 Conclusion

In conclusion, we have for the first time developed a novel intermetallic electrocatalyst synthesized directly using Ti_3C_2 Mxenes as both the conductive support and the second metal precursors. The resultant Pt_3Ti nanoparticles were readily formed at 550 ˚C, and the ordered Pt_3Ti structure was confirmed by both atomic resolution HADDF-STEM and EXAFS. Compared to the catalysts prepared at other temperatures (200, 400, 700 ˚C), Pt/Ti_3C_2 -550 gave the best catalytic performance towards HER with the onset potential of 33.8 mV, Tafel slope of 38.3 V/dec and smallest charge transfer resistance. More importantly, Pt/Ti_3C_2 -550 also has lower overpotential than the commercial 20% Pt/Vulcan with the same Pt loading, indicating that HER activity was enhanced via alloying Pt with Ti. Furthermore, the catalyst is also very stable in acidic solution and no significant activity loss after 2000 cycles. In compassion, we found that 550 ˚C is not sufficient for the formation of ordered Pt_3Ti when using Vulcan carbon as support and Pt_3Ti with a large particle size of 21 nm can be formed until 700 ˚C. This further proves the benefit of our designed synthetic method, which not only lowers the required temperature but also results in small particles. Besides, the control experiments demonstrate that the improvement of activity is not raised by high-temperature annealing of Ti_3C_2 support or the formation of Pt_3Ti alone but instead the interaction between ordered Pt_3Ti and the Ti_3C_2 support. This work demonstrates the first attempt to use MXene in the synthesis of intermetallic and its potential application in electrocatalysis. Future work on exploring the pH-dependent HER activity and mechanism study by DFT calculation and is currently underway.

4.6 Reference

1. Seh, Z. W.; Kibsgaard, J.; Dickens, C. F.; Chorkendorff, I.; Nørskov, J. K.; Jaramillo, T. F. *Science* **2017,** *355* (6321).

2. Vesborg, P. C. K.; Seger, B.; Chorkendorff, I. *The Journal of Physical Chemistry Letters* **2015,** *6* (6), 951-957.

3. Vij, V.; Sultan, S.; Harzandi, A. M.; Meena, A.; Tiwari, J. N.; Lee, W.-G.; Yoon, T.; Kim, K. S. *ACS Catalysis* **2017,** *7* (10), 7196-7225.

4. Zhuo, J.; Cabán-Acevedo, M.; Liang, H.; Samad, L.; Ding, Q.; Fu, Y.; Li, M.; Jin, S. *ACS Catalysis* **2015,** *5* (11), 6355-6361.

5. Li, Y.; Wang, H.; Xie, L.; Liang, Y.; Hong, G.; Dai, H. *Journal of the American Chemical Society* **2011,** *133* (19), 7296-7299.

6. Chen, W.-F.; Sasaki, K.; Ma, C.; Frenkel, A. I.; Marinkovic, N.; Muckerman, J. T.; Zhu, Y.; Adzic, R. R. *Angewandte Chemie International Edition* **2012,** *51* (25), 6131-6135.

7. Tymoczko, J.; Calle-Vallejo, F.; Schuhmann, W.; Bandarenka, A. S. *Nature Communications* **2016,** *7*, 10990.

8. Jiao, Y.; Zheng, Y.; Jaroniec, M.; Qiao, S. Z. *Chem Soc Rev* **2015,** *44* (8), 2060-2086.

9. Kang, Y.; Pyo, J. B.; Ye, X.; Gordon, T. R.; Murray, C. B. *ACS Nano* **2012,** *6* (6), 5642-5647.

10. Qi, Z.; Xiao, C.; Liu, C.; Goh, T. W.; Zhou, L.; Maligal-Ganesh, R.; Pei, Y.; Li, X.; Curtiss, L. A.; Huang, W. *Journal of the American Chemical Society* **2017,** *139* (13), 4762-4768.

11. Casado-Rivera, E.; Gál, Z.; Angelo, A. C. D.; Lind, C.; DiSalvo, F. J.; Abruña, H. D. *ChemPhysChem* **2003,** *4* (2), 193-199.

12. Bu, L.; Zhang, N.; Guo, S.; Zhang, X.; Li, J.; Yao, J.; Wu, T.; Lu, G.; Ma, J.-Y.; Su, D.; Huang, X. *Science* **2016,** *354* (6318), 1410.

13. Wang, G.; Huang, B.; Xiao, L.; Ren, Z.; Chen, H.; Wang, D.; Abruña, H. D.; Lu, J.; Zhuang, L. *Journal of the American Chemical Society* **2014,** *136* (27), 9643-9649.

14. Xia, B. Y.; Wu, H. B.; Wang, X.; Lou, X. W. *Journal of the American Chemical Society* **2012,** *134* (34), 13934-13937.

15. Anasori, B.; Lukatskaya, M. R.; Gogotsi, Y. *Nature Reviews Materials* **2017,** *2*, 16098.

16. Xiong, D.; Li, X.; Bai, Z.; Lu, S. *Small*, 1703419-n/a.

17. Naguib, M.; Kurtoglu, M.; Presser, V.; Lu, J.; Niu, J.; Heon, M.; Hultman, L.; Gogotsi, Y.; Barsoum, M. W. *Advanced Materials* **2011,** *23* (37), 4248-4253.

18. Lukatskaya, M. R.; Mashtalir, O.; Ren, C. E.; Dall'Agnese, Y.; Rozier, P.; Taberna, P. L.; Naguib, M.; Simon, P.; Barsoum, M. W.; Gogotsi, Y. *Science* **2013,** *341* (6153), 1502.

19. Ran, J.; Gao, G.; Li, F.-T.; Ma, T.-Y.; Du, A.; Qiao, S.-Z. *Nature Communications* **2017,** *8*, 13907.

20. Lin, H.; Wang, X.; Yu, L.; Chen, Y.; Shi, J. *Nano Letters* **2017,** *17* (1), 384-391.

21. Li, J.; Yuan, X.; Lin, C.; Yang, Y.; Xu, L.; Du, X.; Xie, J.; Lin, J.; Sun, J. *Advanced Energy Materials* **2017,** *7* (15), 1602725-n/a.

22. Er, D.; Li, J.; Naguib, M.; Gogotsi, Y.; Shenoy, V. B. *ACS Applied Materials & Interfaces* **2014,** *6* (14), 11173-11179.

23. Dong, Y.; Wu, Z.-S.; Zheng, S.; Wang, X.; Qin, J.; Wang, S.; Shi, X.; Bao, X. *ACS Nano* **2017,** *11* (5), 4792-4800.

CHAPTER 5. MORPHOLOGY INHERENCE FROM HOLLOW MOFS TO HOLLOW CARBON POLYHEDRONS IN PREPARING CARBON-BASED ELECTROCATALYSTS

Modified from a publication on the Journal of Materials Chemistry A

J. Mater. Chem. A, 2017, 5, 6186

Yuchen Pei,†[ab] Zhiyuan Qi,†[ab] Xinle Li,[ab] Raghu V. Maligal-Ganesh,[ab] Tian-Wei Goh,[ab]

Chaoxian Xiao,[a] and Wenyu Huang [ab]*

[a.] Department of Chemistry, Iowa State University, Ames, Iowa 50011, United State.

[b.] Ames Laboratory, U.S. Department of Energy, Ames, Iowa 50011, United States.

† These authors contribute equally.

5.1 Abstract

Hollow carbon nanostructures are emerging as advanced electrocatalysts for the oxygen reduction reaction (ORR) due to the effective usage of active sites and the reduced dependence on expensive noble metals. Conventional preparation of these hollow structures is achieved through templates (*e.g.*, SiO_2, CdS, and Ni_3C), which serve to retain the void interior during carbonization, leading to an essential template-removal procedure using hazardous acid etchants. Herein, we demonstrate the direct carbonization of unique hollow zeolitic imidazolate frameworks (ZIFs) for the synthesis of hollow carbon polyhedrons (HCPs) with well-defined morphology. The hollow ZIF precedent behaves bi-functionally as a carbon source and a morphology directing agent. This method evidences the strong morphology inherence of the hollow ZIFs during the carbonization, advancing the significant simplicity and environmental friendliness of this synthesis strategy. As-prepared HCPs show uniform polyhedral morphology and large void interiors, which enables their superior ORR activity. Iron can be doped into the HCPs (Fe/HCPs), rendering the Fe/HCPs with enhanced ORR property ($E_{1/2}$=0.850 V) in comparison with that of HCPs. We highlight the

efficient structural engineering to transform MOF precedents into advanced carbon nanostructures accomplishing morphological control and high electrocatalytic activity.

5.2 Introduction

Hollow carbon nanostructures have gained considerable attention due to their high thermal stability, high surface-to-volume ratios, promoted usability of external active sites, and tunable compositions.[1-4] These advantages endow hollow carbon nanostructures with widespread applications as heterogeneous catalysts,[5] electrode materials,[6] and selective adsorbents for metal ions.[7] Of particular interest, carbon-based nanostructures are potential cathode materials to reduce the usage of expensive Pt catalysts for oxygen reduction reaction (ORR) in polymer-electrolyte-membrane fuel cells (PEMFCs).[8,9] The hollow carbon shells feature more easily accessible active sites due to the short diffusion length for reactants to access the active sites in the thin shells, and they also hold various capabilities for doping elements (*e.g.*, Fe and N), which are beneficial to promote ORR activity.[8,10,11] The conventional synthesis of hollow carbon nanostructures usually starts from constructing a core/shell structure with sacrificial hard templates as core materials (*e.g.*, metal carbide,[6] quantum dots,[10] silica,[12] and polystyrene[13]) coated with carbon sources such as polymerized organic molecules. Subsequent pyrolysis can produce carbon sphere prototypes, where the subsequent removal of the core templates by the chemical etching is essential in most cases to afford the void interiors. Besides, constrained by the morphology of sacrificial templates, the derived hollow carbon nanostructures are mostly spherical.[14] It is very challenging to prepare hollow carbon nanostructures with controlled morphologies in a more facile manner.[15-17]

Metal-organic framework (MOF) and MOF hybrids are an emerging class of crystalline porous materials with extensive applications.[18-27] Direct carbonization of MOF precedents has been exemplified as an ideal route to prepare porous carbon materials.[28-31] Benefitting from high surface areas, tunable functional groups, and controlled morphologies of the parent MOF

precedents, MOF-derived porous carbons are also highly valued as active ORR catalysts.[32-38] Recently, considerable efforts have been devoted to developing hollow carbon nanostructures from the carbonization of MOF materials. Xu et al. obtained hollow carbon particles via the carbonization of Al-MIL-100 MOF, and subsequently removing the converged Al_2O_3 in the resultant carbonized materials by HF etching to induce void interiors.[39] Another interesting demonstration used a core/shell structure of zeolitic imidazolate framework (ZIF)/organic polymer hybrids, and the hollow interiors were generated *in situ* during carbonization.[40,41] Among these aforementioned strategies, the core/shell structure is essential in templates during carbonization to afford structural stability to the outer shell under high temperatures. We envisioned a direct transformation from hollow MOF precedents to hollow carbon particles, where the MOF shells can resist the structural collapse under the harsh carbonization conditions. This new strategy in preparing hollow carbons is inspired by the recent studies that MOF-derived carbons can inherit the morphology of their corresponding parent MOF precedents.[32,42] In comparison to previous core/shell template strategies, this hollow MOF to hollow carbon approach holds advantages including the easy operation, tunable composition, and completely avoiding hazardous etching chemicals (*e.g.*, HF).

Herein, we present the preparation of well-defined hollow carbon polyhedrons (HCPs) by the direct carbonization of hollow ZIF precedents (Scheme 1). Hollow ZIF precedents behave bi-functionally as a carbon source and as a morphological template to construct HCPs. Remarkably, the prepared HCPs exhibited high ORR activity with a half-wave potential ($E_{1/2}$) of 0.821 V (vs. RHE) in basic conditions. We further doped Fe and 2,2'-bipyridine in the hollow MOF precedents. After carbonization, the Fe-doped HCPs exhibited 24% enhancement in current density compared to bare HCPs.

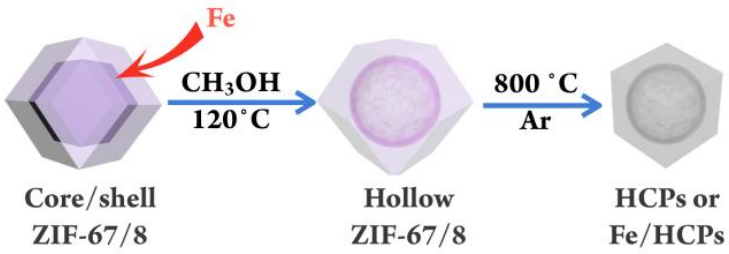

Scheme 1. The synthesis of HCPs from hollow ZIF-67/8 particles via direct carbonization.

5.3 Experimental Section

5.3.1 Synthesis of hollow carbon polyhedrons (HCPs)

The synthesis method was carried out by following reported literature with modifications.[43] 0.546 g $Co(NO_3)_2$ $6H_2O$, 0.558 g $Zn(NO_3)_2$ $6H_2O$, and 0.616 g 2-methylimidazole were dissolve in respective 7.5, 7.5, and 15 mL methanol. Under sonication at 45 ˚C, the Co-methanol solution was added into 2-methylimidazole-methanol solution in 1 min, and the mixture was maintained under sonication for 5 min to form a purple suspension (ZIF-67 cores). The Zn-methanol solution was then added into the as-formed purple suspension in 2 min and sonicated for another 15 min. The suspension was then sealed into a solvothermal reactor and maintained at 120 ˚C for 2 h to form hollow ZIF-67/8 particles. Hollow ZIF-67/8 particles were centrifuged, washed, and dried in vacuum. The hollow ZIF-67/8 particles were carbonized to form HCPs in a quartz boat placed in a temperature-programmed tube furnace. The ramping rate was controlled at 1 ˚C/min, and the samples were carbonized at 800 ˚C for 3 h in a 50 mL/min flow of Ar.

5.3.2 Synthesis of Fe-doped hollow carbon polyhedrons (Fe/HCPs)

The synthesis and carbonization of Fe/HCPs are similar to HCPs, except for an extra Fe loading step before the coating of ZIF-8 shells in the preparation of core/shell ZIF-67/8 particles. As-formed ZIF-67 cores were centrifuged, washed, and dispersed in 15 mL methanol. After adding

$Fe(NO_3)_3$ $6H_2O$ and 2,2'-bipyridine, the mixture was stirred at room temperature for 24 h. The resulting Fe/ZIF-67 cores were centrifuged, washed and dispersed in 15 mL methanol solution containing 0.616g 2-methylimidazole. The Zn-methanol solution was then added to the mixture to form ZIF-8 shells. After methanol hydrothermal treatment and carbonization, Fe/HCPs were obtained.

5.3.3 Synthesis of solid carbon polyhedrons (SCPs)

SCPs were synthesized by similar procedures in preparing HCPs without the methanol hydrothermal treatment of the core-shell ZIF-67/8.

5.3.4 Characterization

N_2 physisorption experiments were conducted by using Micromeritics 3Flex surface characterization analyzer at 77 K. PXRD patterns of the samples were acquired by a STOE Stadi P powder diffractometer using Cu Kα radiation (40 kV, 40 mA, λ=0.1541 nm). Transmission electron microscopy (TEM) images were acquired by using a Tecnai G2 F20 electron microscope operated at 200 kV. ICP–MS (X Series II, Thermo Scientific) and ICP-OES (Perkin Elmer Optima 2100DV) were performed to determine the actual metal content. XPS spectra were measured by a PHI 5500 Multi-technique system (Physical Electronics, Chanhassen, MN) equipped with a mono-chromatized Al K_α X-ray source (1486.6 eV).

5.3.5 Electrochemical analysis of ORR

All electrochemical tests were measured using a potentiostat (VSP-300, Bio-Logic Science Instruments). Catalysts were dispersed in mixtures of H_2O: isopropanol: 5% Nafion solution or isopropanol:H_2O:5% Nafion solution (4:1:0.025) to prepare a 2 mg/mL ink depending on the dispersion. After sonication for 30 min, 20 μL of the catalyst ink was applied onto a rotational ring-disk electrode (RRDE, 5 mm diameter) as a working electrode. A platinum wire and a

saturated Ag/AgCl electrode were used respectively as the counter and the reference electrodes. The water used in all experiments was Millipore ultrapure water (18.2 mΩ). All ORR measurements were carried out at 25 ˚C in a 0.1 M KOH aqueous solution. The sweep speed for linear sweep voltammetry is 10 mV/s.

5.4 Results and Discussion

To fulfill the direct transformation from hollow MOF to hollow carbon nanostructure, hollow ZIF-67/8 particles were selected as the MOF precedent. ZIF-67 $[Co(MeIm)_2]_n$ (MeIm=2-methylimidazole) and ZIF-8 $[Zn(MeIm)_2]_n$ are isostructural MOF materials with similar zeolite SOD topology. Both of them consist of 2-methylimidazole linkers albeit with different metal sites (Co in ZIF-67 and Zn in ZIF-8). In general, ZIFs are optimum MOF precedents to achieve a high ORR activity of the resultant carbon materials due to the high nitrogen content in 2-methylimidazole linkers (ca. 30 wt.%). Moreover, the N atoms are positioned within the aromatic ring, which increases the efficiency of N incorporation during carbonization.[29] The N species in (metal-doped) ZIF-derived carbon materials could also generate more metal-N species active in ORR, such as CoN_x and FeN_x.[32] In hollow ZIF-67/8-derived HCPs, the shorten diffusion length in the shell can facilitate the molecule transfer, beneficial to promote the ORR activity.[10]

Following this design principle, we first synthesized hollow ZIF-67/8 particles via a reported protocol,[43] and subsequently carbonized them to afford various carbon nanostructures. The hollow structure in ZIF-67/8 particles was employed by the selective destruction of ZIF-67 cores in core/shell ZIF-67/8 particles via the solvothermal route in methanol. The resultant hollow ZIF-67/8 particles show the well-defined rhombic dodecahedral morphology with deformed ZIF-67 fragments trapped inside. This synthesis is facile and does not require a hard template to sustain the hollow ZIF-67/8 precedents, and therefore precludes the laborious etching steps involved in

removing internal templates after carbonization. Due to the morphology inherence during MOF carbonization,[32,42] we proposed that these hollow ZIF-67/8 particles could be directly carbonized to form HCPs, where the hollow nature of the ZIF-67/8 particles can be retained. It is notable that the retained ZIF-67 fragments readily restore a significant amount of Co in hollow ZIF-67/8 particles during the destruction of the ZIF-67 cores. This observation inspired us to utilize the ZIF-67 core as a carrier to dope other elements into the hollow ZIF-67/8 particles. Since Fe/N dopants in carbon materials can lead to enhanced ORR activities,[44,45] we loaded $Fe(NO_3)_3$ $6H_2O$ and 2,2'-bipyridine as Fe and N precursors into ZIF-67 cores. The destruction of these Fe-doped ZIF-67 cores can induce Fe-doped hollow ZIF-67/8 particles, subsequently resulting in Fe-doped HCPs with enhanced ORR performance. In a nutshell, we anticipate that hollow ZIF-67/8 particles are ideal starting materials to prepare HCPs with superior ORR activity and controllable morphology.

Hollow ZIF-67/8 particles were first prepared with sizes ranging from 300 to 600 nm measured by TEM (Fig. 1a), of which the size and morphology are similar to their parent core/shell ZIF-67/8 precedents shown in Fig. 1b. They are endowed with large void interiors and a polyhedral morphology, which are advantageous in preparing HCPs. We observed the size enlargement of hollow ZIF-67/8 particles after methanol solvothermal treatment in comparison to their core/shell ZIF-67/8 counterparts as reported in literature.[43] With these hollow ZIF precedents, we proceeded to an elaborate carbonization to the hollow ZIF-67/8 particles at 800 ˚C for 3 h at a ramping rate of 1 ˚C/min in Ar atmosphere. As expected, as-synthesized HCPs (Fig. 1c) demonstrate well-defined polyhedral morphologies similar to their parent hollow ZIF-67/8 precedents. The hollow features of HCPs are clearly seen with the lighter interiors and their surrounding darker edges (Fig. 1e). The sizes of HCPs are similar to their hollow ZIF-67/8 precedents with a slight structural shrinkage. Several metal particles are also observed distributed across the HCPs' framework.

These particles are presumed to be Co/CoO_x since only trace remnant of Zn was determined (<0.1 wt.%, Table S1) by inductively coupled plasma-mass spectrometry (ICP-MS) after the carbonization. To better evaluate the synthesis condition, we varied the carbonization temperatures (600, 800, and 1000 ˚C), time (1, 3, and 5 h at 800 ˚C) and atmosphere (Ar, N_2, and 10% H_2/Ar). Their ORR performances were shown in Figure S1 and Table S3. The carbonization condition of 3 h at 800 ˚C under Ar atmosphere is optimal to obtain the best ORR activity for HCPs. For the comparison, we also carbonized core/shell ZIF-67/8 particles to afford solid carbon polyhedrons (SCPs, as shown in Fig. 1d and f). Since the hollow ZIF-67/8 particles after methanol solvothermal treatment are larger than their core/shell ZIF-67/8 precursors,[43] the resultant HCPs is also larger than the as-prepared SCPs. Both HCPs and SCPs resembled their respective hollow and solid ZIF-67/8 precedents, which evidences the morphology inherence during MOF carbonization.

Co and Zn contents of HCPs, SCPs, and their parent ZIF-67/8 precedents were determined by ICP-MS (Table S1 in Supporting Information). Core/shell ZIF-67/8 particles consist of 18.2 wt.% Co and 5.5 wt.% Zn, conformed to the presence of both ZIF-67 cores and ZIF-8 shells. After methanol solvothermal treatment, hollow ZIF-67/8 particles show increased Zn contents to 18.6 wt.%, presumably due to the mass reduction from the destruction of inner ZIF-67 cores. Co contents of hollow ZIF-67/8 particles decrease to 11.4 wt.%, indicating the significant retention of ZIF-67 fragments within the ZIF-8 shell. The carbonization of both hollow and core/shell ZIF-67/8 particles induces consistent weight loss of ca. 50 wt.%. The resultant HCPs and SCPs have Co contents of 23.9 and 41.3 wt.%, respectively. The roughly doubled Co contents in HCPs and SCPs, compared to that of their parent MOF precedents, are consistent with their weight losses. After the carbonization at 800 ˚C, less than 0.1 wt.% of Zn contents was detected in both HCPs and SCPs. The scarcity of Zn in HCPs and SCPs also confirms that the particles observed on the

HCPs are Co/CoO_x nanoparticles in the TEM images. ICP-MS data of Co and Zn contents agree with the general carbonization pathway of ZIF-materials. 2-methylimidazole linkers pyrolyze into degraded hydrocarbons, whereas Co sites in ZIF-67 can form metallic Co and various carbides/nitrides species (CoN_x and CoC_x).[32] Under high temperatures, Zn can evaporate from the system due to their high vapor pressure, while Co species remain in the as-formed carbon materials.

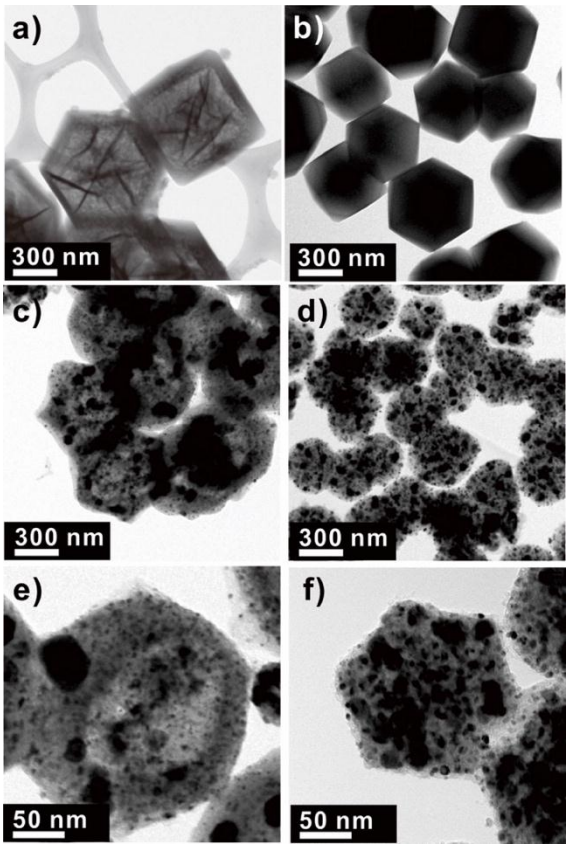

Fig. 1. TEM images of (a) hollow ZIF-67/8 particles, (b) core/shell ZIF-67/8 particles, (c) HCPs, and (d) SCPs. (e) and (f) are enlarged TEM images of respective HCPs and SCPs to identify the hollow interiors.

We employed N_2 physisorption to characterize the porous structures of HCPs and SCPs as shown in Fig. 2a. The isotherms of both HCPs and SCPs show type IV characteristics. A distinct hysteresis loop of HCPs indicates more mesopore volume (0.47 $cm^3\ g^{-1}$) in comparison to that of SCPs (0.35 $cm^3\ g^{-1}$).[4,46,47] The pore size distributions of HCPs and SCPs agree with their

mesoporous characters (Fig. 2b). The mesopores in SCPs are between 2-10 nm in diameter. Differing from SCPs, HCPs show a broader mesoporous feature centered at 60 nm corresponding to their void interiors. We noticed that the void space of 40-80 nm in size is smaller than the theoretical diameter (200-300 nm) of the hollow interior, assuming that HCPs could retain the morphology of their parent hollow ZIF-67/8 precedents. Contradictory to most intact hollow features of HCPs observed in TEM, we speculate that the size reduction of the hollow space shown in N_2-physisorption can be due to the presence of large metal nanoparticles or carbon structures that separate the void interior into several isolated compartments. Interestingly, the Brunauer-Emmett-Teller (BET) surface area of HCPs was measured as 227 m^2 g^{-1}, which is slightly lower than that of SCPs (282 m^2 g^{-1}). During the ZIF-67 core destruction to generate parent hollow ZIF-67/8 particles, degraded Co was reported to etch ZIF-8 shells.[43] Even though the void structure was retained after the carbonization of hollow ZIF-67/8 particles, we infer that the as-formed HCPs can undergo slight structural deformation under high temperatures. This deformation is due to the reduced thermal stability of the etched ZIF shell, which is also responsible for the observed lower BET surface areas in HCPs. The crystallization properties of HCPs, SCPs, and their parent ZIF-67/8 precedents were investigated by powder X-ray diffraction (PXRD) analysis (Fig. 3a). Both hollow and core/shell ZIF-67/8 particles exhibited well-crystallized ZIF structures. After carbonization, HCPs, and SCPs have similar PXRD patterns with amorphous structures. The broad feature around 25˚ is attributed to the (002) diffraction of graphitic carbon.[32] The series of distinct peaks at 22˚, 52˚, and 76˚ are characteristic peaks of bulk Co (PDF#15-0806), which reveals the presence of metallic Co nanoparticles in HCPs and SCPs.

Fe-doping and N-rich environment are critical to enhancing ORR activities of carbon materials.[10] We thus prepared the Fe-doped HCPs with similar hollow structures. As-prepared ZIF-

67 cores were loaded with $Fe(NO_3)_3$ $6H_2O$ as the Fe precursor and 2,2'-bipyridine as the additional N source. To accomplish the desirable hollow structure, ZIF-8 shells were then coated on the resulting Fe-loaded ZIF-67 cores to form the Fe-core/shell ZIF-67/8 particles. After methanol solvothermal treatment and carbonization, Fe-doped HCPs (denoted as Fe/HCPs) were obtained. The TEM images in Fig. 3b and S2 show that Fe/HCPs have similar morphological characteristics as bare HCPs. Target Fe/N loadings were controlled as 1.0 wt.% Fe and 2.0 wt.% 2,2'-bipyridine relative to the mass of ZIF-67 cores. The final Fe contents in Fe/HCPs were measured as 1.0 wt.% by inductively coupled plasma optical emission spectroscopy (ICP-OES). We further studied Co, Zn contents (Table S1) and PXRD features (Fig. S3) of Fe/HCPs, which agree well with that of HCPs.

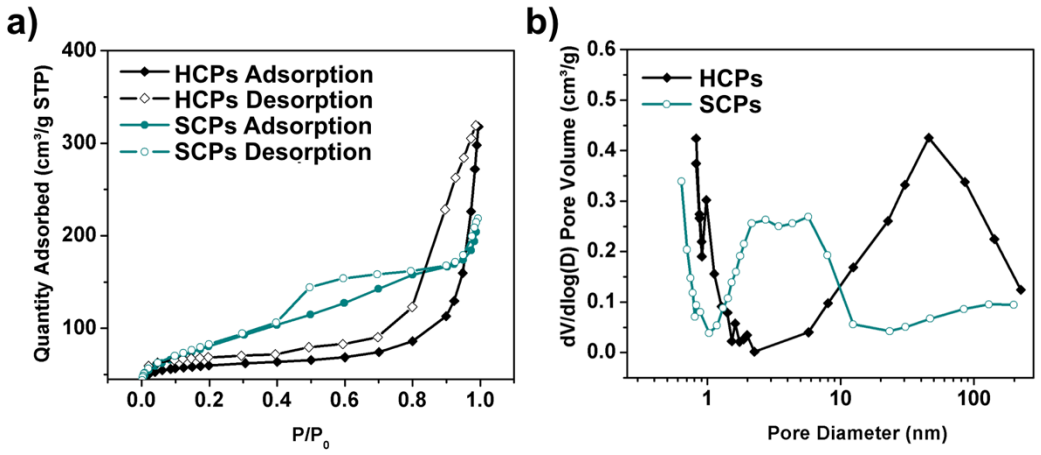

Fig. 2. (a) N_2 physisorption isotherms, and (b) pore size distributions of HCPs and SCPs.

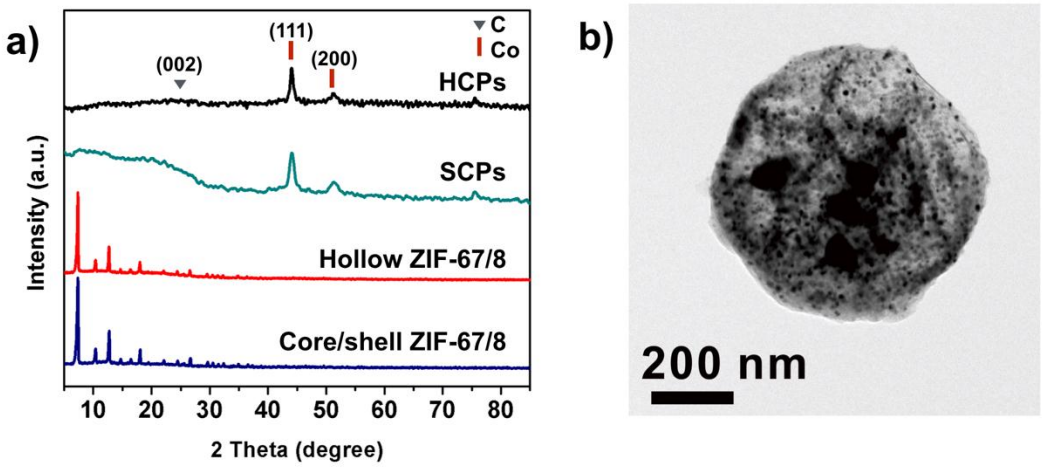

Fig. 3. (a) PXRD patterns of HCPs, SCPs, and their parent ZIF-67/8 precedents; (b) characteristic TEM images of Fe/HCPs.

Surface characteristics of HCPs, SCPs and Fe/HCPs were measured using X-ray photoelectron spectroscopy (XPS). Fig. S4 presents N 1s, Co 2p, Zn 2p, and Fe 2p spectra of respective carbon materials, and detailed analyses are summarized in Table S4. The HCPs have the highest surface N concentration at 6.7 at.% compared to SCPs (5.2 at.%) and Fe/HCPs (5.6 at.%). We deconvoluted the N peaks in XPS spectra to pyridinic-N, graphitic-N, and oxidized-N.[48,49] This indicates that most of the N atoms in the aromatic ring of 2-methyimidazole were transformed to these three types of N species.[33] HCPs and Fe/HCPs have consistently higher fractions of pyridinic-N and less oxidized-N compared to SCPs. The pyridinic-N species donate electrons to carbon networks, which is beneficial to ORR activity.[50] Co spectra depict that most of the Co surfaces are oxidized to CoO_x species. Consistent with low Zn contents in ICP-MS results, surface Zn is also observed to be less than 0.3 at.% in HCPs, SCPs and Fe/HCPs, confirming a nearly complete evaporation of Zn at high temperatures. Fe species were not detected on the surface of 1.0 wt.% Fe/HCPs. Since ICP-OES results confirm the presence of Fe in 1.0 wt.% Fe/HCPs, the low Fe contents in our samples may fall below the detection limit of XPS.

Alternatively, Fe can be trapped inside the hollow structure of Fe/HCPs, where the Fe-doped ZIF-67 cores were used as the Fe carrier. This process can also be extended to dope other metal atoms into such hollow carbon structures.

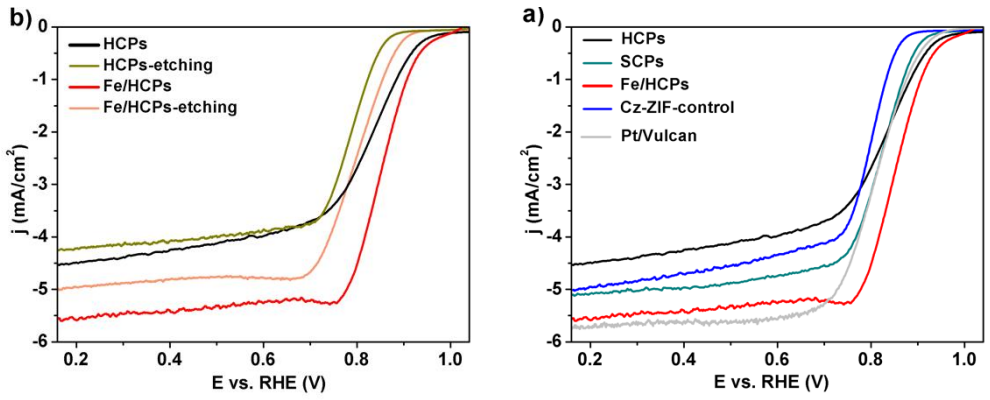

Fig. 4. (a) ORR polarization curves of HCPs, SCPs, Fe/HCPs, Cz-ZIF-control and commercial Pt/Vulcan catalysts. (b) ORR polarization curves of HCPs, HCPs-etching, Fe/HCPs, and Fe/HCPs-etching to investigate the active sites for ORR. In all ORR measurements, the ink concentrations of carbon catalysts and Pt/Vulcan were controlled as 2 mg/mL and 0.5 mg/mL. 20 μL of above mentioned catalyst ink was applied on the RRDE.

With desired structural characterizations of HCPs and SCPs in place, we investigated their ORR activities using the rotating ring-disk electrode (RRDE) in a 0.1 M KOH electrolyte at 25 ˚C. Detailed potential and current density values are summarized in Table S5. As shown in Fig. 4, HCPs have an onset potential (E_{onset}) of 0.948 V, and $E_{1/2}$ is 0.821 V. To the best of our knowledge, these electrochemical values demonstrate our HCPs as highly active ORR catalysts comparing to previous reports (Table S6). Interestingly, SCPs have a comparable $E_{1/2}$ (0.810 V) and a lower E_{onset} (0.912 V) in contrast to that of the HCPs. However, the kinetic current density of HCPs (0.87 mA/cm^2 at 0.90 V) is ca. 2 times higher, in sharp contrast to that of SCPs (0.40 mA/cm^2). It is

interesting to note that the HCPs have lower surface area while demonstrating higher kinetic current density, which indicates that the hollow structure of HCPs can better utilize the easily accessible active sites accounting for ORR. To better evaluate the ORR activity of HCPs and SCPs, we prepared another carbonized bimetallic ZIF-67/8 as a control catalyst (denoted as Cz-ZIF-control) by co-mixing the Co/Zn precursors in the preparation of ZIFs. The Cz-ZIF-control shows solid structures with irregular shapes (Fig. S6).[34] We characterized Cz-ZIF-control using PXRD, XPS, ICP-MS, N_2 physisorption, and Raman spectrometry (Table S1-7 and Fig. S6-8). Solid Cz-ZIF-control displays mostly similar size, crystallization, and chemical properties in comparison to HCPs, except for the 30% lower surface N contents determined by XPS. We, therefore, tested ORR activity for this Cz-ZIF-control under identical conditions. Cz-ZIF-control has much worse ORR performance compared to HCPs. $E_{1/2}$ and E_{onset} of Cz-ZIF-control are 0.793 V and 0.869 V, which are 28 mV and 79 mV lower than HCPs. These electrochemical results demonstrate the synthesis and structural advantages of HCPs, which can promote their ORR activity.

It is notable that the limiting current of HCPs is 4.49 mA/cm^2 at 0.2 V, which is not competitive to Pt/Vulcan (5.73 mA/cm^2) and SCPs (5.08 mA/cm^2). We envision that the Fe-doping in Fe/HCPs can complement the low limiting current of HCPs due to the Fe promotion to ORR.[51] As expected, the current density of Fe/HCPs is boosted to 5.59 mA/cm^2, which is close to Pt/Vulcan and 24 % enhanced in comparison to that of HCPs. We also varied the Fe loadings from 0.4, 1.0, 3.3 and 19.8 wt.% on Fe/HCPs as determined by ICP-OES, and employed them for ORR analysis. 1.0 wt.% Fe ($E_{1/2}$ as 0.850 V) stands out as the most active catalysts among different Fe loadings under our synthesis and reaction conditions (Fig. S9 and Table S8), and this $E_{1/2}$ even surpasses that of HCPs by 29 mV. We propose that the Fe doping can facilitate the reduction of O_2 on the carbon surface responsible for the promotion of ORR current density in Fe/HCPs. To

further validate this hypothesis, we placed HCPs and Fe/HCPs in 6 M HNO_3 overnight to etch the metallic contents, denoted as HCPs-etching and Fe/HCPs-etching (Table S1). After etching, Co contents are consistently reduced to ca. 30% for both HCPs and Fe/HCPs. The Fe content of Fe/HCPs-etching was measured as 0.9 wt.%, which is ca. 30% loss to that of the original Fe/HCPs considering the mass loss of Co. Fig. 4b illustrates the distinct decreasing ORR activity of both HCPs-etching and Fe/HCPs-etching in contrast to their respective counterparts before etching treatments. Respective $E_{1/2}$ of HCPs-etching (0.784 V) and Fe/HCP-etching (0.799 V) are similar, and they both contain comparable Co contents (ca. 8-12 wt.%). Limiting currents at 0.2 V of Fe/HCPs-etching (4.96 mA/cm^2) are still 18% higher than HCPs-etching (4.22 mA/cm^2), consistent with the adequate remnant Fe contents (ca. 70%) in Fe/HCPs-etching. We thus suggest that the Co species on our HCPs and Fe/HCPs influence their ORR performance. Meanwhile, the doping of Fe can further increase the mass transport limiting current density, which evidences the promotion effect of Fe in ORR activity.[52-54] The chronoamperometric responses for HCPs and Fe/HCPs were also acquired for 40,000 s as shown in Fig. S10. Both HCPs and Fe/HCPs show excellent stabilities with respective 10.9 and 12.7% current drop, in comparison to the poor stability of Pt/Vulcan (53.0% current drop).

5.5 Conclusion

In summary, we demonstrate a novel and facile synthesis of hollow carbon polyhedrons (HCPs) via a direct carbonization of hollow ZIF-67/8 particles. This approach presents the morphology inherence of carbon materials derived from their parent MOF precedents. With the benefits afforded by the structural reassembly during carbonization, we designed the ideal Fe/HCPs catalyst with remarkable enhancement of ORR activity, combining the advantages of the high porosity of parent ZIFs, unique hollow structures, and Fe-doping promotion. HCPs and

Fe/HCPs readily display superior ORR activity in basic conditions. This work demonstrates the use of structural engineering for the preparation of porous carbon nanostructures in a controllable manner as efficient electrocatalysts.

5.6 Acknowledgements

We are grateful for the start-up funds support from the Ames Laboratory (Royalty Account) and Iowa State University. The Ames Laboratory is operated for the U.S. Department of Energy by Iowa State University under Contract No. DE-AC02-07CH11358. We thank Gordon J. Miller for the use of X-ray diffractometer, Igor I. Slowing for the use of ICP-OES, Xinwei Wang for the use of Raman spectrometer, and Dapeng Jing for the assistance in the XPS measurement.

5.7 Reference

1 J. Liu, N. P. Wickramaratne, S. Z. Qiao and M. Jaroniec, *Nat. Mater*., 2015, **14**, 763−774.

2 W. M. Zhang, J. S. Hu, Y. G. Guo, S. F. Zheng, L. S. Zhong, W. G. Song and L. J. Wan, *Adv. Mater.*, 2008, **20**, 1160−1165.

3 Q. Sun, W. C. Li and A. H. Lu, *Small*, 2013, **9**, 2086−2090.

4 X. Fang, J. Zang, X. Wang, M. S. Zheng and N. Zheng, *J. Mater. Chem. A*, 2014, **2**, 6191−6197.

5 R. Liu, S. M. Mahurin, C. Li, R. R. Unocic, J. C. Idrobo, H. Gao, S. J. Pennycook and S. Dai, *Angew. Chem. Int. Ed.*, 2011, **50**, 6799−6802.

6 Z. L. Schaefer, M. L. Gross, M. A. Hickner and R. E. Schaak, *Angew. Chem. Int. Ed.*, 2010, **49**, 7045-7048.

7 D. H. Liu, Y. Guo, L. H. Zhang, W. C. Li, T. Sun and A. H. Lu, *Small*, 2013, **9**, 3852−3857.

8 Y. Hu, J. O. Jensen, W. Zhang, L. N. Cleemann, W. Xing, N. J. Bjerrum and Q. Li, *Angew. Chem. Int. Ed.*, 2014, **53**, 3675−3679.

9 J. Sun, H. Yin, P. Liu, Y. Wang, X. Yao, Z. Tang and H. Zhao, *Chem. Sci.*, 2016, **7**, 5640-5646.

10 Y. Wang, A. Kong, X. Chen, Q. Lin and P. Feng, *ACS Catal.*, 2015, **5**, 3887−3893.

11 C. Han, S. Wang, J. Wang, M. Li, J. Deng, H. Li and Y. Wang, *Nano Res.*, 2014, **7**, 1809−1819.

12 N. Jayaprakash, J. Shen, S. S. Moganty, A. Corona and L. A. Archer, *Angew. Chem. Int. Ed.*, 2011, **50**, 5904−5908.

13 J. Han, G. Xu, B. Ding, J. Pan, H. Dou and D. R. MacFarlane, *J. Mater. Chem. A*, 2014, **2**, 5352−5357.

14 F. Caruso, R. A. Caruso and H. Möhwald, *Science*, 1998, **282**, 1111−1114.

15 W. Xia, J. Zhu, W. Guo, L. An, D. Xia and R. Zou, *J. Mater. Chem. A*, 2014, **2**, 11606−11613.

16 H. Wu, X. Qian, H. Zhu, S. Ma, G. Zhu and Y. Long, *RSC Adv.*, 2016, **6**, 6915−6920.

17 W. Li, X. Wu, H. Liu, J. Chen, W. Tang and Y. Chen, *New J. Chem.*, 2015, **39**, 7060−7065.

18 R. C. Huxford, J. Della Rocca and W. Lin, *Curr. Opin. Chem. Biol.*, 2010, **14**, 262−268.

19 L. E. Kreno, K. Leong, O. K. Farha, M. Allendorf, R. P. Van Duyne and J. T. Hupp, *Chem. Rev.*, 2011, **112**, 1105−1125.

20 S. Sen, N. N. Nair, T. Yamada, H. Kitagawa and P. K. Bharadwaj, *J. Am. Chem. Soc.*, 2012, **134**, 19432−19437.

21 J. A. Mason, M. Veenstra and J. R. Long, *Chem. Sci.*, 2014, **5**, 32−51.

22 X. Li, Z. Guo, C. Xiao, T. W. Goh, D. Tesfagaber and W. Huang, *ACS Catal.*, 2014, **4**, 3490−3497.

23 X. Li, T. W. G. Goh, C. Xiao, A. L. D. Stanton, Y. Pei, P. K. Jain and W. Huang, *ChemNanoMat*, 2016, **2**, 810−815.

24 H. Yin and Z. Tang, *Chem. Soc. Rev.*, 2016, **45**, 4873-4891.

25 L. He, Y. Liu, J. Liu, Y. Xiong, J. Zheng, Y. Liu and Z. Tang, *Angew. Chem. Int. Ed.*, 2013, **52**, 3741-3745.

26 S. Zhao, Y. Wang, J. Dong, C.-T. He, H. Yin, P. An, K. Zhao, X. Zhang, C. Gao, L. Zhang, J. Lv, J. Wang, J. Zhang, A. M. Khattak, N. A. Khan, Z. Wei, J. Zhang, S. Liu, H. Zhao and Z. Tang, *Nat. Energy*, 2016, **1**, 16184-16194.

27 W Cai, T. Lee, M. Lee, W. Cho, D. Y. Han, N. Choi, A. C. Yip and J. Choi, *J. Am. Chem. Soc.*, 2014, **136**, 7961-7971.

28 B. Liu, H. Shioyama, T. Akita and Q. Xu, *J. Am. Chem. Soc.*, 2008, **130**, 5390−5391.

29 W. Xia, A. Mahmood, R. Zou and Q. Xu, *Energy Environ. Sci.*, 2015, **8**, 1837−1866.

30 S. J. Yang, T. Kim, J. H. Im, Y. S. Kim, K. Lee, H. Jung and C. R. Park, *Chem. Mater.*, 2012, **24**, 464−470.

31 X.-W. Liu, T.-J. Sun, J.-L. Hu and S.-D. Wang, *J. Mater. Chem. A*, 2016, **4**, 3584-3616.

32 Y. Z. Chen, C. Wang, Z. Y. Wu, Y. Xiong, Q. Xu, S. H. Yu and H. L. Jiang, *Adv. Mater.*, 2015, **27**, 5010−5016.

33 J. Tang, R. R. Salunkhe, J. Liu, N. L. Torad, M. Imura, S. Furukawa and Y. Yamauchi, *J. Am. Chem. Soc.*, 2015, **137**, 1572−1580.

34 A. Aijaz, J. Masa, C. Rosler, W. Xia, P. Weide, A. J. Botz, R. A. Fischer, W. Schuhmann and M. Muhler, *Angew. Chem. Int. Ed.*, 2016, **55**, 4087−4091.

35 A. Aijaz, N. Fujiwara and Q. Xu, *J. Am. Chem. Soc.*, 2014, **136**, 6790−6793.

36 S. Zhao, H. Yin, L. Du, L. He, K. Zhao, L. Chang, G. Yin, H. Zhao, S. Liu and Z. Tang, *ACS Nano*, 2014, **8**, 12660-12668.

37 K. Shen, X. Chen, J. Chen and Y. Li, *ACS Catal.*, 2016, **6**, 5887-5903.

38 M. Li, W. Wang, M. Yang, F. Lv, L. Cao, Y. Tang, R. Sun and Z. Lu, *RSC Adv.*, 2015, **5**, 7356-7362.

39 A. Aijaz, J. K. Sun, P. Pachfule, T. Uchida and Q. Xu, *Chem. Commun.*, 2015, **51**, 13945−13948.

40 S. Hong, J. Yoo, N. Park, S. M. Lee, J. G. Park, J. H. Park and S. U. Son, *Chem. Commun.*, 2015, **51**, 17724−17727.

41 S. Yang, L. Peng, P. Huang, X. Wang, Y. Sun, C. Cao and W. Song, *Angew. Chem. Int. Ed.*,
2016, **55**, 4016−4020.

42 G. Srinivas, V. Krungleviciute, Z. X. Guo and T. Yildirim, *Energy Environ. Sci*., 2014, **7**, 335−342.

43 J. Yang, F. Zhang, H. Lu, X. Hong, H. Jiang, Y. Wu and Y. Li, *Angew. Chem. Int. Ed.*, 2015, **54**, 10889−10893.

44 J. Tian, A. Morozan, M. T. Sougrati, M. Lefevre, R. Chenitz, J. P. Dodelet, D. Jones and F. Jaouen, *Angew. Chem. Int. Ed.*, 2013, **52**, 6867−6870.

45 E. Proietti, F. Jaouen, M. Lef èvre, N. Larouche, J. Tian, J. Herranz and J. P. Dodelet, *Nat. Commun.*, 2011, **2**, 416-424.

46 T. Yang, J. Liu, R. Zhou, Z. Chen, H. Xu, S. Z. Qiao and M. J. Monteiro, *J. Mater. Chem. A*, 2014, **2**, 18139−18146.

47 S. Chen, J. Bi, Y. Zhao, L. Yang, C. Zhang, Y. Ma, Q. Wu, X. Wang and Z. Hu, *Adv. Mater.*, 2012, **24**, 5593−5597.

48 T. S. Olson, S. Pylypenko and P. Atanassov, *J. Phys. Chem. C*, 2010, **114**, 5049−5059.

49 V. B. Parambhath, R. Nagar and S. Ramaprabhu, *Langmuir*, 2012, **28**, 7826−7833.

50 S. Yasuda, L. Yu, J. Kim and K. Murakoshi, *Chem. Commun.*, 2013, **49**, 9627−9629.

51 Q. Yi, Y. Zhang, X. Liu, B. Xiang and Y. Yang, *J. Mater. Sci.*, 2014, **49**, 729−736.

52 J. S. Lee, G. S. Park, S. T. Kim, M. Liu and J. Cho, *Angew. Chem.*, 2013, **125**, 1060−1064.

53 H. Liu, M. Dou, F. Wang, J. Liu, J. Ji and Z. Li, *RSC Adv.*, 2015, **5**, 66471−66475.

54 Z. Y. Yang, Y. X. Zhang, L. Jing, Y. F. Zhao, Y. M. Yan and K. N. Sun, *J. Mater. Chem. A*, 2014, **2**, 2623−2627.

5.8 Supporting Information

Synthesis of ZIF-control and Cz-ZIF-control

50 mL 0.1 mol/L $M(NO_3)_2$ $6H_2O$ (M = Zn and Co, Zn:Co = 1:1) methanol solution and 50 mL 0.8 mol/L 2-methyl imidazole methanol solution were prepared separately. Under magnetic stirring, the 2-methylimidazole solution was poured into Zn/Co solution and stirred for

2 hrs. The mixture solution was centrifuged, washed and dried in vacuum. After carbonization following the same procedure as that of HCPs, Cz-ZIF-control was obtained.

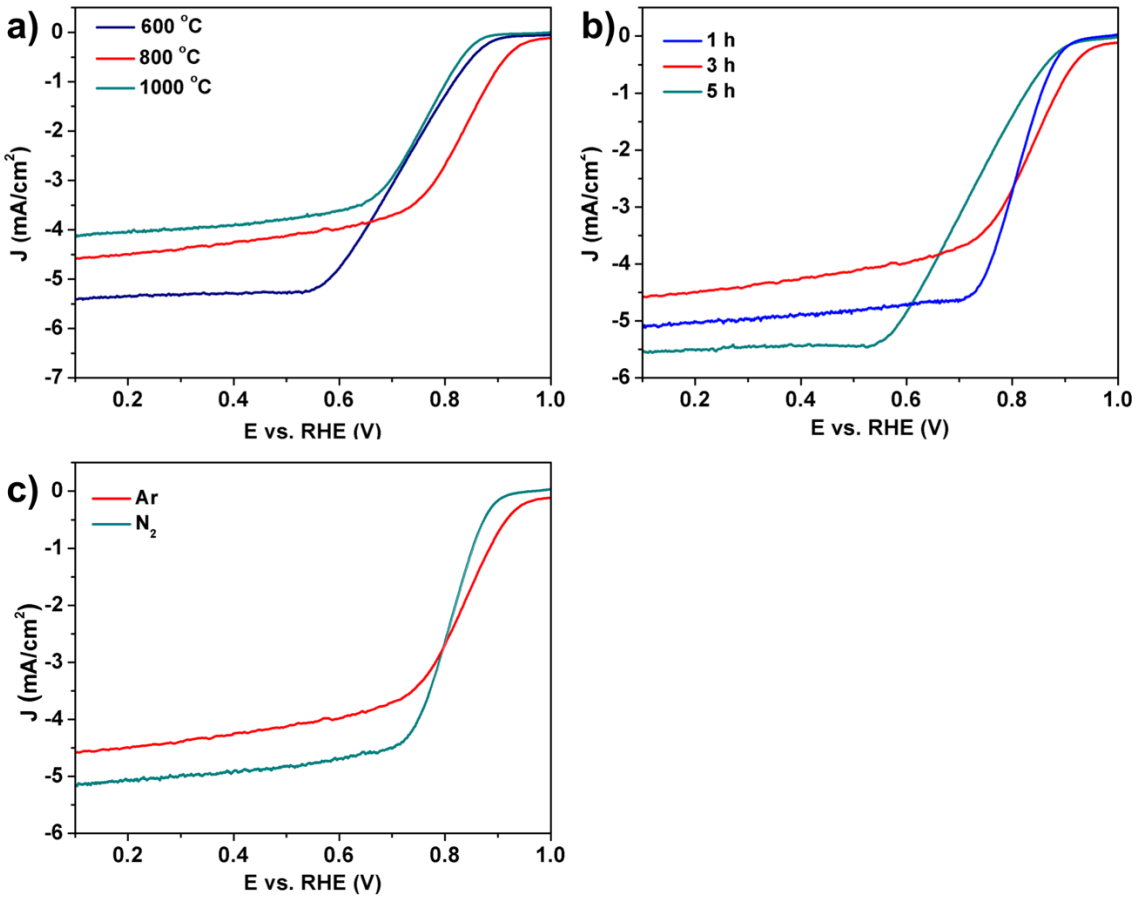

Figure S1. ORR performance of a) HCPs carbonized at 600, 800, and 1000 ℃ for 3 h in Ar; b) HCPs carbonized at 800 ℃ for 1, 3 and 5 h Ar; and c) HCPs carbonized at 800 ℃ for 3 h in Ar and N_2. In all conditions, HCPs prepared at 800 ℃ for 3 h have the best $E_{1/2}$. We did not evaluate the ORR performance of HCPs when employing 10% H_2/Ar, because most of the carbons in HCPs were removed/decomposed in the presence of H_2 at 800 ℃.

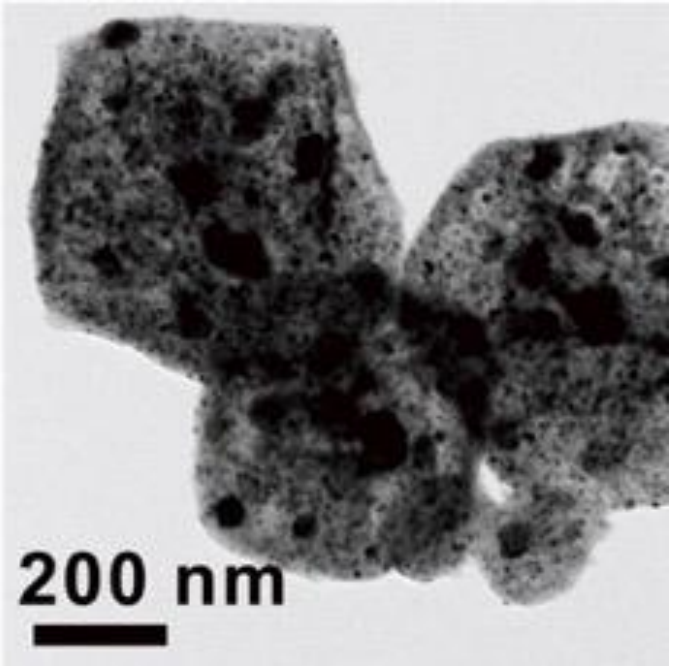

Figure S2. TEM image of Fe/HCPs.

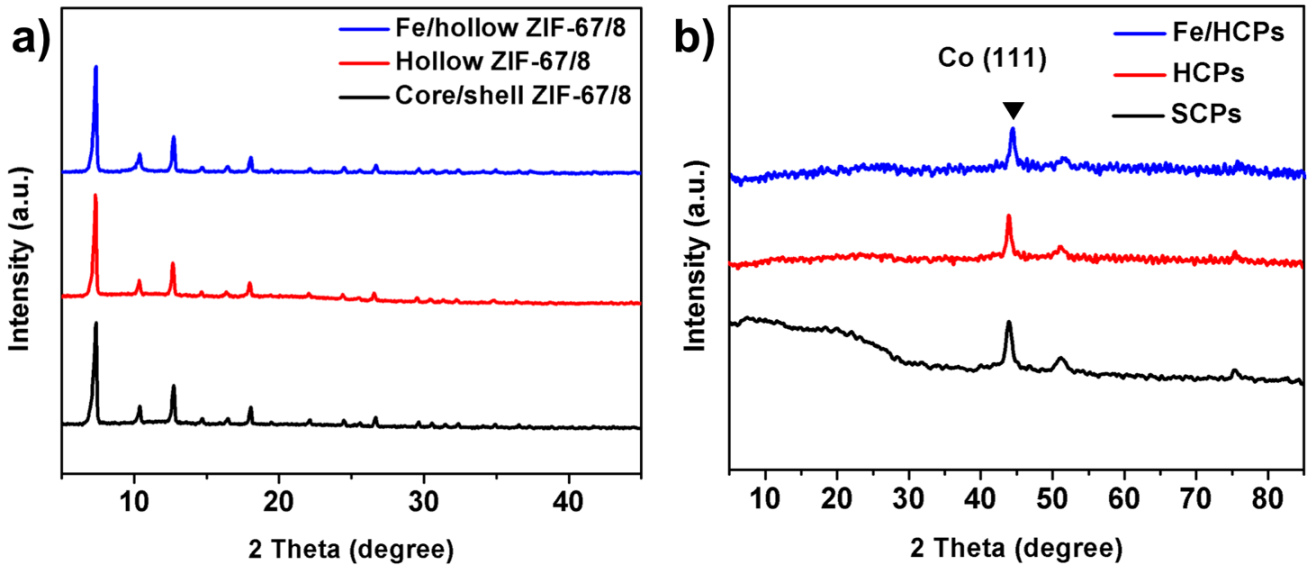

Figure S3. PXRD patterns of (a) parent ZIFs, and (b) HCPs, SCPs, and Fe/HCPs.

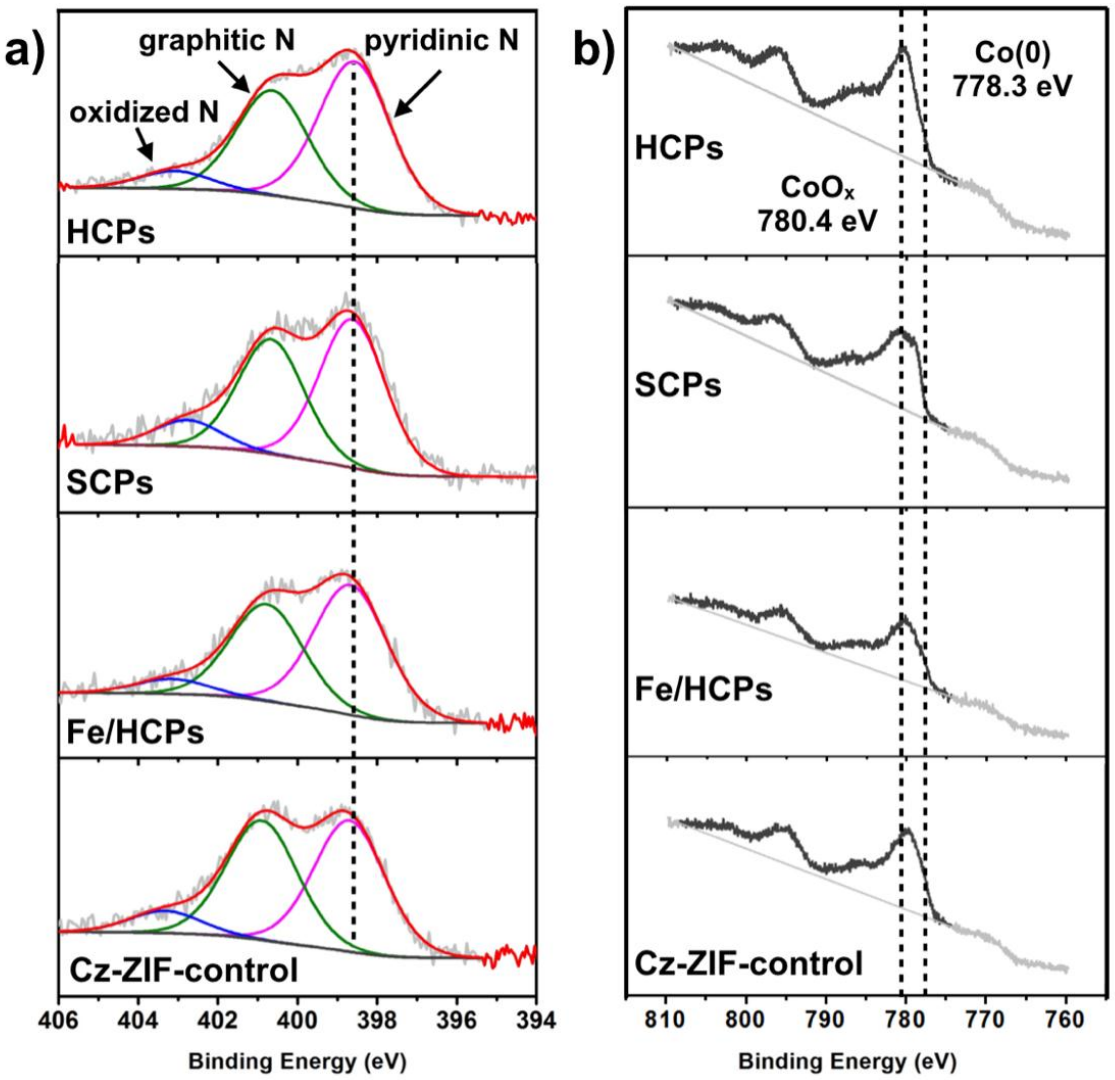

Figure S4. XPS spectra of HCPs, SCPs, Fe/HCPs and Cz-ZIF-control: (a) N 1s, and (b) Co 2p.

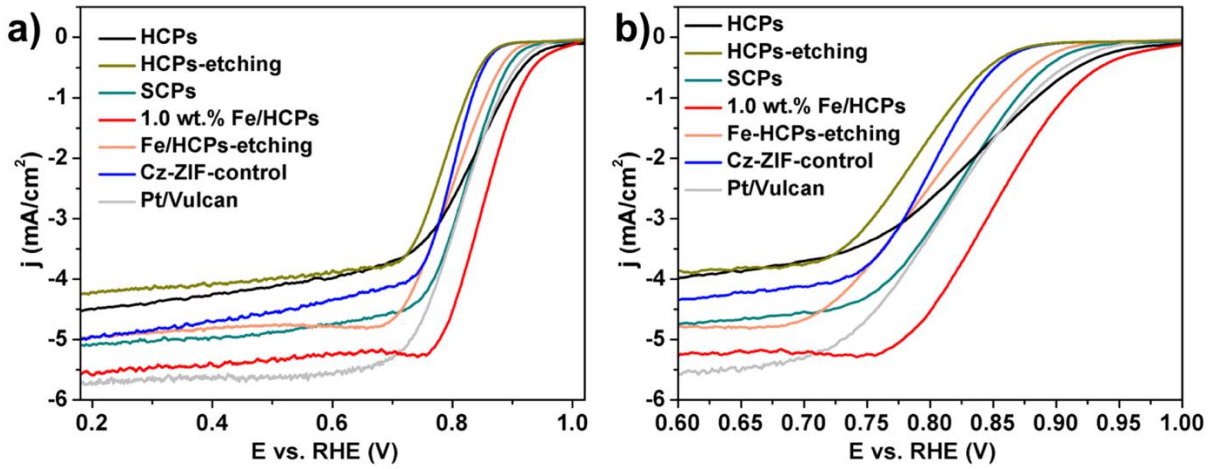

Figure S5. (a) ORR polarization curves of HCPs, HCPs-etching, SCPs, 1.0 wt.% Fe/HCPs, Fe/HCPs-etching, Cz-ZIF-control, and Pt/Vulcan commercial catalyst. (b) enlarged area of plot a) at the range from 0.65 V to 1.00 V.

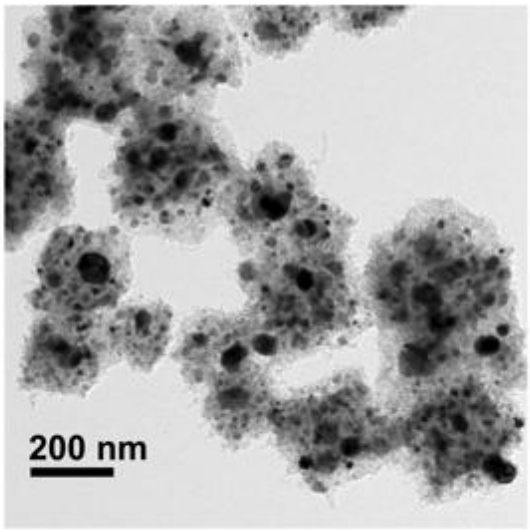

Figure S6. TEM image of Cz-ZIF-control. The Cz-ZIF-control was prepared by carbonizing the bimetallic ZIF-control using the mixture of Co and Zn precursors. This sample serves as a control catalyst to evaluate the electrochemical activity of HCPs and SCPs. The average size of Cz-ZIF-control is around 200-300 nm that is similar to that of HCPs and SCPs. The block morphology of Cz-ZIF-control is similar to the parent ZIFs, which evidences the morphology inherence as well. However, Cz-ZIF-control is not uniform due to that their parent ZIF precursor has random morphologies.

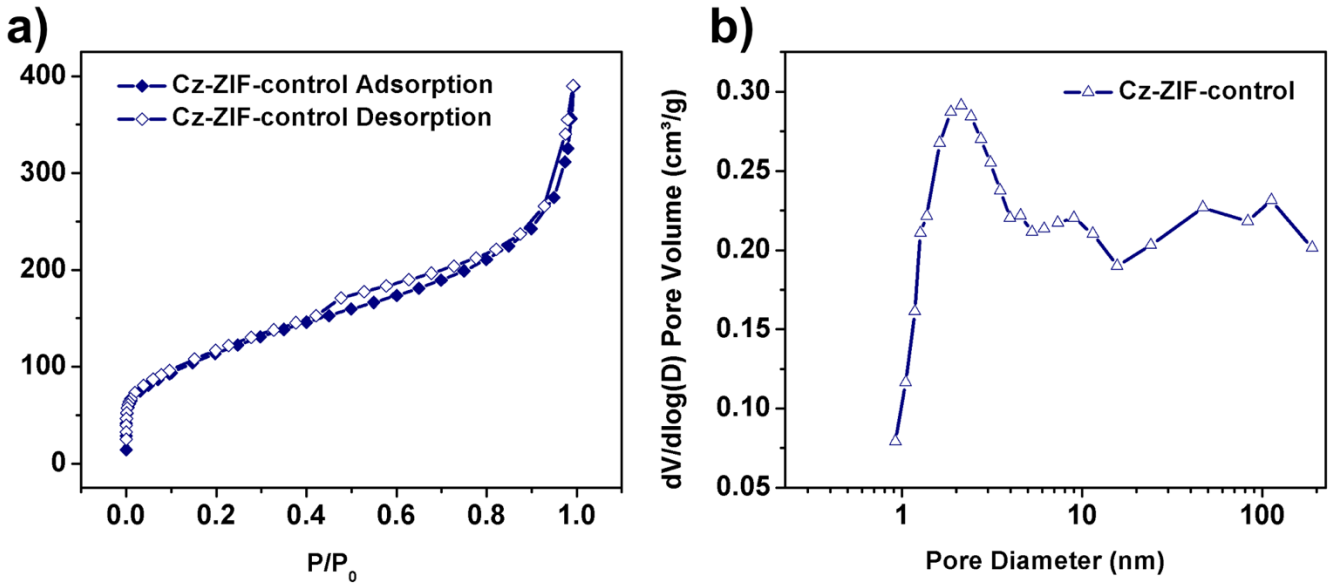

Figure S7. (a) N_2 physisorption isotherm and (b) pore size distribution of Cz-ZIF-control.

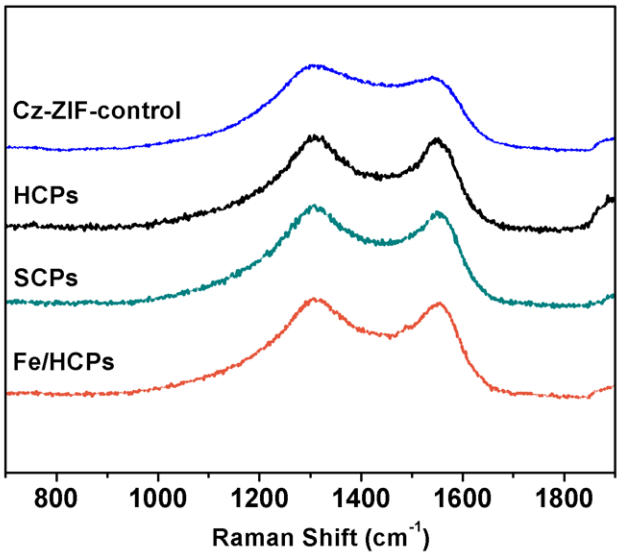

Figure S8. Raman spectra of HCPs, SCPs, Fe/HCPs, and Cz-ZIF-control.

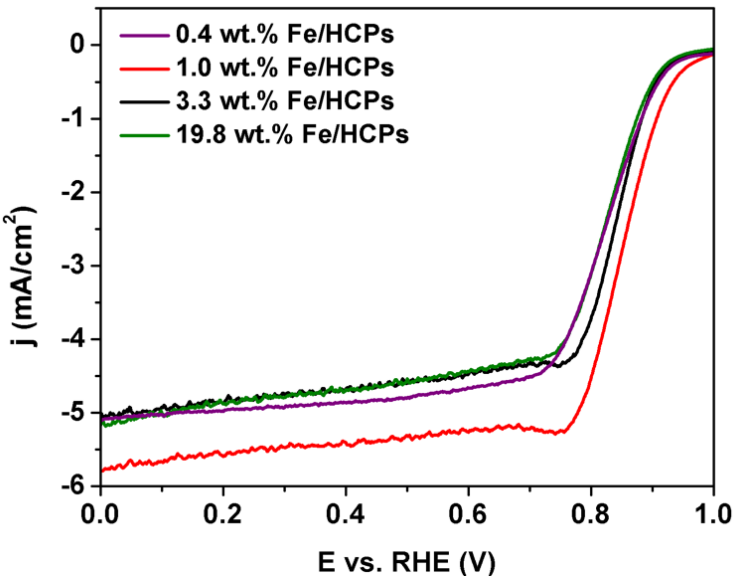

Figure S9. ORR polarization curves of Fe/HCPs with 0.4, 1.0, 3.3, and 19.8 wt.% Fe loading. The E_{onset} indicates that 1.0 wt.% Fe is the best loading under our reaction conditions. These actual loadings of Fe were measured by ICP-OES.

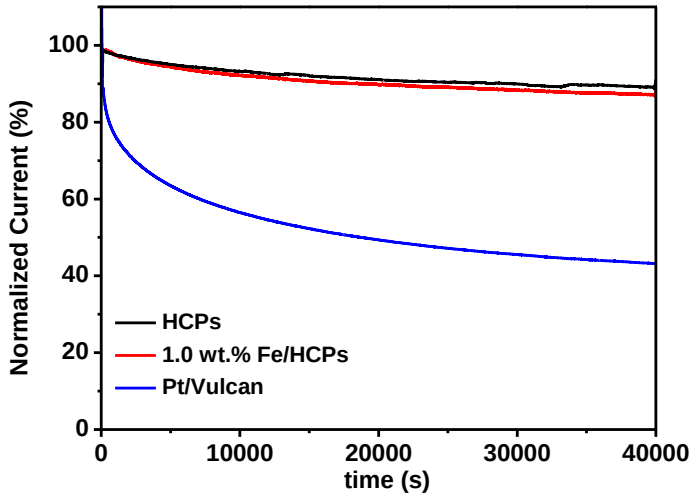

Figure S10. Chronoamperometric responses of HCPs, 1.0 wt.% Fe/HCPs, and commercial 20% Pt/Vulcan catalysts kept at 0.65 V vs. RHE in O_2 saturated 0.1 M KOH with a rotational speed of 400 rpm. All the current was normalized by the initial current, and the retained current was shown as a percentage.

Table S1. ICP-MS and ICP-OES results.

samples	Co /wt.%	Zn /wt.%	Fe /wt.%	weight loss after carbonization /%
Hollow ZIF-67/8	11.4	18.6	-	-
HCPs	23.9	0.1	-	51.3
Core/shell ZIF-67/8	18.2	5.5	-	-
SCPs	41.3	< 0.1	-	57.7
Fe/hollow ZIF-67/8	16.3	27.8	-	-
1.0 wt.% Fe/HCPs	34.4	0.1	1.0	-
ZIF-control	12.3	9.6	-	-
Cz-ZIF-control	41.8	1.2	-	48.8
HCPs-etching	8.1	< 0.1	-	-
Fe-HCPs-etching	11.5	< 0.1	0.9	-

Table S2. Porosity summary of carbonized materials.

samples	HCPs	SCPs	Cz-ZIF-control
BET surface areas / m^2 g^{-1}	227	282	361
Mesoporous volume / cm^3 g^{-1}	0.47[a]	0.35[a]	0.60[c]
Microporous volume /cm^3 g^{-1}[b]	0.07	0.01	0

[a] BJH adsorption from 0.6-400 nm; [b] determined by the t-plot method; and [c] single point (< 291.8 nm) adsorption total pore volume of pores.

Table S3. ORR summary of carbon catalysts with different synthesis conditions.

samples	$E_{1/2}$ (V)	E_{onset} (V)	$J_{limiting}$ (mA/cm^2) at 0.2 V	$J_{kinetic}$ (mA/cm^2) at 0.9 V
HCPs-3 h-800 ℃-Ar	0.821	0.948	4.49	0.87
HCPs-3 h-600 ℃-Ar	0.718	0.875	5.43	0.14
HCPs-3 h-1000 ℃-Ar	0.751	0.859	4.02	0.047
HCPs-1 h-800 ℃-Ar	0.807	0.896	5.02	0.22
HCPs- 5h-800 ℃-Ar	0.722	0.887	5.51	0.19
HCP-3 h-800 ℃-N_2	0.805	0.888	5.08	0.18

Table S4. XPS analysis of carbonized materials.

samples	N /%	Co /%	C /%	Zn /%	Fe /%
HCPs	6.7	2.2	81.9	0.1	-
SCPs	5.2	3.2	84.6	0.3	-
Fe/HCPs	5.6	2.2	83.2	0.1	trace
Cz-ZIF-control	4.7	2.2	88.2	-	-
N analysis	Pyridinic-N (398.6 ± 0.1 eV) /%		Graphitic-N (400.7 ± 0.2 eV) /%		Oxidized N (403.0 ± 0.3 eV) /%
HCPs	54.3		39.0		6.6
SCPs	51.2		39.6		9.1
Fe/HCPs	53.7		40.1		6.2
Cz-ZIF-control	48.0		43.8		8.1

Table S5. ORR summary of different carbon catalysts.

samples	$E_{1/2}$ (V)	E_{onset} (V)	$J_{limiting}$ (mA/cm^2) at 0.2 V	$J_{kinetic}$ (mA/cm^2) at 0.9 V
HCPs	0.821	0.948	4.49	0.87
SCPs	0.810	0.912	5.08	0.40
Fe/HCPs	0.850	0.960	5.59	1.47
HCPs-etching	0.784	0.869	4.22	0.096
Fe/HCPs-etching	0.799	0.900	4.96	0.26
Cz-ZIF-control	0.793	0.869	4.94	0.10
Pt/Vulcan	0.812	0.925	5.73	0.53

All the current densities were normalized by electrode geometric surface area. The kinetic current was calculated by $1/j = 1/j_{limiting} + 1/j_{kinetic}$.

Table S6. Literature summary of electro-catalytic results of carbon nanostructures in ORR.

samples	$E_{1/2}$ (V)	E_{onset} (V)	$J_{limiting}$ (mA/cm^2)[a]	Condition	Ref.
1:1 Fe-N/carbon nanoshell	0.85	0.98	5.0 at 0.2 V	0.1 M KOH	1
P-CNCo-20	0.85	0.93	5.8 at -0.6 V[b]	0.1 M KOH	2
MDC (Cz-ZIF-67)-750˚C	~ 0.75	~ 0.95	~ 5.5 at 0.2 V	0.1 M $HClO_4$	3
Co@Co_3O_4/NC-1	0.80	~ 0.90	~ 4.4 at 0.2 V	0.1 M KOH	4
Hollow Fe_3C/C-700	0.83	1.05	~ 3.75 at 0.2 V	0.1 M KOH	5
N-MCNSs	~ 0.67	~0.82	~ 3.6 at -0.6 V [b]	0.1 M KOH	6
ZIF-67-900-AL	0.85	0.92	~ 5.2 at 0.4 V	0.1 M KOH	7
FeIM/ZIF-8	0.755	0.915	-	0.1 M KOH	8

[a] Rotation speed is 1600 rpm; [b] vs. Ag/AgCl.

Table S7. Raman spectra summary.

samples	D (cm^{-1})	I_D	G (cm^{-1})	I_G	I_D/I_G
HCPs	1345	6171	1587	6929	1.02
SCPs	1345	7363	1592	6756	1.09
Fe/HCPs	1344	11071	1590	10467	1.06
Cz-ZIF-control	1340	25151	1578	21159	1.19

All the carbon materials have two similar peaks around 1350 cm^{-1} and 1580 cm^{-1}, which are the D band and G band of graphitic carbon. The intensity ratio of D band and G band (I_D/I_G) is 1.02 for HCPs and 1.06 for Fe/HCPs, indicating these catalysts have similar defect degrees. The peaks positions of Cz-ZIF-control have slightly left shifts, and the I_D/I_G ratio is higher compared to that of HCPs and SCPs.

Table S8. ORR summary of carbon catalysts with different Fe loadings.

samples	$E_{1/2}$ (V)	E_{onset} (V)	$J_{limiting}$ (mA/cm^2) at 0.2 V	$J_{kinetic}$ (mA/cm_2) at 0.9 V
0.4 wt.% Fe/HCPs	0.824	0.937	4.98	0.74
1.0 wt.% Fe/HCPs	0.850	0.960	5.59	1.47
3.3 wt.% Fe/HCPs	0.840	0.929	4.87	0.67
19.8 wt.% Fe/HCPs	0.823	0.925	4.88	0.56

Reference

1 Y. Wang, A. Kong, X. Chen, Q. Lin and P. Feng, *ACS Catal.*, 2015, **5**, 3887–3893.

2 Y. Z. Chen, C. Wang, Z. Y. Wu, Y. Xiong, Q. Xu, S. H. Yu and H. L. Jiang, *Adv. Mater.*, 2015, **27**, 5010–5016.

3 W. Xia, J. Zhu, W. Guo, L. An, D. Xia and R. Zou, *J. Mater. Chem. A*, 2014, **2**, 11606−11613.

4 A. Aijaz, J. Masa, C. Rosler, W. Xia, P. Weide, A. J. Botz, R. A. Fischer, W. Schuhmann and M. Muhler, *Angew. Chem. Int. Ed.*, 2016, **55**, 4087-4091.

5 Y. Hu, J. O. Jensen, W. Zhang, L. N. Cleemann, W. Xing, N. J. Bjerrum and Q. Li, *Angew. Chem. Int. Ed.*, 2014, **53**, 3675-3679.

6 T. Yang, J. Liu, R. Zhou, Z. Chen, H. Xu, S. Z. Qiao and M. J. Monteiro, *J. Mater. Chem. A*, 2014, **2**, 18139-18146.

7 X. Wang, J. Zhou, H. Fu, W. Li, X. Fan, G. Xin, J. Zheng and X. Li, *J. Mater. Chem. A*, 2014, **2**, 14064-14070.

8 D. Zhao, J. L. Shui, C. Chen, X. Chen, B. M. Reprogle, D. Wang and D. J. Liu, *Chem. Sci.*, 2012, **3**, 3200-3205.